# The Cosmic Neutrino Background and Effects of Rayleigh Scattering on the CMB and Cosmic Structure

by

Elham Alipour Khayer

B.Sc. Sharif University of Technology, 2008

A THESIS SUBMITTED IN PARTIAL FULFILLMENT
OF THE REQUIREMENTS FOR THE DEGREE OF

**Doctor of Philosophy**

in

THE FACULTY OF GRADUATE AND POSTDOCTORAL STUDIES
(Physics)

The University of British Columbia
(Vancouver)

October 2015

# Abstract

The Cosmic Microwave Background (CMB) radiation, photons free-streaming from their last scattering surface at $z \simeq 1090$, is currently our main source of information about the origin and history of the Universe. The vast recent advancement in technology has led to new possibilities for gathering data especially detecting the CMB with high accuracy. The goal of the two projects studied in this thesis is to improve the cosmological perturbation theory to better test cosmology with the upcoming data.

In chapter 4 we explore the effect of Rayleigh scattering on the CMB and cosmic structure. During and after recombination, in addition to Thomson scattering with free electrons, photons also coupled to neutral hydrogen and helium atoms through Rayleigh scattering. The frequency-dependence of the Rayleigh cross section breaks the thermal nature of CMB temperature and polarization anisotropies and effectively doubles the number of variables needed to describe CMB intensity and polarization statistics, while the additional atomic coupling changes the matter distribution and the lensing of the CMB. We introduce a new method to capture the effects of Rayleigh scattering on cosmological power spectra. We show the Rayleigh signal, especially the cross-spectra between the thermal (Rayleigh) E-polarization and Rayleigh (thermal) intensity signal, may be detectable with future CMB missions even in the presence of foregrounds, and how this new information might help to better constrain the cosmological parameters.

In chapter 5 we study the Cosmic Neutrino Background (CNB). In addition to the CMB, the standard cosmological model also predicts that neutrinos were de-

coupled from the rest of the cosmic plasma when the age of the Universe was less than one second, far earlier than the photons. We study the anisotropy of the CNB and for the first time present the full CNB anisotropy power spectrum at large and small scales both for a massless and massive neutrinos. We also show that how presence of nonstandard neutrino self-interactions compatible with current cosmological data alters the CNB power spectrum.

# Preface

This thesis is partly based on one published paper and one manuscript that is close to submission.

A version of chapter 4 has been published. Aside from calculating the Rayleigh scattering cross section in the necessary limit (section 4.2) which was done by Kris Sigurdson and Christopher M. Hirata, I performed all the rest of the calculations, made the plots and drafted the manuscript. Professor Sigurdson provided guidance and comments on the manuscript. The Boltzmann code (CAMB) used in this chapter was provided by Dr. Antony Lewis, however I heavily modified this code for this project. Most of this chapter is contained in the following paper: E. Alipour, K. Sigurdson, Ch. M. Hirata, Physical Review D, **91**, 083520 (2015)

I led the study of the cosmic neutrino background presented in chapter 5. All the analytical and numerical calculations in this chapter were conducted by me but heavily influenced by significant consultation with my supervisor.

# Table of Contents

# List of Tables

# List of Figures

# Glossary

| | |
|---|---|
| **ACT** | Atacama Cosmology Telescope |
| **BAO** | Baryon Acoustic Oscillation |
| **CIB** | Cosmic Infrared Background |
| **CMB** | Cosmic Microwave Background |
| **CNB** | Cosmic Neutrino Background |
| **COBE** | Cosmic Background Explorer |
| **FRW** | Friedmann-Robertson-Walker |
| **ISW** | Integrated Sachs-Wolf |
| **PIXIE** | The Primordial Inflation Explorer |
| **PRISM** | Polarized Radiation Imaging and Spectroscopy Mission |
| **SPT** | South Pole Telescope |
| **WMAP** | Wilkinson Microwave Anisotropy Probe |

# Acknowledgments

Firstly, I would like to thank my research supervisor Prof. Kris Sigurdson for the continuous support, guidance and motivation throughout my Phd, and for helping me in all the time of research and writing of this thesis.

I would also like to thank my supervisory committee, Prof. David Morrissey, Prof. Douglas Scott, Prof. Colin Gay and Prof. Mark Van Raamsdonk for their encouragement, constructive feedback, and hard questions.

I acknowledge the financial support from the University of British Columbia (UBC) through University Four Year Fellowship, PhD Tuition Fee Award and International Partial Tuition Scholarship.

I will always be grateful to my beloved parents and my sisters, who have always supported, encouraged and believed in me. To my friends who always inspired and motivated me throughout my research.

Most importantly, I would like to thank Hamed, my loving, supportive, encouraging, and patient husband without whom this accomplishment would have not been possible. Thank you.

# Chapter 1

# Introduction

We are now entering a golden era of cosmology. Recent advances in technology are opening up new possibilities for gathering data. Complementing that, there has been a dramatic theoretical development in the last couple of decades. In particular, comprehensive models, such as inflation, have emerged which describe how the Universe evolved in its earliest stages and how galaxies and other structures began to form. Inflation predicts that the Universe exponentially expanded just a short time after the Big Bang, and a scale-invariant spectrum of density fluctuations was generated. These primordial perturbations evolved and grew through time to form the distribution of large-scale structure that we see today. This theory has numerous characteristic signatures that allow it to be tested by observational data. One phenomenon which allows us to probe these signatures is the spectrum of temperature and polarization anisotropies in the Cosmic Microwave Background (CMB) radiation. The CMB is a form of polarized electromagnetic radiation filling the entire Universe at a temperature 2.725K that is almost, but not quite, uniform.

The goal of my work is to improve cosmological perturbation theory in order to be able to better test cosmology with the upcoming data. In the past decade the Wilkinson Microwave Anisotropy Probe (WMAP) has provided us with precise measurements of CMB anisotropies [3] and, complemented by next-generation ground based experiments such as South Pole Telescope (SPT) [4] and Atacama Cosmology Telescope (ACT) [5], the Planck satellite has now characterized the microwave background anisotropies even to a higher precision [2]. Future mea-

surements may even probe CMB anisotropies with more frequencies and higher precision (e.g., Polarized Radiation Imaging and Spectroscopy Mission (PRISM) [6] or The Primordial Inflation Explorer (PIXIE) [7]). This dramatic improvement in the observations challenges theorists to improve the level of their calculations. The focus of the projects in this thesis is to pursue this direction.

We begin the thesis by briefly reviewing some elements of the standard cosmology in section 1.1. In sections 1.2 and 1.3 we present an introduction to the recombination and the cosmic microwave background respectively. Finally we give a brief summary of each thesis chapter. Note that throughout this thesis we use units in which

$$\hbar = c = k_B = 1. \tag{1.1}$$

## 1.1 The standard cosmological model

The current well accepted model of cosmology is called the standard model of Big Bang cosmology also known as Lambda Cold Dark Matter model ($\Lambda$CDM). This model describes an expanding Universe that on large enough scales, based on cosmological principle, is both homogeneous and isotropic. A homogeneous space is one that is translation invariant, or the same at every point. An isotropic space is one which is rotationally invariant, or the same in every direction. According to this model, supported by observations ([8], [9], [10] and [11]), only a small fraction of the Universe consists of radiation and baryonic matter that we are familiar with from our everyday experience. The dominant components of the Universe today are cold dark matter and dark energy.

Cold dark matter is a form of matter that while gravitationally acts the same way as normal visible matter, its particles interact very weakly with electromagnetic radiation (they are dark) and are non-relativistic (they are cold). Dark energy is the most accepted hypothesis to explain the observed acceleration of the expansion of the Universe. The letter $\Lambda$ in $\Lambda$CDM model stands for cosmological constant, the constant energy density filling space homogeneously, which is a sample proposed and often accepted form of dark energy.

This standard observationally consistent cosmological model still however has some unsolved problems. The Universe appears to be statistically homogenous and

isotropic at large scales. The observed CMB has the same temperature across the regions on the sky separated by large enough distances that according to this model, have never been in casual contact [12]. This homogeneity problem is often called the horizon problem. Another problem is the flatness problem. The current energy density of the Universe is observed to be very close to the critical value required to make the Universe flat [13]. Since the total density departs rapidly from the critical value with time, the energy density would have to be fine-tuned to be extremely close to the critical density at the Big Bang.

Inflation was initially introduced to solve the problems mentioned above. According to the theory of inflation, the early Universe expanded exponentially fast for a short time period after the Big Bang. Before this period of inflation, the entire Universe could have been in causal contact and equilibrated to a common temperature, giving the same initial condition everywhere. Widely separated regions today were actually very close together in the early Universe, solving the horizon problem. Additionally, an exponential expansion drives the Universe to flatness resolving the flatness problem [14]. More importantly, inflation provides a mechanism for generating the observed density fluctuations observed today. Since it is very difficult to test a theory based on energy scales far beyond the reach of the accelerators, we can not be certain that inflation is the mechanism explaining the initial condition of the Universe. However, it is by far the most plausible explanation.

The evolution of the Universe before $10^{-10}$ seconds (1 TeV) is not well understood due to very high energy scales and therefore the physics of this era is speculative. However, we know that we need a mechanism such as inflation in the very early universe ($\sim 10^{-34}$ seconds) to solve the horizon and flatness problems and also to generate the seed for primordial fluctuations. We also need baryogenesis, a process that produced an asymmetry between baryons and antibaryons in the very early universe, and also a mechanism to create dark matter.

The history of the Universe from $10^{-10}$ seconds to today is better understood since it is based on tested physical theories like the standard model of particle physics, general relativity and fluid dynamics. Here, we summarize the cosmic history of the Universe after this time on the basis of Ref. [14].

Below 100 GeV, electroweak symmetry breaking occurs, the Z and $W^{\pm}$ bosons

acquire mass and the weak interaction weakens as the temperature of the Universe drops. Around 100 MeV, the temperature of the Universe is cool enough for quarks to form hadrons. Around 1 MeV neutrinos decouple from the rest of the plasma. As the temperature drops below the electron mass, 0.511 MeV, electron-positron annihilation happens. Around 0.1 MeV, during Big Bang nucleosynthesis, protons and neutrons begin to combine into atomic nuclei in the process of nuclear fusion. The energy density of matter dominates over that of radiation at $T \simeq 1$ eV. As the temperature falls below $\sim 0.1$ eV, the neutral hydrogen atoms begin to form and photons decouple. Therefore the relic photons travelling freely from this point to us can tell us about the condition of the Universe when it was roughly 380000 years old.

## 1.2 Recombination

Hydrogen and helium atoms begin to form about 380000 years after the Big Bang. Before this time they are ionized. As the Universe expands and cools down, electrons get captured by the ions, forming electrically neutral atoms. This process is known as recombination.

The cosmic ionization history is generally described in terms of the free electron fraction $x_e$ as a function of time:

$$x_e = \frac{n_e}{n_e + n_H}, \tag{1.2}$$

where $n_e$ is the number density of free electrons and $n_H$ that of atomic hydrogen. While the recombination process ($p + H^- \leftrightarrow H + \gamma$) is fast compared to the expansion of the Universe, the ionization fraction obeys an equilibrium distribution. The equilibrium situation is described by the Saha equation [1]:

$$\frac{x_e^2}{1 - x_e} = \frac{1}{n_e + n_H} \left(\frac{m_e T}{2\pi}\right)^{3/2} e^{-B/T}, \tag{1.3}$$

where $m_e$ is the mass of electron, $T$ is the temperature of plasma and $B = 13.6$ eV is the binding energy.

Due to high photon-baryon ratio ($10^9$), at $T = B = 13.6$ eV, any produced hydrogen atoms will be instantaneously ionized. When the temperature drops below

0.3 eV at redshift $z = 1000$, far below the binding energy, the ionization rate becomes too slow to keep the equilibrium since there are not enough photons in the Wien tail to keep ionizing the hydrogen atoms.

The Saha equation is good for describing the initial departure from full ionization, but the equilibrium breaks down shortly after recombination starts. Therefore the full Boltzmann equation must be solved to find the evolution of the free electron fraction. The direct recombination to the ground state is not relevant since photons emitted from direct recombination can easily re-ionize the nearby neutral atoms. The only way for recombination to happen is via capture to one of the excited states of hydrogen. Photons emitted by electrons going from first excited state to the ground state can escape re-absorption by redshifting out of the line, but the probability for this is very low. The other way for electrons to move from the first excited state to the ground state is through the 2s-ls two-photon transition. Photons emitted by this transition can escape re-absorption. The exact solution and Saha approximation for the free electron fraction are plotted in Figure 1.1.[1]

## 1.3 Cosmic Microwave Background

The Cosmic Microwave Background, photons free-streaming from their last scattering surface at redshift $z \simeq 1100$, is currently our main source of information about the origin and history of the Universe. The CMB has a thermal black body spectrum at temperature of 2.725 K. Historically, the CMB was accidentally observed first at 1964 by Penzias and Wilson who noticed excess noise in their receiver while working on an antenna to detect radio waves bounced off metallic balloons in the atmosphere [15]. In 1992, the Cosmic Background Explorer (COBE) [16] observed small fluctuations of order one in $10^5$ in temperature of the CMB. Later, more advanced experiments such as WMAP [3] and Planck [2] have characterized the anisotropies with higher accuracy. In Figure 1.2 we show the CMB temperature perturbation map seen by Planck.

According to the inflationary cosmological model, the quantum fluctuations in the inflation field provided seed for the density perturbations. Below a temperature of $\sim 0.1$ MeV, the early universe was made of a hot interacting plasma of photons, electron and protons. The photons and electrons were tightly coupled by Thomson

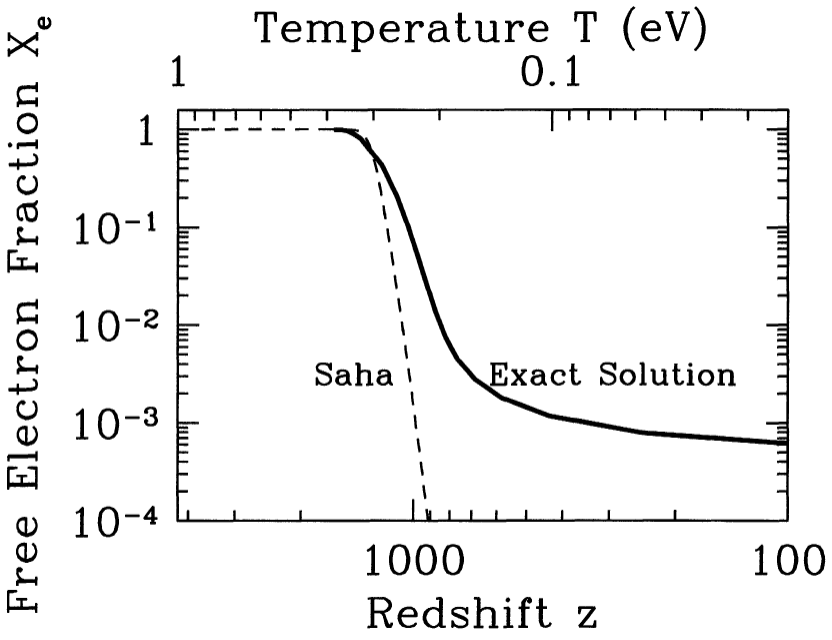


**Figure 1.1:** The exact solution and Saha approximation for the free electron fraction as a function of redshift [1].

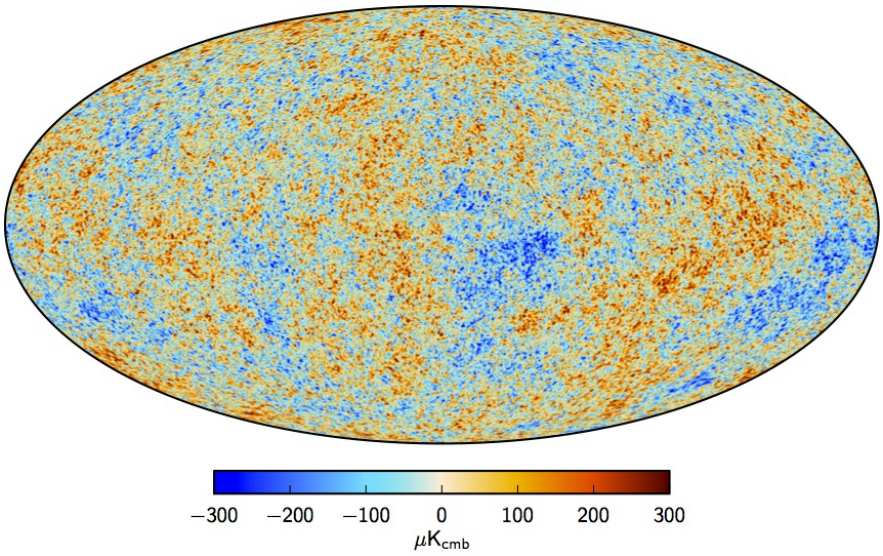


**Figure 1.2:** The Cosmic microwave background temperature perturbation map as seen by Planck [2].

scattering and since the mean free path of photons (the mean distance each photon could travel before encountering an electron) was short, the plasma was opaque to the electromagnetic radiation. As the Universe expanded and the temperature dropped, the electrons and protons combined to form hydrogen atoms. At this point, which is called recombination or the epoch of last scattering, the photons stopped interacting with the electrically neutral hydrogen atoms and they travelled through the Universe without interacting with matter. Hence, the Universe became transparent. After photon decoupling, the Universe continued expanding and cooling and therefore the wavelengths of photons have redshifted to roughly one millimetre and their temperature has cooled down to $\sim 2.725$ K. These photons are the CMB photons that we observe today.

Radiation pressure prevents photon anisotropies from growing due to gravitational instability (in contrast to matter inhomogeneities), therefore the photon perturbations remain small and their evolution falls almost entirely in the domain of linear perturbation theory. They are only influenced a little by the non-linear processes of galaxy formation and therefore we can compute them very precisely. This makes the CMB an excellent source of information about the early Universe since it basically gives a snapshot of the Universe when it was only 380000 years old.

The CMB temperature map is close to a Gaussian random field and therefore to the extent that it is Gaussian, the statistical properties of the temperature map can be described by its power spectrum. The CMB temperature power spectrum observed by Planck is shown in Figure 1.3 [2].

The temperature power spectrum has a series of peaks and troughs. This characteristic peak structure arises due to the physics of the photon-baryon plasma in the early Universe. The pressure of photons tends to erase anisotropies whereas the gravitational attraction of baryons makes them tend to collapse. The competition between these two effects leads to the acoustic oscillations. The peaks and troughs in the spectrum are a signature of this oscillations in the plasma. The peaks come from waves at an extrema of their oscillation, either maximally compressed or rarefied.

The peaks contain interesting physical information. The angular scale of the first peak tells us about the curvature of the Universe [17], [18]. The first peak cor-

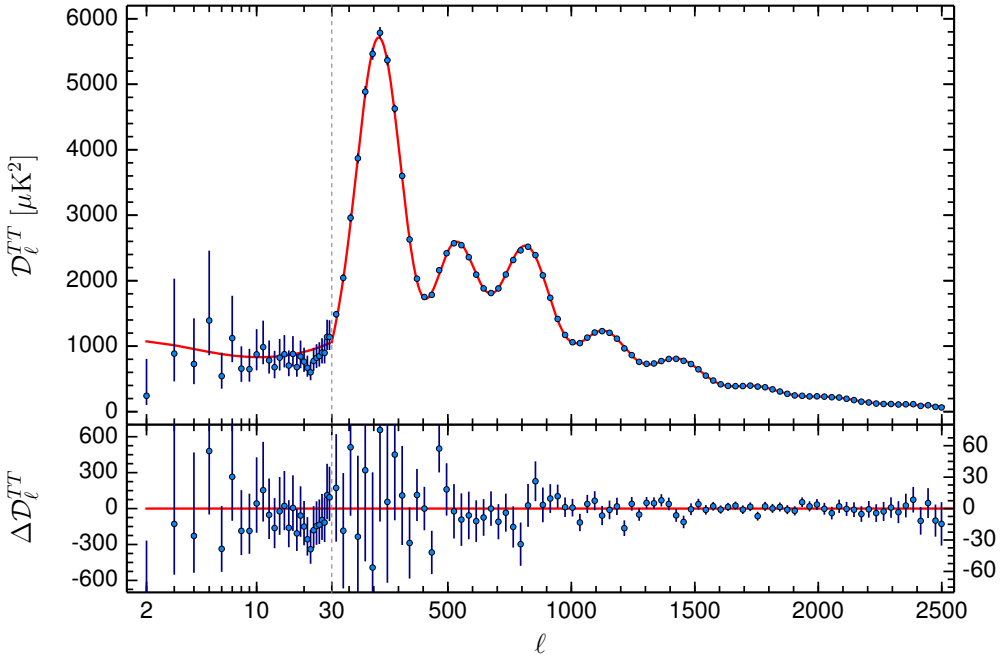


**Figure 1.3:** The CMB temperature anisotropy power spectrum as a function of angular scale $l$ observed by Planck [2]. The red curve on the upper panel shows the best fit ΛCDM theoretical spectrum and the residuals with respect to this model are shown in the lower panel.

responds to the fundamental acoustic mode, the first mode that reached maximum at the time of recombination. The physical scale of this mode is well understood so the angular scale that we observe on the sky depends on the angular diameter distance to the last scattering surface which depends on the curvature of the Universe.

The ratio of the even peaks to the odd peaks can be used to determine the baryon density of the Universe [17], [18]. Baryons load down the photon-baryon oscillations which means the compressions in potential wells got enhanced over rarefactions. This means that the amplitudes of the odd peaks are enhanced over even peaks.

Another feature of the CMB temperature power spectrum is damping of the oscillations at smaller scales, which is called Silk damping or diffusion damping. Silk damping is caused by the finite thickness of the last scattering surface; since photons move a mean distance during the decoupling, any perturbation on scales

smaller than this distance will be washed out.

In addition to the intensity of the CMB, its polarization also gives to further information. There are two types of polarization patterns: the E-mode (curl-free component of the polarizations); and B-mode (curl component). The E-mode, similar to the temperature fluctuations, reflects the recombination history. The detection of the B-mode polarization, which is not sourced by standard scalar type perturbations, can tell us about inflation and physics beyond the standard model of particle physics.

Studying the CMB temperature and polarization anisotropy power spectra provides us with much information about many important cosmological parameters such as the curvature of the Universe, the dark matter and baryon densities, the amplitude and slope of the primordial power spectrum, and the number of relativistic species present at photon decoupling.

## 1.4 Outline of the thesis

This thesis is organized as follows:

In chapter 2 we briefly review the linear cosmological perturbation theory which is a very powerful tool to describe how primordially-generated perturbations in matter and radiation grow due to gravitational instability to form the structures that we see in the Universe today. First we present the background equations governing the evolution of a homogenous and isotopic universe filled with radiation, matter and dark energy. Then we derive the linearized governing equations for a perfect fluid in a perturbed universe in synchronous and conformal Newtonian gauges.

Chapter 3 presents an overview of the CMB anisotropy and the derivation of its temperature and polarization angular power spectrum. We also discuss how foreground contamination is an obstacle in detecting the CMB anisotropies. Foregrounds are any emissions that confuse the primordial CMB signal after the time of last scattering.

In chapter 4 we study the effects of Rayleigh scattering on the CMB and cosmic structure. Rayleigh scattering from neutral hydrogen during and after recombination causes the CMB anisotropies to be frequency dependent and alters the distri-

bution of matter in the Universe. We introduce a new method to capture the effects of Rayleigh scattering on cosmological power spectra. Also a discussion about the detectibility of Rayleigh signal with future CMB missions even in the presence of foregrounds has been given in this chapter.

In addition to the CMB, the standard model also provides us with cosmic neutrino background (CNB), the relic neutrinos which travelled to us freely from when the Universe was only less than one second old. In chapter 5 we study the anisotropy of the Cosmic Neutrino Background (CNB) and derive the full CNB anisotropy power spectrum at large and small scales both for a massless and massive neutrinos. We also discuss how presence of nonstandard neutrino self-interactions which are compatible with the current cosmological data modifies the CNB power spectrum.

# Chapter 2

# The linear cosmological perturbation theory

Linear cosmological perturbation theory is an extremely useful tool to describe how primordially-generated fluctuations in matter and radiation grow to form the structures that exist in the Universe today through gravitational instability. Linear perturbation theory can be formulated since these fluctuations remain small for a large part of cosmic history.

In this theory, to compute the growth of small perturbations in the context of general relativity, one need to solve the Einstein equations linearized about an expanding background. The use of general relativity introduces some complications related to gauge freedom, i.e., the choice of coordinate system; Physical variables must be independent of this choice. Lifshitz [19] pioneered the early work on perturbations. He adopted the synchronous gauge for his coordinate system which is still used in many recent works due to the fact that equations in this particular gauge are more numerically stable than in other gauges. However there are some complications associated with using this gauge such as the appearance of coordinate artifacts or gauge modes. One way to deal with this gauge problem is to carefully keep track of physical and gauge modes. A different approach to this problem was taken by Bardeen [20] by introducing gauge-invariant variables and therefore removing the gauge artifacts. A thorough review of gauge-invariant perturbation theory is given in Ref. [21].

According to the decomposition theorem, linear perturbations to the homogenous and isotropic metric can be divided into three types: scalar, vector and tensor. This classification refers to the way each type transforms under spatial transformations. In this thesis we only follow the evolution of scalar perturbations and since each of these types of perturbations evolve independently we do not need to worry about the possible vector or tensor perturbations. For scalar perturbations, the most convenient and common gauge to use is the conformal Newtonian gauge in which the two scalar fields describing the metric perturbations are identical to the gauge-invariant variables constructed by Bardeen.

In this section we present the Einstein, Boltzmann and fluid equations for the metric and density perturbations in the two most common gauges: synchronous gauge and conformal Newtonian gauge. We largely follow the notation and equations of Ref. [22].

## 2.1 Background equations

The metric describing the geometry of an isotropic and homogenous spacetime is the Friedmann-Robertson-Walker (FRW) metric $g_{\mu\nu}$ [1]. The line element is given by

$$ds^2 = g_{\mu\nu}dx^\mu dx^\nu = -dt^2 + a^2(t)\gamma_{ij}dx^i dx^j, \tag{2.1}$$

where $t$ is the coordinate time, $a(t)$ is a function that only depends on time and is called the scale factor and $\gamma_{ij}$ is the metric tensor on spatial hypersurfaces. Since current observations are consistent with a flat or very nearly flat universe we adopt this choice henceforth and write the line element as

$$ds^2 = -dt^2 + a^2(t)\delta_{ij}dx^i dx^j, \tag{2.2}$$

where $\delta_{ij}$ is the Kronecker delta. An important quantity characterizing the FRW spacetime is the Hubble rate $H$ which measures how rapidly the scale factor changes:

$$H = \frac{da/dt}{a}. \tag{2.3}$$

The Hubble rate has unit of inverse time. The Hubble time ($t \sim H^{-1}$) sets the scale for the age of the Universe and the Hubble length ($d \sim cH^{-1}$) sets the size of the

observable universe. The dynamic evolution of the scale factor $a(t)$ is determined by the Einstein equation:

$$G_{\mu\nu} = 8\pi G T_{\mu\nu}, \tag{2.4}$$

where the left-hand side $G_{\mu\nu}$ is the Einstein tensor which denotes the curvature of the Universe and is very straight-forward to obtain for a homogenous FRW spacetime [1]. $G$ is the the Newton's gravitational constant and $T_{\mu\nu}$ is the energy momentum tensor.

For a perfect fluid the energy momentum tensor has the following form:

$$T_{\mu\nu} = P g_{\mu\nu} + (\rho + P) U^{\mu} U^{\nu}, \tag{2.5}$$

where $\rho$ is the energy density of the fluid, $P$ is the pressure and $U_{\mu} = dx_{\mu}/\sqrt{-ds^2}$ is the four-velocity of the fluid.

The Einstein equations give the following evolution equations for the scale factor which are called the Friedmann equations:

$$H^2 = (\frac{da/dt}{a})^2 = \frac{8\pi G}{3}\rho \tag{2.6}$$

$$\frac{d^2a/dt^2}{a} = -\frac{8\pi G}{6}(\rho + 3P) \tag{2.7}$$

The second Friedmann equation implies that in an expanding Universe with ordinary matter ($\rho + 3P > 0$), $d^2a/dt^2 < 0$ which means there is a singularity in the finite past ($a(t = 0) = 0$). This could be an indication of the breakdown of General Relativity at high energy scales.

The two Friedmann equations can be combined to obtain the continuity equation

$$\frac{d\rho}{dt} + 3H(\rho + P) = 0. \tag{2.8}$$

Defining the equation of state parameter $w = P/\rho$, the continuity equation may be integrated to give

$$\rho \propto a^{-3(1+w)}, \tag{2.9}$$

and the scale factor evolves as

$$a \propto \begin{cases} t^{2/3(1+w)} & w \neq -1 \\ e^{Ht} & w = -1 \end{cases} \tag{2.10}$$

Now we highlight the evolution of scale factor and the energy density in different eras of the Universe. In a radiation dominated universe which is filled with relativistic particles, the equation of state parameter is $w = 1/3$ which gives

$$\rho \propto a^{-4} \qquad \text{and} \qquad a \propto t^{1/2}. \tag{2.11}$$

The next epoch is the matter dominated era where the Universe is filled with non-relativistic matter ($w = 0$). In this epoch:

$$\rho \propto a^{-3} \qquad \text{and} \qquad a \propto t^{2/3}. \tag{2.12}$$

The last epoch is dominated by cosmological constant ($w = -1$) which results in:

$$\rho \propto a^{0} \qquad \text{and} \qquad a \propto e^{Ht}. \tag{2.13}$$

## 2.2 Metric perturbations

Now we allow for small perturbations in the flat FRW metric that break homogeneity and isotropy. It's often convenient to use, instead of t, the conformal time coordinate $\tau$ defined as $d\tau = dt/a$. In synchronous gauge the line element is given by

$$ds^2 = a^2(\tau)\{-d\tau^2 + (\delta_{ij} + h_{ij})dx^i dx^j\}. \tag{2.14}$$

In this gauge the $g_{00}$ and $g_{0i}$ components of the metric are left unperturbed and only the spatial part of it has perturbations $h_{ij}$. Therefore $\tau$ defines proper time for all comoving observers. In this section we will be working in Fourier space with variable $k$. According to the decomposition theorem, the metric perturbation $h_{ij}$ can be decomposed to scalar, vector and tensors modes. By introducing two scalar fields $h(\vec{k},\tau)$ and $\eta(\vec{k},\tau)$ in $k$-space, we can write the scalar mode of $h_{ij}$ as a

Fourier integral [22]:

$$h_{ij}(\vec{x},\tau) = \int d^3k e^{i\vec{k}.\vec{x}}\{\hat{k}_i\hat{k}_j h(\vec{k},\tau) + (\hat{k}_i\hat{k}_j - \frac{1}{3}\delta_{ij})6\eta(\vec{k},\tau)\}. \tag{2.15}$$

Note that $h$ is the trace of $h_{ij}$. The drawback of this gauge is that it is not uniquely defined by the synchronous gauge condition. There is still the freedom to make further transformations and remain within the gauge since the spacelike hypersurface at $t = 0$ can be chosen arbitrarily. This can introduce, in addition to the physical modes, coordinate artifacts.

The line element in the conformal Newtonian gauge is given as

$$ds^2 = a^2(\tau)\{-(1+2\psi)d\tau^2 + (1-2\phi)dx^i dx_i\}, \tag{2.16}$$

where $\phi$ and $\psi$ are two scalar potentials. The Newtonian coordinates and metric perturbations in this gauge are defined uniquely, which means there are no gauge modes in this gauge and all solutions are physical. This can also be realized by noticing that the two scalar potentials in this gauge are equal to the gauge-invariant variables $\Phi_A$ and $\Phi_H$ introduced by Bardeen in Ref. [20].

$$\psi = \Phi_A, \qquad \phi = -\Phi_H. \tag{2.17}$$

Another advantage of working in this gauge is that $\psi$ plays the role of gravitational potential in the Newtonian limit. Also since the perturbed metric in this gauge is diagonal, calculations in this gauge are simpler.

## 2.3 Linearized Einstein equations

The background evolution equations for an homogenous and isotropic universe are presented in section 2.1. In this section we derive the linearized governing equations for a perfect fluid in a perturbed FRW universe in the synchronous gauge and conformal Newtonian gauge.

To solve the linearized Einstein equations, we first perturb the energy-momentum

tensor of a perfect fluid given in 2.5 as

$$\begin{aligned} \delta T^0_0 &= -\delta\rho, \\ \delta T^0_i &= (\rho+P)v_i, \\ \delta T^i_j &= \delta P\delta^i_j+\Sigma^i_j, \end{aligned} \tag{2.18}$$

where $\delta\rho$ and $\delta P$ are the energy density and pressure perturbations respectively, $v_i$ is the velocity perturbation and $\Sigma^i_j$ is the anisotropic shear perturbation which is the traceless component of $T^i_j$.

We solve the Einstein equations in Fourier space $k$. The linearized Einstein equations in both synchronous and conformal Newtonian gauges are given as [22]:

In *synchronous gauge* :

$$\begin{aligned} k^2\eta-\frac{1}{2}\frac{\dot{a}}{a}\dot{h} &= -4\pi Ga^2\delta\rho(\mathrm{Syn}), \\ k^2\dot{\eta} &= 4\pi Ga^2(\rho+P)\theta(\mathrm{Syn}), \\ \ddot{h}+2\frac{\dot{a}}{a}\dot{h}-2k^2\eta &= -24\pi Ga^2\delta P(\mathrm{Syn},) \\ \ddot{h}+6\ddot{\eta}+2\frac{\dot{a}}{a}(\dot{h}+6\dot{\eta})-2k^2\eta &= -24\pi Ga^2(\rho+P)\sigma(\mathrm{Syn}). \end{aligned} \tag{2.19}$$

In *conformal Newtonian gauge* :

$$\begin{aligned} k^2\phi+3\frac{\dot{a}}{a}(\dot{\phi}+\frac{\dot{a}}{a}\psi) &= -4\pi Ga^2\delta\rho(\mathrm{Con}), \\ k^2(\dot{\phi}+\frac{\dot{a}}{a}\psi) &= 4\pi Ga^2(\rho+P)\theta(\mathrm{Con}), \\ \ddot{\phi}+\frac{\dot{a}}{a}(\psi+2\dot{\phi})+(2\frac{\ddot{a}}{a}-\frac{\dot{a}^2}{a^2})\psi+\frac{k^2}{3}(\phi-\psi) &= 4\pi Ga^2\delta P(\mathrm{Con}), \\ k^2(\phi-\psi) &= 12\pi Ga^2(\rho+P)\sigma(\mathrm{Con}). \end{aligned} \tag{2.20}$$

The label "Syn" and "Con" is used to distinguish the components of energy-momentum tensor in the two gauges from each other. Here, overdots denote derivatives with respect to the conformal time $\tau$. The variable $\theta$ is the divergence of the fluid velocity $\theta = ik^jv_j$ and $\sigma$ is defined as $(\rho+P)\sigma = -(\hat{k}_i\hat{k}_j-\frac{1}{3}\delta_{ij})\Sigma^i_j$.

## 2.4 Boltzmann equation

The Boltzmann equation gives us the evolution of the perturbed phase space distribution functions. The phase space distribution of the particles gives the number of particles per unit volume in single-particle phase space. The equation relates how the distribution function of each component evolves with time taking into account the interactions with other species. The Boltzmann equation states:

$$\frac{df}{d\tau} = \frac{\partial f}{\partial \tau} + \frac{\partial f}{\partial x^i}\frac{\partial x^i}{\partial \tau} + \frac{\partial f}{\partial p^\mu}\frac{\partial p^\mu}{\partial \tau} = C[f]. \tag{2.21}$$

The right-hand side, $C[f]$, contains all possible collision terms, $x^i$ is the position of particles and $p^\mu$ is the proper momentum, the momentum measured by an observer at fixed spatial coordinates. For convenience, we introduce the comoving momentum $q^i = ap^i$ and the comoving energy $\varepsilon = a\sqrt{p^2+m^2}$ where $m$ is the mass of the particle. Moreover, we write the comoving momentum in terms of its magnitude and its direction $\vec{q} = q\hat{n}$. Expanding the distribution function up to the first order leads to:

$$f(\vec{x},q,\hat{n},\tau) = f_0(q)[1+\Psi(\vec{x},q,\hat{n},\tau)], \tag{2.22}$$

where $f_0(q)$ is the zeroth-order distribution function and $\Psi(\vec{x},q,\hat{n},\tau)$ is the perturbation to this distribution function. The function $f_0(q)$ for fermions is the Fermi-Dirac distribution (positive sign in Eq. 2.23) and for bosons is the Bose-Einstein distribution (negative sign in Eq. 2.23):

$$f_0(q) = \frac{1}{e^{\varepsilon/k_B T_0} \pm 1}, \tag{2.23}$$

where $k_B$ is the Boltzmann constant and $T_0 = aT$ is the temperature of the particles today. Using the geodesic equations, one can estimate $\partial p^\mu/\partial\tau$ in Eq. 2.21 in the two gauges we are interested in. Then the Boltzmann equation leads to the following evolution equations for the perturbation of distribution function in $k$-space:

In *synchronous gauge* :

$$\frac{\partial\Psi}{\partial\tau} + i\frac{q}{\varepsilon}(\vec{k}.\hat{n})\Psi + \frac{d\ln f_0}{d\ln q}[\dot{\eta} - \frac{\dot{h}+6\dot{\eta}}{2}(\vec{k}.\hat{n})^2] = \frac{1}{f_0}C[f]. \tag{2.24}$$

In *conformal Newtonian gauge* :

$$\frac{\partial \Psi}{\partial \tau} + i\frac{q}{\varepsilon}(\vec{k}.\hat{n})\Psi + \frac{d\ln f_0}{d\ln q}[\dot{\phi} - i\frac{\varepsilon}{q}(\vec{k}.\hat{n})\psi] = \frac{1}{f_0}C[f]. \tag{2.25}$$

Since in the previous section we wrote Einstein equations in terms of the perturbations in energy-momentum tensor $\delta T^{\mu}_{\nu}$, we need to find the relation between $\delta T^{\mu}_{\nu}$ and the perturbation in the distribution function $\Psi$. The general energy-momentum tensor written in terms of the distribution function is given by [22]:

$$T_{\mu\nu} = \int dP_1 dP_2 dP_3 (-g)^{-1/2} \frac{P^{\mu}P^{\nu}}{P^0} f(\vec{x}, \vec{P}, \tau), \tag{2.26}$$

where $P^{\mu}$ is the canonical momentum and $g$ denotes the determinant of the metric $g_{\mu\nu}$. Using the perturbed distribution function, the components of the energy-momentum tensor to linear order in the perturbations can be written as

$$\begin{aligned}
T^0_0 &= -(\rho + \delta\rho) = -a^{-4} \int q^2 dq d\Omega \sqrt{q^2 + m^2a^2} f_0(q)(1+\Psi), \qquad (2.27)\\
T^0_i &= (\rho + P)v_i = a^{-4} \int q^2 dq d\Omega q n_i f_0(q)\Psi,\\
T^i_j &= (P + \delta P)\delta^i_j + \Sigma^i_j = a^{-4} \int q^2 dq d\Omega \frac{q^2 n_i n_j}{\sqrt{q^2 + m^2a^2}} f_0(q)(1+\Psi),
\end{aligned}$$

where $d\Omega$ is the solid angle associated with direction $\hat{n}$.

# Chapter 3

# The Cosmic Microwave Background anisotropy

In this chapter we briefly review the physics and the statistical interpretation of CMB temperature and polarization fluctuations.

## 3.1 Temperature anisotropies

Photons evolve differently before and after recombination. Before recombination, the rate of the Thomson scattering, which couples photons and electrons, is much larger than the rate of the expansion of the Universe. As a result, photons and baryons behave as a single tightly coupled fluid. The differential cross section $d\sigma/d\Omega$, defined as the radiated intensity per unit solid angle divided by the incoming intensity per unit area, for Thomson scattering is given by [22]:

$$\frac{d\sigma}{d\Omega} = \frac{3\sigma_T}{16\pi}(1+\cos^2\alpha), \tag{3.1}$$

where $\sigma_T = 0.6652 \times 10^{-24}\text{cm}^2$ is the total Thomson cross section and $\alpha$ is the scattering angle.

After recombination, the rate of the Thomson scattering becomes smaller than the rate of the expansion of the Universe, photons travel almost freely and the Universe becomes transparent.

To quantify the evolution of the CMB temperature anisotropies, we expand the photon distribution function about its zero-order Bose-Einstein value:

$$f(\vec{x}, p, \hat{n}, \tau) = [e^{\frac{p}{T(\tau)[1+\theta_I(\vec{x},\hat{n},\tau)]}} - 1]^{-1}, \tag{3.2}$$

where $\vec{x}$, $p$ and $\hat{n}$ are the position, the magnitude of the momentum and the direction of the momentum respectively. $T(\tau)$ is the temperature of photons and $\theta_I(\vec{x}, \hat{n}, \tau)$ is the intensity or temperature perturbation. The temperature perturbation does not depend on $p$ since the magnitude of the photon momentum is virtually unchanged during a Thomson scattering. The temperature perturbation $\theta_I$ is related to the distribution perturbation $\Psi$ in Eq. 2.22 by

$$\theta_I = -[\frac{d\ln f_0}{d\ln p}]^{-1}\Psi. \tag{3.3}$$

We solve the evolution of the temperature perturbation $\theta_I$ in Fourier $k$ space. We expand $\theta_I$ in Legendre series:

$$\theta_I(\vec{k}, \hat{n}, \tau) = \sum_{l=0}^{\infty}(-i)^l(2l+1)\theta_{Il}(\vec{k}, \tau)P_l(\mu). \tag{3.4}$$

The cosine of the angle between the wavenumber $\vec{k}$ and the photon direction $\hat{n}$ is defined to be $\mu = \hat{k}\cdot\hat{n}$ and $P_l(\mu)$ is the Legendre polynomial of order $l$. The monopole of photon distribution $\theta_{I0}$ correspond to $l = 0$, dipole $\theta_{I1}$ to $l = 1$, etc.

Now we can write the Boltzmann equations for photons in both synchronous and conformal Newtonian gauges which govern the evolution of photon temperature perturbations [1]:

In *synchronous gauge* :

$$\dot{\theta}_I + ik\mu\theta_I - (\dot{\eta} - \frac{\dot{h}+6\dot{\eta}}{2}\mu^2) = n_e\sigma_T a[\theta_{I0} - \theta_I + \mu v_b - \frac{1}{2}P_2(\mu)\Pi]. \tag{3.5}$$

In *conformal Newtonian gauge* :

$$\dot{\theta}_I + ik\mu\theta_I - \dot{\phi} + ik\mu\psi = n_e\sigma_T a[\theta_{I0} - \theta_I + \mu v_b - \frac{1}{2}P_2(\mu)\Pi]. \tag{3.6}$$

$h$ and $\eta$ are the two scalar metric perturbations in synchronous gauge and $\phi$ and $\psi$ are metric perturbations in conformal Newtonian gauge, $n_e$ and $v_b$ are the proper mean density and velocity of electrons, and $\Pi$ is defined as

$$\Pi = \theta_{I2} + \theta_{E0} + \theta_{E2}, \tag{3.7}$$

where $\theta_{E0}$ and $\theta_{E2}$ are monopole and quadrupole of E-polarization perturbation.

### 3.1.1 Temperature power spectrum

To extract information about the Universe from the observational data, the Legendre transformation of the two-point correlation function of the CMB fluctuations, the CMB power spectrum, is often used. To connect the observed anisotropy power spectrum to the $\theta_{Il}$ variable, we expand the temperature perturbation field $\theta_I(\vec{k},\hat{n},\tau)$ in terms of spherical harmonics $Y_{lm}$:

$$\theta_I(\vec{k},\hat{n},\tau) = \sum_{l=1}^{\infty}\sum_{m=-l}^{l} a_{lm}Y_{lm}(\hat{n}). \tag{3.8}$$

Since the spherical harmonics are a complete basis for functions on the surface of a sphere, all the information in the temperature field is contained in the amplitudes $a_{lm}$. The mean value of $a_{lm}$'s is zero but they have non-zero variance (angular power spectrum) which is defined as:

$$C_l = \frac{1}{2l+1}\sum_m \langle a_{lm}a^*_{lm}\rangle, \qquad \text{or} \qquad \langle a_{lm}a^*_{l'm'}\rangle = \delta_{ll'}\delta_{mm'}C_l. \tag{3.9}$$

The angular power spectrum $C_l$ is an important tool in the statistical analysis of the CMB. This power spectrum gives the cosmological information contained in the millions of pixels of a CMB map in terms of a much more compact data representation. The relation between $C_l$ and $\theta_l$ is given by [1]:

$$C_l = 4\pi\int_0^{\infty} k^2 dk P_\psi(k)|\theta_{Il}(k,\tau=\tau_0)|^2, \tag{3.10}$$

where $P_\psi(k)$ is the primordial potential fluctuation power spectrum which contains information about the initial condition of the Universe.

## 3.2 Polarization anisotropies

In addition to anisotropies in the CMB temperature, we expect the CMB to become polarized via Thomson scattering. Thomson scattering allows all the radiation transverse to the outgoing direction to pass through unimpeded, while stopping any radiation parallel to the outgoing direction. If in the rest frame of the electron, the incident radiation has the same intensity in every direction, then the outgoing radiation remains unpolarized because orthogonal polarization directions cancel out. Only if the incoming radiation field has a quadrupole component, the outgoing incident will be polarized [1] and [23]. As before photon decoupling the electrons and photons are tightly coupled, the photon quadrupole is relatively small and we expect the polarization perturbations to be smaller than the temperature anisotropies.

Polarized light is usually described in terms of the Stokes parameters. Consider a monochromatic plane electromagnetic wave with frequency $\omega_0$ propagating in the $z$ direction. Its electric field vector at any given point in space can be written as

$$E_x = A_x(t)\cos[\omega_0 t - \phi_x(t)], \qquad E_y = A_y(t)\cos[\omega_0 t - \phi_y(t)], \tag{3.11}$$

where $A_x$, $A_y$ and $\phi_x$, $\phi_y$ describe the amplitude and phases in the $\hat{x}-\hat{y}$ plane respectively.

The Stokes parameters are defined as [23]:

$$I = \langle A_x^2\rangle + \langle A_y^2\rangle, \tag{3.12}$$

$$Q = \langle A_x^2\rangle - \langle A_y^2\rangle, \tag{3.13}$$

$$U = \langle 2A_xA_y\cos(\phi_x-\phi_y)\rangle, \tag{3.14}$$

$$V = \langle 2A_xA_y\sin(\phi_x-\phi_y)\rangle. \tag{3.15}$$

The parameter $I$ measures the intensity of radiation and is always positive. The other three parameters describe the polarization state of radiation and can be either positive or negative. $Q$ and $U$ quantify the magnitude of the linear polarization, and $V$ parametrizes the circular polarization. $I$ is invariant under a rotation in $\hat{x}-\hat{y}$ plane and therefore can be expanded in terms of scalar (spin-0) spherical harmonics

Eq. 3.8. However $Q$ and $U$ transform under rotation by angle $\phi$ such that [14]

$$(Q \pm iU) \longrightarrow e^{\mp 2i\phi}(Q \pm iU). \tag{3.16}$$

This implies that the linear combinations $(Q \pm iU)$ are spin-2 quantities and we need to expand them on a sphere in terms of tensor (spin-2) spherical harmonics [14]:

$$(Q \pm iU)(\hat{n}) = \sum_{l,m} a_{\pm 2,lm}\ {}_{\pm 2}Y_{lm}(\hat{n}). \tag{3.17}$$

Instead of $a_{\pm 2,lm}$, it's convenient to introduce their linear combination

$$a_{E,lm} = -\frac{1}{2}(a_{2,lm} + a_{-2,lm}), \qquad a_{B,lm} = -\frac{1}{2i}(a_{2,lm} - a_{-2,lm}). \tag{3.18}$$

Now instead of spin-2 quantities we define two scalar fields such that:

$$E(\hat{n}) = \sum_{lm} a_{E,lm} Y_{lm}(\hat{n}), \qquad B(\hat{n}) = \sum_{lm} a_{B,lm} Y_{lm}(\hat{n}). \tag{3.19}$$

In analogy with electric and magnetic fields, these $E$ and $B$ field represent the "curl-free" and "divergence-free" component of the polarization field and they completely specify the linear polarization field [14].

### 3.2.1 Polarization power spectra

Analyzing both temperature and polarization anisotropies at the same time leads to four types of non-vanishing correlations: the auto-correlation of temperature and $E$- and $B$-modes polarization perturbations and also the cross-correlation of temperature and $E$-mode polarization fluctuations. The cross-correlation of $B$-mode and temperature anisotropies and also $B$-mode and $E$-mode vanish due to parity [14].

The angular power spectra are defined as before

$$C_l^{XY} = \frac{1}{2l+1} \sum_m \langle a^*_{X,lm} a_{Y,lm} \rangle, \tag{3.20}$$

where $X$ and $Y$ are $I$ for intensity, $E$ for $E$-mode polarization or $B$ for $B$-mode

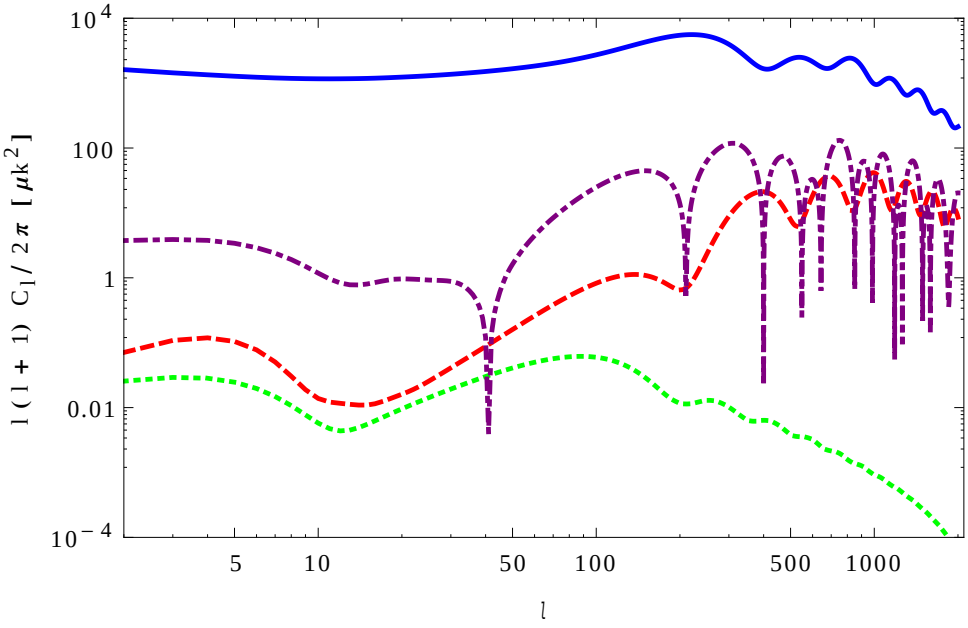


**Figure 3.1:** The theoretical CMB power spectra. The blue (solid), red (dashed), green (dotted) and purple (dot dashed) are for the temperature, E-polarization, B-polarization and Temperature-E polarization cross-correlation spectra respectively.

polarization. Figure 3.1 shows the theoretical prediction for these power spectra calculated by CAMB [24].

The temperature and $E$-mode auto-correlation as well as $TE$ cross-correlation are dominated by the scalar perturbations, while the $B$-mode is only generated by tensor perturbations. As discussed in section 1.3, analyzing the observed CMB power spectra provides us with information about the early universe.

## 3.3 Foregrounds

One of the biggest challenges in observing CMB anisotropies are foregrounds, which are any other sources of radiation in the path of CMB photons that also emit at microwave frequencies. Dust, synchrotron radiation (relativistic electrons in galactic magnetic field) and free-free or bremsstrahlung emission (electrons ac-

celerated in ionized gas) from our galaxy as well as extragalactic point sources could be potential problems in detecting the CMB anisotropies [25].

The understanding and removal of CMB foregrounds has become an important topic in CMB data analysis. There are a couple of reasons why foregrounds can be managed. Firstly the spectral shapes of all the foregrounds are different from one another and from the black body shape of the CMB. For example dust emission has a spectrum which rises with frequency, while free-free and synchrotron emission have falling frequency spectra. Therefore by observing the CMB at different frequency channels we can extract the CMB signal from the foregrounds. Also the foreground amplitudes are found to be smaller than the CMB amplitude in a fairly wide frequency window. There are a number of papers such as Ref.[25], [26], [27] and [28] which present a comprehensive treatment of foreground problem and suggest an optimal way to remove foreground contamination from the CMB signal.

# Chapter 4

# Effects of Rayleigh Scattering on the CMB and Cosmic Structure

## 4.1 Introduction

Most descriptions of the Cosmic Microwave Background (CMB) anisotropies assume that before recombination at $z \simeq 1090$, photons are tightly coupled to baryons through Thomson scattering with electrons and afterwards free stream from the surface of last scattering to us [21], [22],[23]. However, in fact photons were coupled not only to free electrons through Thomson scattering, but also to neutral hydrogen and helium through Rayleigh scattering. The Rayleigh scattering cross section depends approximately on photon frequency to the fourth power and, since it modifies the opacity near decoupling at the few percent level [29], has been neglected in most of the literature to simplify the analysis. In this chapter we revisit the impact of Rayleigh scattering on cosmological perturbations, quantify its effects, and suggest potential ways that this effect may be detected in the future.

In the past decade the Wilkinson Microwave Anisotropy Probe (WMAP) has provided us with precise measurements of CMB anisotropies [3] and, complemented by next-generation ground based experiments (SPT [4], ACT [5]), the Planck satellite has now characterized the microwave background anisotropies to an even higher precision [30]. Future measurements may even probe CMB anisotropies with more frequencies and higher precision (e.g., PRISM [6] or PIXIE [7]). With

this dramatic improvement in experimental capability in mind it is timely to include the physics of Rayleigh scattering in cosmological perturbation theory both to find accurate solutions and to forecast whether these effects might be measured with proposed instruments.

A conceptually straightforward method to calculate the effect of Rayleigh scattering on photon perturbations, as its cross section is frequency dependent, is to consider separate Boltzmann hierarchies with different scattering sources and visibility functions at each frequency of interest. While this captures the effects of the extra opacity that photons experience, it does not account for either the momentum transferred to the atoms nor the effect of spectral distortion on gravitational perturbations. In order to model these effects, the photon perturbation at each frequency must be integrated over to determine the photon density and momentum density which influence gravitation perturbations and the photon-baryon coupling. Existing work has modelled the effect of Rayleigh scattering on CMB anisotropies but has avoided determining the baryonic back reaction in detail [31, 32]. We introduce here a new approach to solve this problem and accurately treat baryons and frequency-dependent photon perturbations simultaneously, allowing us to quantify the impact of Rayleigh scattering on matter perturbations for the first time. We also validate the results of existing CMB anisotropy calculations. The key innovation in our approach is to track perturbations in photon spectral-distortions rather than photon perturbations at a particular frequency.

Rayleigh scattering changes the rate at which photons and baryons decouple from each other, and extra photon drag modifies how baryon perturbations are influenced by photon perturbations. As we quantify below, this alters the shape of the matter correlation function and makes a small shift to the Baryon Acoustic Oscillation (BAO) scale. Like prior work on this subject we find that Rayleigh scattering results in percent level frequency-dependent distortions to CMB power spectra. These distortions break the thermal nature of CMB temperature and polarization anisotropies so that primary CMB intensity and polarization patterns at different frequencies are not perfectly correlated with each other. We show below that to a very good approximation this effectively doubles the number of random variables needed to completely describe the CMB sky, and determine for the first time the set of intensity and E-polarization eigenspectra needed to capture this statistical in-

formation. Finally, we forecast how well future CMB missions might detect these eigenspectra and show that a PRISM-like experiment may be able to detect the Rayleigh signal.

This chapter is organized as follows: In Section 4.2, the relevant Rayleigh scattering cross sections for hydrogen and helium are presented. Section 4.3 reviews the cosmological equations governing the evolution of perturbations in the presence of Rayleigh scattering and presents our new method to calculate the effect of this additional frequency-dependent opacity. The effect of Rayleigh scattering on the matter two-point correlation function and on the CMB power spectra is calculated in Section 4.4 and 4.5 respectively. In Section 4.6, we present the two sets of variables needed to describe the CMB intensity and E-polarization statistics. Section 4.7 investigates the possibility of detecting the Rayleigh signal and Section 4.8 concludes.

## 4.2 Rayleigh scattering cross section

An electron of charge $e$ and mass $m$ which is part of an atomic system acts like a harmonic oscillator with frequency $\nu_0$, the characteristic transition frequency. When this oscillator is subjected to a plane wave radiation of frequency $\nu$ which is much smaller than $\nu_0$, the total energy radiated per unit time in all directions is [33]:

$$P = \frac{8\pi}{3}\left(\frac{e^2}{mc^2}\right)^2 \frac{\nu^4}{(\nu_0^2 - \nu^2)^2} cU, \tag{4.1}$$

where $c$ is the speed of light, $U = E_0^2/4\pi$ is the energy density of the incident field and $E_0$ is the amplitude of the electric field. The scattering cross section is defined as

$$\sigma = \frac{P}{U} = \frac{8\pi}{3}\left(\frac{e^2}{mc^2}\right)^2 \frac{\nu^4}{(\nu_0^2 - \nu^2)^2}. \tag{4.2}$$

The corresponding quantum mechanical expression for the Rayleigh scattering cross section is

$$\sigma_R(\nu) = \sigma_T |S|^2, \tag{4.3}$$

where $\sigma_T$ is the Thomson cross section and the dimensionless scattering amplitude, S, is given by [33]

$$S = \sum_{j=2}^{\infty} f_{1j} \frac{\nu^2}{\nu_{1j}^2 - \nu^2}. \tag{4.4}$$

Here $\nu_{1j}$ is the Lyman series frequencies, and $f_{1j}$ is the Lyman series oscillator strength which expresses the probability of the absorption or emission of a photon in transition between the ground state and excited states of an atom. Note that the summation includes an implied integration over unbound states $j$.

At the time of recombination, when $T \simeq 0.25$ eV, typical photon frequencies are much smaller than $\nu_{1j}$ and it is therefore appropriate to Taylor-expand the dimensionless scattering amplitude as

$$S = \sum_{k=0}^{\infty} a_{2k+2} (h\nu)^{2k+2}, \tag{4.5}$$

where the coefficients are

$$a_{2k+2} = \sum_{j \geq 2} f_{1j} (h\nu_{1j})^{-2k-2} + \int_{E_I}^{\infty} \frac{df}{dE} E^{-2k-2} dE. \tag{4.6}$$

Here we have written the integral over continuum states explicitly. The integral starts at the ionization energy $E_I$ of the relevant atom. The Rayleigh scattering cross section is then

$$\sigma_R = \sigma_T \sum_{k=0}^{\infty} b_{2k+4} (h\nu)^{2k+4}, \tag{4.7}$$

where

$$b_{2k+4} = \sum_{p=0}^{k} a_{2p+2} a_{2(k-p)+2}. \tag{4.8}$$

The coefficients can be evaluated provided that the oscillator strength distributions are known. For H, these are known exactly: for the discrete spectrum ($1s \to np$), the oscillator strengths are [34]

$$f_{1s,np} = \frac{256 n^5 (n-1)^{2n-4}}{3(n+1)^{2n+4}}, \tag{4.9}$$

with $h\nu_{1s,np} = (1 - n^{-2})$Ry. Above $E_I = 1\,\mathrm{Ry} = 13.6$ eV there is a continuous

| 2k+4 | H | He |
|---|---|---|
| 4 | 1.265625 | 0.120798 |
| 6 | 3.738281 | 0.067243 |
| 8 | 8.813931 | 0.031585 |
| 10 | 19.153795 | 0.014153 |
| 12 | 39.923032 | 0.006226 |

**Table 4.1:** The cross-section coefficients $b_{2k+4}\mathrm{Ry}^{2k+4}$ for H and He in the Rydberg-based units that we adopt for this work.

spectrum of oscillator strengths,

$$\frac{df}{dE} = \frac{128e^{-4\nu\arctan(\nu^{-1})}}{3(E/\mathrm{Ry})^4(1-e^{-2\pi\nu})}\mathrm{Ry}^{-1}, \tag{4.10}$$

where $\nu = (E/\mathrm{Ry}-1)^{-1/2}$ is the principal quantum number of the continuum state.

Helium is a multi-electron atom, for which to show the angular momentum quantum numbers we use the following term symbol:

$$^{2S+1}L, \tag{4.11}$$

where $S$ is the total spin quantum number and $L$ is the orbital quantum number in spectroscopic notation which means $L = 0$ correspond to letter $S$ and $L = 1$ correspond to letter $P$. For He, the electric dipole selection rules allow the ground $1s^2\ ^1S$ state to have nonzero oscillator strength only with the $^1P$ discrete and continuum states. We have taken the oscillator strengths and energies for the $1s^2\ ^1S \rightarrow 1snp\ ^1P$ transitions from Refs. [35, 36] for $n \leq 9$ and used the asymptotic formula of Ref. [37] for $n > 9$. For the continuum states we used the TOPbase cross sections [38], which are trivially converted into oscillator strengths. The resulting $b_{2k+4}$ coefficients that we adopt for the rest of this work are shown in Table 4.1.

The radiative transfer equations also require the angular distribution and polarization of Rayleigh-scattered radiation. For scattering with initial and final states of zero orbital angular momentum ($S \rightarrow S$), and neglecting spin-orbit coupling, the scattering is of a pure "scalar" nature (in the language of Ref. [39] §61)

and has the same angular and polarization dependence as Thomson scattering, $dP/d\Omega \propto 1+\cos^2\theta$. Near a resonance such as Lyman-$\alpha$, fine structure splitting makes the electron spin important, and the scattering by hydrogen takes on a different form that is a combination of scalar, anti-symmetric, and symmetric scattering; the full equations for the angular scattering distribution as a function of frequency through the resonance can be found in e.g. Appendix B of Ref. [40]. The equations in Appendix B of Ref. [40] show that the angular distribution approaches the scalar case with corrections of order $\Delta\nu_{\rm fs}^2/(\nu_{{\rm Ly}\alpha}-\nu)^2$ as one moves away from the resonance, where the fine structure splitting is $\Delta\nu_{\rm fs}\sim 11\,{\rm GHz}$. For cases considered in this paper (frequencies up to 857 GHz observer frame, or $0.52\nu_{{\rm Ly}\alpha}$ at $z=1500$), we are thus safely below the lowest resonant frequency, and the scalar angular distribution – already incorporated in the CMB Boltzmann hierarchy formalism – is applicable.

## 4.3 Cosmological equations and proposed method

To include the effects of Rayleigh scattering on cosmological perturbations, we must modify the evolution equations for photon temperature, photon polarization and baryon velocity perturbations. We use synchronous gauge in this paper as it is convenient for most numerical computations. The full cosmological evolution equations in this gauge are given in a number of papers [22, 41], and therefore we only explicitly show the equations that need modification. In particular, using the Boltzmann equation in this gauge we find the evolution equations for the

temperature perturbation, $\Theta_I$, and E-polarization, $\Theta_E$, hierarchies are

$$\begin{aligned}
\dot{\Theta}_{I0} &= -k\Theta_{I1} + \frac{\dot{a}}{a}\nu\frac{\partial\Theta_{I0}}{\partial\nu} - \frac{\dot{h}}{6}, && (4.12)\\
\dot{\Theta}_{I1} &= \frac{k}{3}\Theta_{I0} - \frac{2k}{3}\Theta_{I2} + \frac{\dot{a}}{a}\nu\frac{\partial\Theta_{I1}}{\partial\nu} \\
&\quad -\dot{\kappa}[-\Theta_{I1} + \frac{1}{3}v_b], && (4.13)\\
\dot{\Theta}_{I2} &= \frac{2k}{5}\Theta_{I1} - \frac{3k}{5}\Theta_{I3} + \frac{\dot{a}}{a}\nu\frac{\partial\Theta_{I2}}{\partial\nu} + \frac{\dot{h}+6\dot{\eta}}{15} \\
&\quad -\dot{\kappa}[-\Theta_{I2} + \frac{1}{10}\Pi], && (4.14)\\
\dot{\Theta}_{Il} &= \frac{k}{2l+1}[l\Theta_{I(l-1)} - (l+1)\Theta_{I(l+1)}] \\
&\quad +\frac{\dot{a}}{a}\nu\frac{\partial\Theta_{Il}}{\partial\nu} + \dot{\kappa}\Theta_{Il} \qquad l \geq 3, && (4.15)\\
\dot{\Theta}_{E2} &= \frac{2k}{5}\Theta_{E1} - \frac{k}{3}\Theta_{E3} + \frac{\dot{a}}{a}\nu\frac{\partial\Theta_{E2}}{\partial\nu} \\
&\quad +\dot{\kappa}(\Theta_{E2} - \frac{2}{5}\Pi), && (4.16)\\
\dot{\Theta}_{El} &= \frac{k}{2l+1}[l\Theta_{E(l-1)} - \frac{(l+3)(l-1)}{l+1}\Theta_{E(l+1)}] \\
&\quad +\frac{\dot{a}}{a}\nu\frac{\partial\Theta_{El}}{\partial\nu} + \dot{\kappa}\Theta_{El} \qquad l \geq 3, && (4.17)
\end{aligned}$$

where an overdot denotes derivatives with respect to conformal time $\tau$, k is the wavenumber of the perturbations, $h$ and $\eta$ are the synchronous gauge metric perturbations, $\Pi$ is the combination $\Theta_{I2} + \frac{3}{2}\Theta_{E2}$, $a$ the scale factor and $\dot{\kappa}$ is the comoving opacity defined as

$$\begin{aligned}
-\dot{\kappa} &= -\dot{\kappa}_T - \dot{\kappa}_R \\
&= n_e\sigma_T a + n_H\sigma_R^H a + n_{He}\sigma_R^{He} a. && (4.18)
\end{aligned}$$

Here $n_e$, $n_H$ and $n_{He}$ are respectively the number densities of free electrons, neutral hydrogen and helium atoms. The comoving opacity for Rayleigh and Thomson scattering as a function of conformal time is plotted in Figure 4.1 for a couple of observed frequencies.

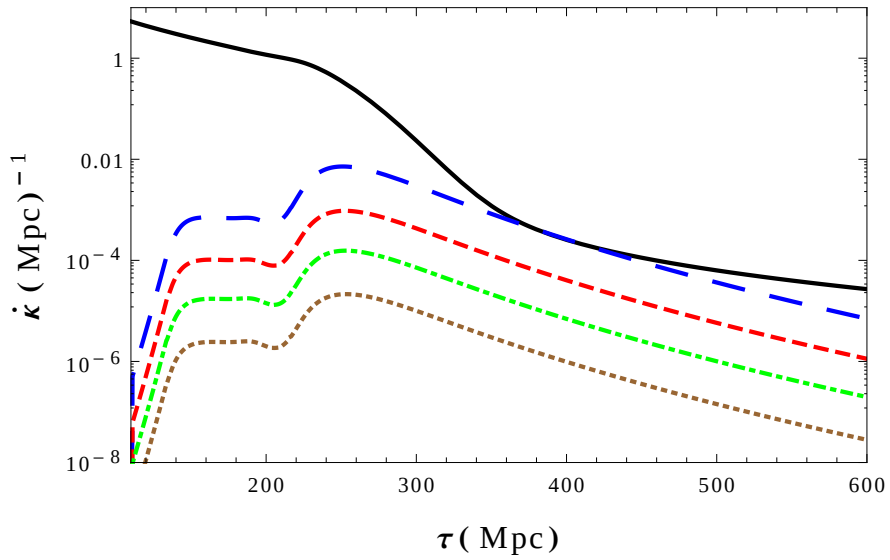


**Figure 4.1:** The Comoving opacity as a function of comoving time. The black (solid) line is for Thomson scattering while the blue (large dashed), red (small dashed), green (dot dashed) and brown (dotted) lines are for Rayleigh scattering at frequencies 857, 545, 353, and 217 GHz respectively.

In standard case when opacity does not depend on frequency, the baryons evolve according to equations

$$\dot{\delta}_b = -kv_b - \frac{1}{2}\dot{h}, \tag{4.19}$$

$$\begin{aligned} \dot{v_b} + \frac{\dot{a}}{a}v_b - kc_s^2\delta_b &= \frac{1}{\bar{\rho}_b}\int \frac{d^3p}{(2\pi)^3}(-p\mu)C[f(\vec{p})] \\ &= \frac{4\bar{\rho}_\gamma}{3\bar{\rho}_b}\dot{\kappa}(-3\Theta_{I1} + v_b), \end{aligned} \tag{4.20}$$

where $\delta_b$ and $v_b$ are baryon overdensity and velocity, $c_s$ is the intrinsic baryon sound speed, $f(p)$ is photon distribution function, $C[f(\vec{p})] = \frac{df}{dt}$ is the collision term in the Boltzmann equation for photon temperature perturbations, $\mu = \hat{p}\cdot\hat{k}$, and $\bar{\rho}_\gamma$ and $\bar{\rho}_b$ are the mean photon and baryon energy densities.

Including Rayleigh scattering will make the opacity frequency-dependent, therefore the scattering term in the baryon velocity must be modified to

$$\int \frac{d^3p}{(2\pi)^3}(-p\mu)C[f(\vec{p})] = \int \frac{d^3p}{(2\pi)^3}p^2\frac{\partial f}{\partial p}\mu\dot{\kappa}(p)(\Theta_{I0}(p)-\Theta_I(p)+\mu v_b). \tag{4.21}$$

As discussed above, a straightforward method to solve the above system of equations is to consider a separate Boltzmann hierarchy for each frequency of interest, each with different scattering sources and visibility function, and then integrate over each photon frequency bin to get the total baryon-photon coupling [31, 32]. However there is another computationally efficient method that can be used. If at the times that atoms are present the typical CMB photon energies are much smaller than Rydberg energy $h\nu \ll \mathrm{Ry}$, then we can write $\Theta_{Il}$ and $\Theta_{El}$ as Taylor series in the comoving frequency $a\nu$ where each term in the series describes spectral-distortion perturbations that scale with increasing powers of frequency. Specifically we write:

$$\Theta_{Il}(\nu) = \sum_{r=0}^{\infty}\Theta_{Il}^{(2r)}\left(\frac{ah\nu}{a_*\mathrm{Ry}}\right)^{2r}, \tag{4.22}$$

$$\Theta_{El}(\nu) = \sum_{r=0}^{\infty}\Theta_{El}^{(2r)}\left(\frac{ah\nu}{a_*\mathrm{Ry}}\right)^{2r}. \tag{4.23}$$

Note that only even powers of $\nu$ appear because the scattering cross section contains only even powers of $\nu$. We expanded the perturbations in terms of $ah\nu/a_*\mathrm{Ry}$ because this ratio does not evolve with time for a given photon and $a_* = 0.001$ is a reference epoch for normalizing the coefficients in the series expansion (its value has no physical consequences). Similarly we can write the opacity as

$$\dot{\kappa}(\nu) = \sum_{r=0}^{\infty}\dot{\kappa}_{2r}\left(\frac{ah\nu}{a_*\mathrm{Ry}}\right)^{2r}, \tag{4.24}$$

where $\dot{\kappa}_0 = -n_e\sigma_T a$ is the standard Thomson scattering rate, $\dot{\kappa}_1 = 0$ and

$$-\dot{\kappa}_{2r} = (n_H b_{2r}^H + n_{He}b_{2r}^{He})\sigma_T a\left(\frac{a_*}{a}\right)^{2r}. \tag{4.25}$$

Substituting these Taylor expansions into evolution equations for photon temperature and polarization perturbations leads to the following evolution equations for each $\Theta_{Il}^{(2n)}$ and $\Theta_{El}^{(2n)}$ terms:

$$\begin{aligned}
\dot{\Theta}_{I0}^{(2n)} &= -k\Theta_{I1}^{(2n)} - \frac{\dot{h}}{6}\delta_{n,0}, && (4.26)\\
\dot{\Theta}_{I1}^{(2n)} &= \frac{k}{3}\Theta_{I0}^{(2n)} - \frac{2k}{3}\Theta_{I2}^{(2n)} \\
&\quad - \sum_{r=0}^{n} \dot{\kappa}_{2r}[-\Theta_{I1}^{2(n-r)} + \frac{v_b}{3}\delta_{n-r,0}], && (4.27)\\
\dot{\Theta}_{I2}^{(2n)} &= \frac{2k}{5}\Theta_{I1}^{(2n)} - \frac{3k}{5}\Theta_{I3}^{(2n)} + \frac{\dot{h}+6\dot{\eta}}{15}\delta_{n,0} \\
&\quad - \sum_{r=0}^{n} \dot{\kappa}_{2r}[-\Theta_{I2}^{2(n-r)} + \frac{\Pi^{2(n-r)}}{10}], && (4.28)\\
\dot{\Theta}_{Il}^{(2n)} &= \frac{k}{2l+1}[l\Theta_{I(l-1)}^{(2n)} - (l+1)\Theta_{I(l+1)}^{(2n)}] \\
&\quad + \sum_{r=0}^{n} \dot{\kappa}_{2r}\Theta_{Il}^{2(n-r)} \qquad l \geq 3, && (4.29)
\end{aligned}$$

$$\begin{aligned}
\dot{\Theta}_{E2}^{(2n)} &= \frac{2k}{5}\Theta_{E1}^{(2n)} - \frac{k}{3}\Theta_{E3}^{(2n)} \\
&\quad + \sum_{r=0}^{n} \dot{\kappa}_{2r}[\Theta_{E2}^{2(n-r)} - \frac{2}{5}\Pi^{2(n-r)}], && (4.30)\\
\dot{\Theta}_{El}^{(2n)} &= \frac{k}{2l+1}[l\Theta_{E(l-1)}^{(2n)} - \frac{(l+3)(l-1)}{l+1}\Theta_{E(l+1)}^{(2n)}] \\
&\quad + \sum_{r=0}^{n} \dot{\kappa}_{2r}\Theta_{El}^{2(n-r)} \qquad l \geq 3. && (4.31)
\end{aligned}$$

To find the evolution equation for baryon velocity we first must calculate the following integral

$$\begin{aligned}
I_n &= -\frac{1}{4\bar{\rho}_\gamma T^n}\int_0^\infty \frac{d\nu}{2\pi^2}\nu^{n+4}\frac{\partial f}{\partial \nu} \\
&= \frac{15}{4\pi^4}(n+4)!\zeta[n+4], && (4.32)
\end{aligned}$$

where $\zeta$ is the Riemann $\zeta$-function. Therefore the baryon velocity in the presence of Rayleigh scattering evolves according to

$$\begin{aligned}\dot{v}_b &= -\frac{\dot{a}}{a}v_b + kc_s^2\delta_b \\ &\quad + \frac{4\bar{\rho}_\gamma}{3\bar{\rho}_b}\sum_{r=0}^{\infty}\dot{\kappa}_{2r}[-3\sum_{n=0}^{\infty}\Theta_{I1}^{(2n)}I_{2(n+r)}\left(\frac{aT}{a_*\mathrm{Ry}}\right)^{2(n+r)} \\ &\quad + v_b I_{2r}\left(\frac{aT}{a_*\mathrm{Ry}}\right)^{2r}]. \end{aligned} \tag{4.33}$$

As shown in Equation 4.4, the Rayleigh cross section blows up near the resonant frequencies. Therefore photons with these frequencies remain tightly coupled to baryons. Photons do not self interact so these resonant photons are unlikely to change the CMB power spectrum. However they do enhance the pressure or sound speed of baryons. There is typically of order 1 photon per baryon near the Lyman-$\alpha$ line and since the photon energy is 10.2 eV, and the baryon mass is 1 GeV, the baryon sound speed increases by roughly $10^{-8}$. This only alters perturbations at very small scales below those of interest in this work.

Since metric perturbation evolution depends on the total photon overdensity and velocity, the final modification is to calculate the change in the photon stress-energy tensor in the presence of frequency dependent scattering. The fractional photon energy density perturbation is

$$\begin{aligned}\delta_\gamma &= -\frac{1}{\bar{\rho}_\gamma}\int \nu^4 d\nu \frac{\partial f}{\partial \nu}\Theta_{I0}(\nu) \\ &= 4\sum_{r=0}^{\infty}\Theta_{I0}^{(2r)}I_{2r}\left(\frac{aT}{a_*\mathrm{Ry}}\right)^{2r}, \end{aligned} \tag{4.34}$$

and the photon momentum density is

$$\begin{aligned}\Theta_\gamma &= -\frac{3k}{4\bar{\rho}_\gamma}\int \nu^4 d\nu \frac{\partial f}{\partial \nu}\Theta_{I1}(\nu) \\ &= 3k\sum_{r=0}^{\infty}\Theta_{I1}^{(2r)}I_{2r}\left(\frac{aT}{a_*\mathrm{Ry}}\right)^{2r}. \end{aligned} \tag{4.35}$$

This appears to replace the problem of summing over many perturbations at dif-

ferent frequencies with summing over many perturbations with different spectral-distortion shapes. However, we find in practice that these sums rapidly converge after including only a few of the spectral-distortion terms which allows the entire system to be solved for efficiently and accurately.

For numerical computations we modified CAMB [24], a public Boltzmann code for anisotropies in CMB which calculates the theoretical matter and CMB power spectra given the cosmological parameters. We added the additional opacity due to Rayleigh scattering to this code as well as the evolution equations for spectral distortion terms $\Theta_{Il}^{(2n)}$ and $\Theta_{El}^{(2n)}$.

## 4.4 Matter power spectrum

One of the physical effects of Rayleigh scattering is a change in matter two-point correlation function. The matter correlation function is the excess probability, compared with what expected from a random distribution, of finding a matter over-density at a distance $\vec{r}$ apart and its Fourier transform is the matter power spectrum,

$$\xi(\vec{r}) = \langle \delta(\vec{x})\delta(\vec{x}+\vec{r})\rangle = \int \frac{d^3k}{(2\pi)^3} P(k) e^{i\vec{k}.\vec{r}}. \tag{4.36}$$

Rayleigh scattering increases the total baryon-photon coupling which delays the time of recombination. As shown in Figure 4.2, the correlation function has a peak near a radius of $\sim 150\,\mathrm{Mpc}$, the BAO scale, which represents the sound horizon at the time of recombination. This changes due to the delay in the time of photon-baryon decoupling. The percentage change in the two-point correlation function due to Rayleigh scattering is plotted in Figure 4.3. Adding Rayleigh scattering to the opacity changes the correlation function by up to $\sim 0.3\%$. Unless otherwise stated we show all results in a fiducial model where we adopt the best-fit parameters from PLANCK [30].

Another way of visualizing how much the matter power spectrum is changed in the presence of Rayleigh scattering is by looking at the evolution of a concentrated matter over-density in real space. In Figures 4.4 and 4.5, the redshift evaluation of a narrow Gaussian-shaped adiabatic density fluctuation in real space is displayed for baryons (blue) and photons (red).

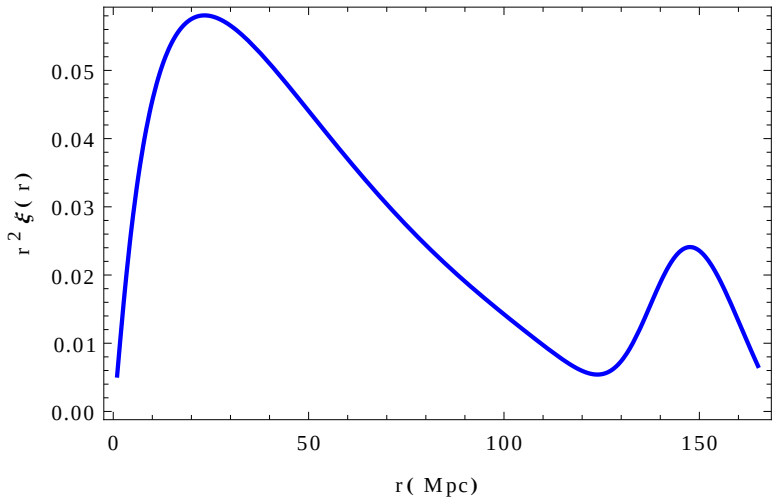


**Figure 4.2:** The matter two-point correlation function, $r^2\xi(\vec{r})$, as a function of the distance between two over-densities for our fiducial cosmological parameters.

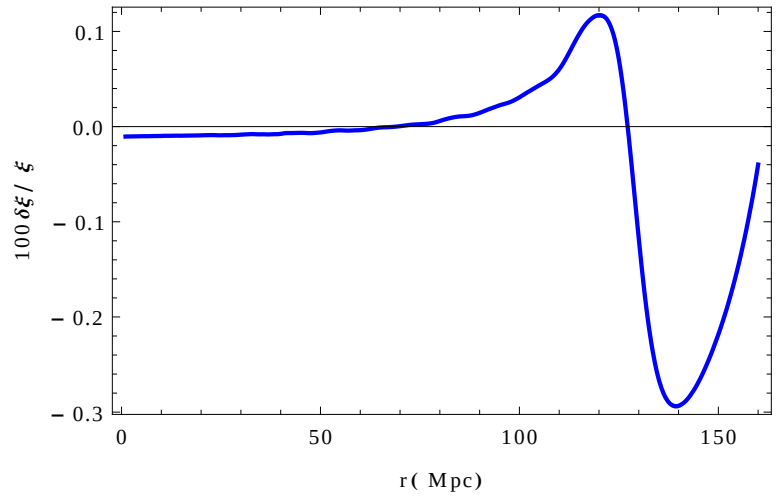


**Figure 4.3:** The percentage change in the matter correlation function due to Rayleigh scattering for our fiducial cosmological parameters.

At very early stages, when the photons and baryons were tightly coupled, panel (a), the baryon-photon plasma density wave travels outward from the initial over-density. Panel (b) shows a snapshot of the density waves at redshift $z = 1050$. At this time the temperature is low enough that neutral atoms can form, therefore the photons begin to decouple from baryons and the sound speed starts to drop. Thus the baryon density wave slows down compared to the photon density wave. In panel (c), the waves are shown at $z = 500$ when photons and baryons are completely decoupled. The photon perturbation smooths itself out at the speed of light. But because the sound speed is much smaller than speed of light the baryon density wave stalls. Panel (d) present the late time picture. The photons free-stream until now when we can observe them as the cosmic microwave background and the baryon perturbation clusters around the initial over-density and in a shell of about $\sim 150$ Mpc radius.

In Figure 4.6, the percentage change in physical baryon density fluctuations in real space due to Rayleigh scattering is plotted at different redshifts. Note that while $\Delta\delta/\delta$ is up to 0.6% at some points the percentage change in the location of the peak in baryon density wave or the BAO scale due to Rayleigh scattering is less than 0.01% in this example, and so the detailed effect of Rayleigh scattering is not well modelled as a simple shift in the BAO scale.

## 4.5 Photon power spectra

To calculate the power spectra for both photon temperature and E-polarization perturbations, we use the line of sight integration approach of Ref. [42]. In this approach, the solutions of Eqs. 4.26 to 4.31 can be written as an integral over the product of a source term and a geometrical term which is just the spherical Bessel function,

$$\Theta_{Il}(\tau_0) = \int_0^{\tau_0} d\tau S_I(k,\tau) j_l[k(\tau_0-\tau)], \tag{4.37}$$

$$\Theta_{El}(\tau_0) = \int_0^{\tau_0} d\tau S_E(k,\tau) j_l[k(\tau_0-\tau)]. \tag{4.38}$$

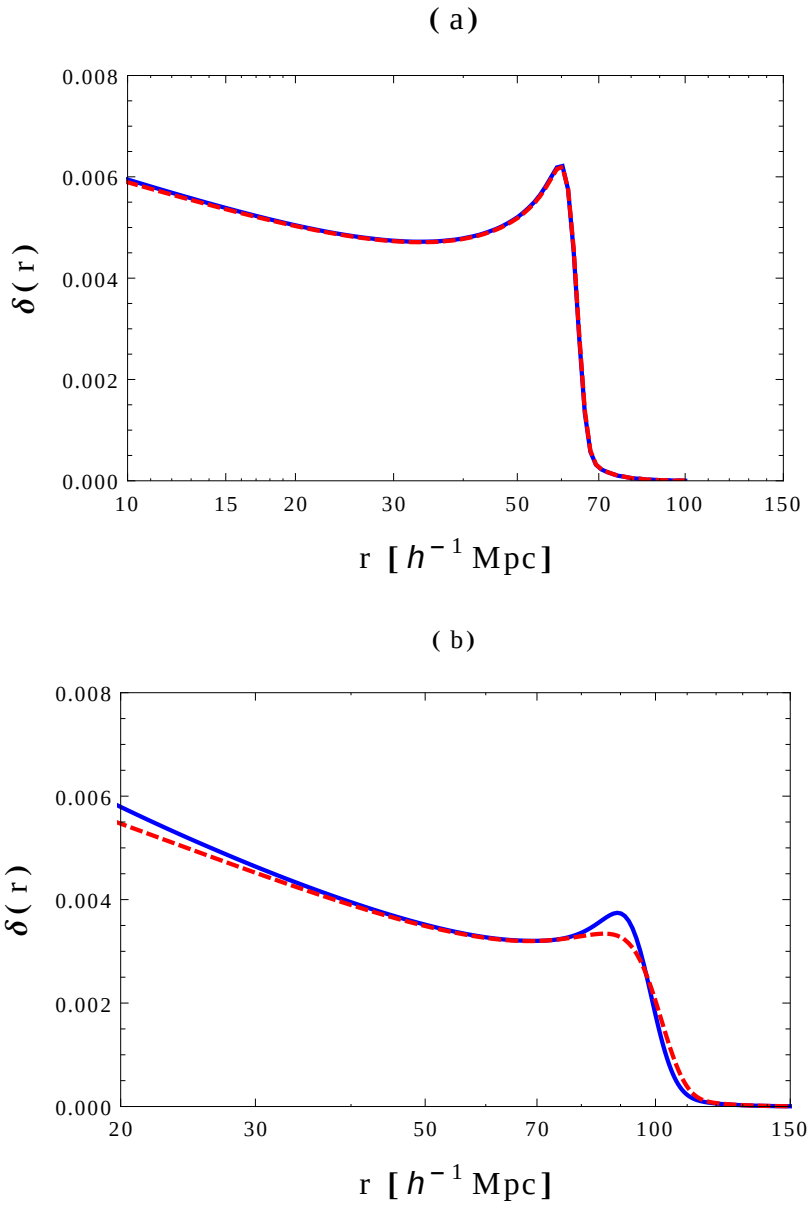


**Figure 4.4:** The redshift evaluation of a narrow Gaussian-shaped adiabatic density fluctuation in real space. The blue (solid) and red (dashed) lines are respectively the baryon and photon density waves. Panel(a) shows a snapshot at very early times when baryons and photons are tightly coupled and their density waves travel together. In panels (b), redshift $z = 1050$, photons begin to decouple from baryons and the baryon density wave slows down compare to photon density wave due to the drop in the sound speed.

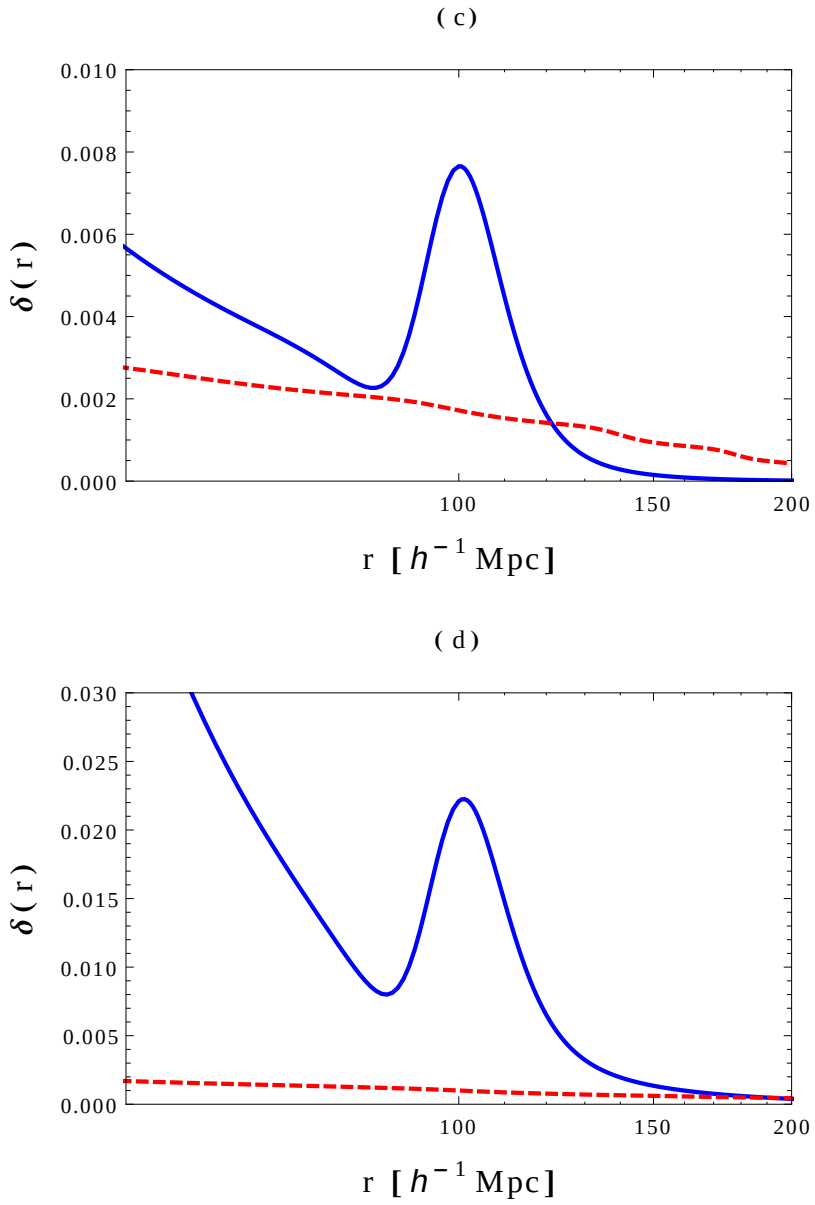


**Figure 4.5:** Same as 4.4 but for later redshifts. Panel (c) shows the density waves at redshift $z = 500$ where photons and baryons are completely decoupled. The late time picture is presented in panel (d). The photons free stream to us and baryons cluster around the initial over-density and in a shell at about 150 Mpc radius.

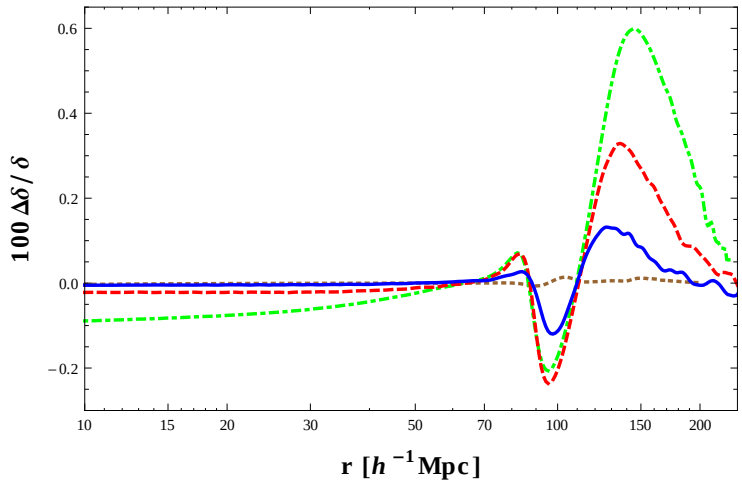


**Figure 4.6:** The percentage change in physical baryon density fluctuations in real space due to Rayleigh scattering at different redshifts. The blue (solid), red (dashed), green (dot dashed) and brown (dotted) lines correspond to redshifts 0, 100, 500 and 1050 respectively.

The source functions for temperature and E-polarization perturbations are given in many previous studies [41, 42].

$$\begin{aligned} S_I(k,\tau) &= e^{-\kappa}[-\frac{\dot{h}}{6}+\frac{k}{3}\sigma+\frac{\ddot{\sigma}}{k}] \\ &\quad +g(\tau)[2\frac{\dot{\sigma}}{k}+\Theta_{I0}+\frac{v_b}{k}+\frac{\Pi}{4}+\frac{3}{4k^2}\ddot{\Pi}] \\ &\quad +\dot{g}(\tau)[\frac{\sigma}{k}+\frac{v_b}{k}+\frac{3}{4k^2}2\dot{\Pi}]+\ddot{g}(\tau)\frac{3}{4k^2}\Pi^{(0)}, \end{aligned} \tag{4.39}$$

$$S_E(k,\tau) = g(\tau)\frac{3}{4}\Pi\frac{1}{[k(\tau_0-\tau)]^2}, \tag{4.40}$$

where $\sigma=(\dot{h}+6\dot{\eta})/2k$ and $g(\tau)=-\dot{\kappa}e^{-\kappa}$ is the visibility function. In the presence of Rayleigh scattering the visibility function is frequency dependent and can be written as a Taylor series in $ah\nu/a_*\mathrm{Ry}$. The total visibility function for several frequencies is plotted in Figure 4.7. Note that the total photon visibility function shifts toward later time with increasing frequencies.

Substituting the Taylor expansions of visibility function and temperature and

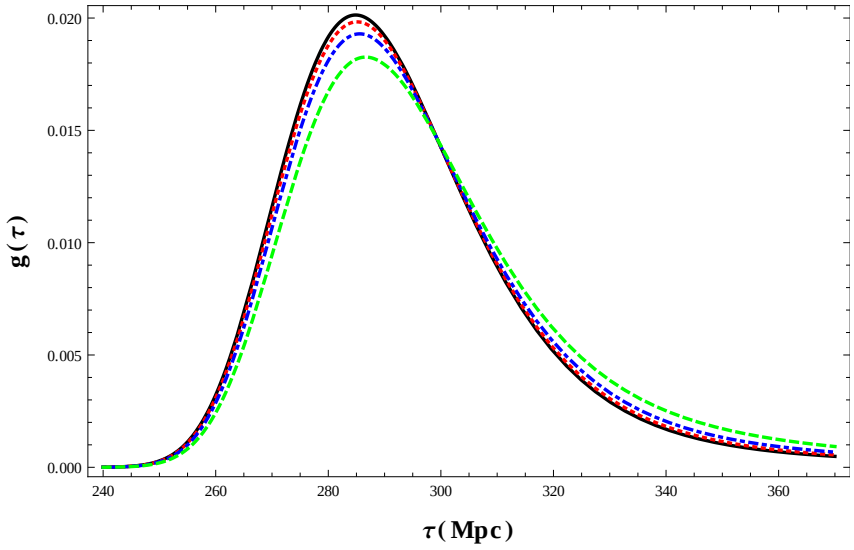


**Figure 4.7:** The total visibility function as a function of conformal time for several frequencies. The black (solid), red (dotted), blue (dot dashed) and green (dashed) lines are the total visibility function for frequencies 0, 545, 700 and 857 GHz respectively. The total photon visibility function shifts toward later times with increasing frequency.

E-polarization perturbations into the above equations gives the source functions for each of the $\Theta_{Il}^{(2n)}$ and $\Theta_{El}^{(2n)}$ terms,

$$\Theta_{Il}^{(2n)}(\tau_0) = \int_0^{\tau_0} d\tau S_I^{(2n)}(k,\tau) j_l[k(\tau_0-\tau)], \tag{4.41}$$

$$\Theta_{El}^{(2n)}(\tau_0) = \int_0^{\tau_0} d\tau S_E^{(2n)}(k,\tau) j_l[k(\tau_0-\tau)], \tag{4.42}$$

where

$$
\begin{aligned}
S_I^{(0)} &= e^{-\kappa_0}[-\frac{\dot{h}}{6}+\frac{k}{3}\sigma+\frac{\ddot{\sigma}}{k}]+g_0[2\frac{\dot{\sigma}}{k}+\Theta_{I0}^{(0)}+\frac{\dot{v}_b}{k}+\frac{\Pi^{(0)}}{4}+\frac{3}{4k^2}\ddot{\Pi}^{(0)}] \\
&\quad +\dot{g}_0[\frac{\sigma}{k}+\frac{v_b}{k}+\frac{3}{4k^2}2\dot{\Pi}^{(0)}]+\ddot{g}_0\frac{3}{4k^2}\Pi^{(0)}, \qquad (4.43) \\
S_I^{(4)} &= e^{-\kappa_0}[-\frac{\dot{h}}{6}+\frac{k}{3}\sigma+\frac{\ddot{\sigma}}{k}](-\kappa_4)+(g_0(-\kappa_4)+g_4) \\
&\quad \times[2\frac{\dot{\sigma}}{k}+\Theta_{I0}^{(0)}+\frac{\dot{v}_b}{k}+\frac{\Pi^{(0)}}{4}+\frac{3}{4k^2}\ddot{\Pi}^{(0)}]+g_0[\Theta_{I0}^{(4)}+\frac{\Pi^{(4)}}{4}+\frac{3}{4k^2}\ddot{\Pi}^{(4)}] \\
&\quad +(\dot{g}_0(-\kappa_4)+g_0(-\dot{\kappa}_4)+\dot{g}_4)[\frac{\sigma}{k}+\frac{v_b}{k}+\frac{3}{4k^2}2\dot{\Pi}^{(0)}]+\dot{g}_0\frac{3}{4k^2}2\dot{\Pi}^{(4)} \\
&\quad +\ddot{g}_0\frac{3}{4k^2}\Pi^{(4)}+[\ddot{g}_0(-\kappa_4)+2\dot{g}_0(-\dot{\kappa}_4)+g_0(-\ddot{\kappa}_4)+\ddot{g}_4]\frac{3}{4k^2}2\Pi^{(0)}, \qquad (4.44) \\
S_I^{(6)} &= e^{-\kappa_0}[-\frac{\dot{h}}{6}+\frac{k}{3}\sigma+\frac{\ddot{\sigma}}{k}](-\kappa_6)+(g_0(-\kappa_6)+g_6) \\
&\quad \times[2\frac{\dot{\sigma}}{k}+\Theta_{I0}^{(0)}+\frac{\dot{v}_b}{k}+\frac{\Pi^{(0)}}{4}+\frac{3}{4k^2}\ddot{\Pi}^{(0)}]+g_0[\Theta_{I0}^{(6)}+\frac{\Pi^{(6)}}{4}+\frac{3}{4k^2}\ddot{\Pi}^{(6)}] \\
&\quad +(\dot{g}_0(-\kappa_6)+g_0(-\dot{\kappa}_6)+\dot{g}_6)[\frac{\sigma}{k}+\frac{v_b}{k}+\frac{3}{4k^2}2\dot{\Pi}^{(0)}]+\dot{g}_0\frac{3}{4k^2}2\dot{\Pi}^{(6)} \\
&\quad +\ddot{g}_0\frac{3}{4k^2}\Pi^{(6)}+[\ddot{g}_0(-\kappa_6)+2\dot{g}_0(-\dot{\kappa}_6)+g_0(-\ddot{\kappa}_6)+\ddot{g}_6]\frac{3}{4k^2}2\Pi^{(0)}, \qquad (4.45) \\
S_E^{(0)} &= \frac{3}{4[k(\tau_0-\tau)]^2}g_0\Pi^{(0)}, \qquad (4.46) \\
S_E^{(4)} &= \frac{3}{4[k(\tau_0-\tau)]^2}(g_0[\Pi^{(4)}+\Pi^{(0)}(-\kappa_4)]+g_4\pi^{(0)}), \qquad (4.47) \\
S_E^{(6)} &= \frac{3}{4[k(\tau_0-\tau)]^2}(g_0[\Pi^{(6)}+\Pi^{(0)}(-\kappa_6)]+g_6\pi^{(0)}). \qquad (4.48)
\end{aligned}
$$

Here $g_{2r}=-\dot{\kappa}_{2r}e^{-\kappa_0}$. The anisotropy spectrum can be obtained by integrating over the initial power spectrum of the metric perturbation, $P_\psi(k)$:

$$
\begin{aligned}
C_l^{XY}(\nu,\nu') &= \int_0^\infty k^2 dk P_\psi(k)\left(\Theta_{Xl}(\nu,k)\Theta_{Yl}(\nu',k)\right) \qquad (4.49) \\
&= \sum_{r,r'=0}^{\infty} C_l^{XY(2r,2r')}\left(\frac{ah\nu}{a_*\mathrm{Ry}}\right)^{2r}\left(\frac{ah\nu'}{a_*\mathrm{Ry}}\right)^{2r'},
\end{aligned}
$$

where

$$C_l^{XY(2r,2r')} = \int_0^\infty k^2 dk P_\psi(k)(\Theta_{Xl}^{(2r)}(k)\Theta_{Yl}^{(2r')}(k)). \tag{4.50}$$

We used the modified version of CAMB [24] to numerically calculate $C_l^{TT(2r,2r')}$ and $C_l^{EE(2r,2r')}$ power spectra. These results are shown in Figure 4.8 and Figure 4.9. Note that while Eq. 4.50 describes unlensed power spectra from the surface of last scattering, here and elsewhere, these power spectra include the effect of gravitational lensing from structure along the line of sight implemented in CAMB.

Using Eq. 4.50, the relative difference in the (lensed) scalar CMB power spectra due to Rayleigh scattering is calculated for four different frequencies and presented in Figures 4.10 and 4.11. As expected, the relative difference in CMB power spectrum is bigger for higher frequencies. In the limit of very low frequencies the only modification in these power spectra arises from the increase in the total baryon-photon coupling due to Rayleigh scattering which is of order $0.05\%$.

On small scales, Rayleigh scattering leads to damping of both temperature and polarization anisotropies. Rayleigh scattering increases the rate of photon-baryon interaction and hence it reduces the photon-diffusion length. Since the amplitude of Silk damping depends on the integrated photon-diffusion length, it is also reduced by Rayleigh scattering. But there is another reason why the small-scale anisotropies are more damped in the presence of Rayleigh scattering. The damping factor at a given wave number is weighted by the photon visibility function. As we have seen above, adding Rayleigh scattering shifts the visibility function toward lower redshifts where Silk damping is more important and as a result, the anisotropy spectra at small scale decreases.

We also find Rayleigh scattering leads to a boost in large-scale E-polarization. The reason for this is that the low-multipole polarization signal is sourced by the CMB quadrupole. Since the visibility function is shifted toward later time, where the quadrupole is larger, by Rayleigh scattering the low-multipole E-polarization signal is increased. In contrast, the effect of Rayleigh scattering on the lensing B modes is significantly smaller at low-multipole because these modes are produced by the gravitational lensing of E modes from a wide range of scales, so the Rayleigh contribution for them partly averages out.

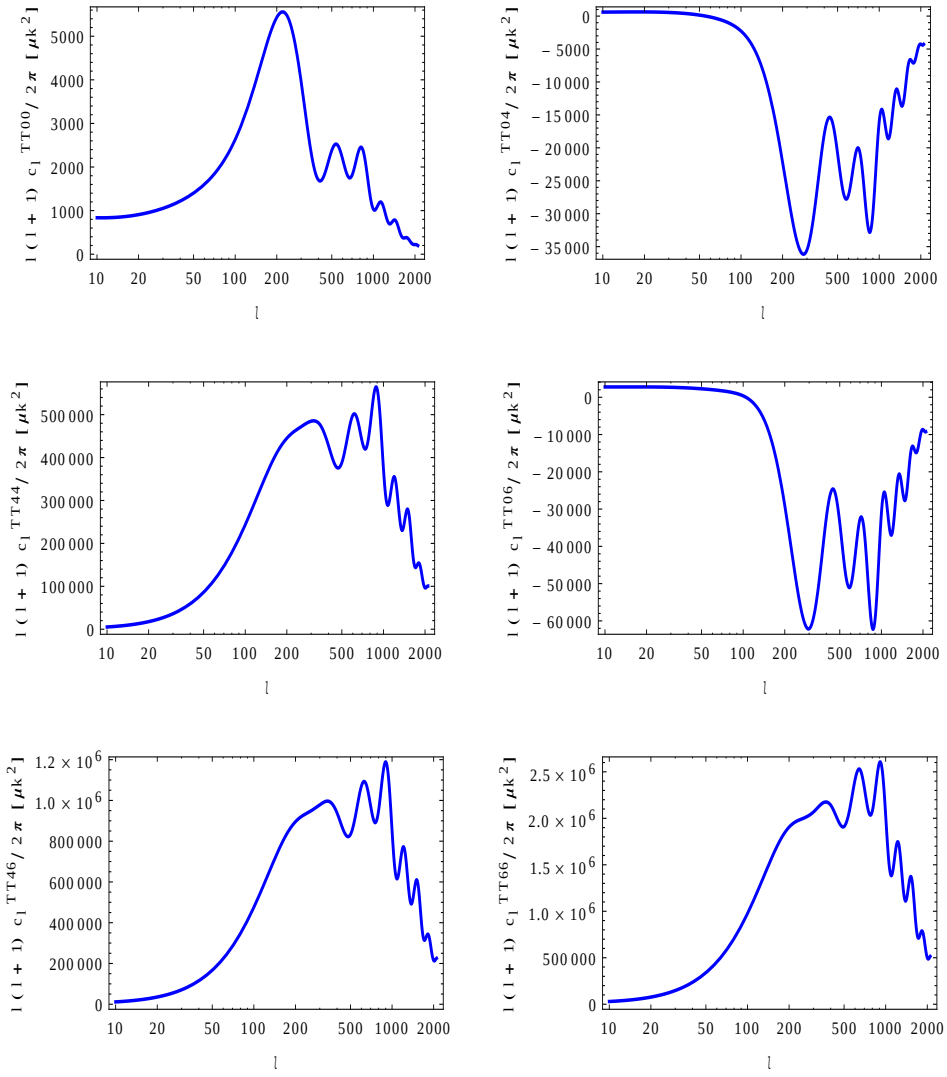


**Figure 4.8:** The cross correlation temperature power spectrum $C_l^{TT(2r,2r')}$ of the $\Theta_{Il}^{(2r)}$ and $\Theta_{Il}^{(2r')}$ intensity coefficients for the $\nu^0$, $\nu^4$ and $\nu^6$ spectral distortions.

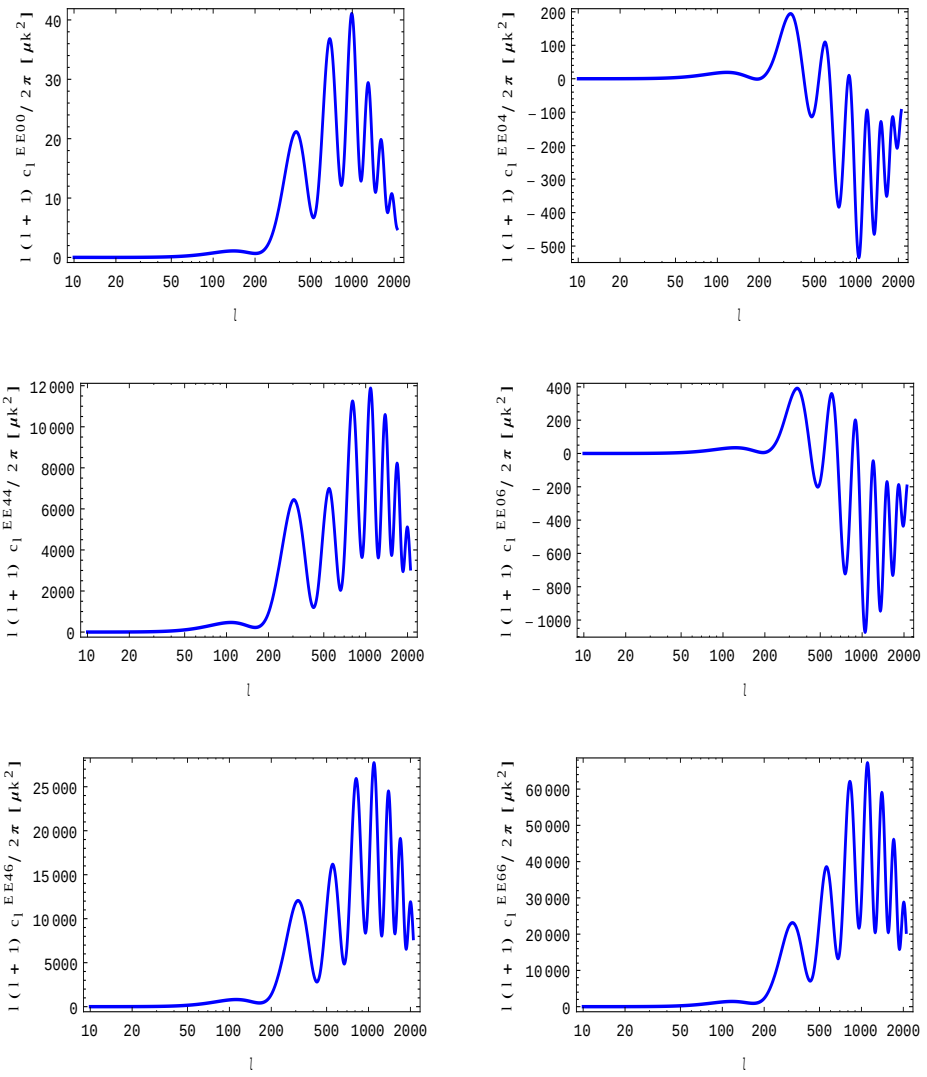


**Figure 4.9:** The cross correlation temperature power spectrum $C_l^{EE(2r,2r')}$ of the $\Theta_{El}^{(2r)}$ and $\Theta_{El}^{(2r')}$ E-polarization coefficients for the $\nu^0$, $\nu^4$ and $\nu^6$ spectral distortions.

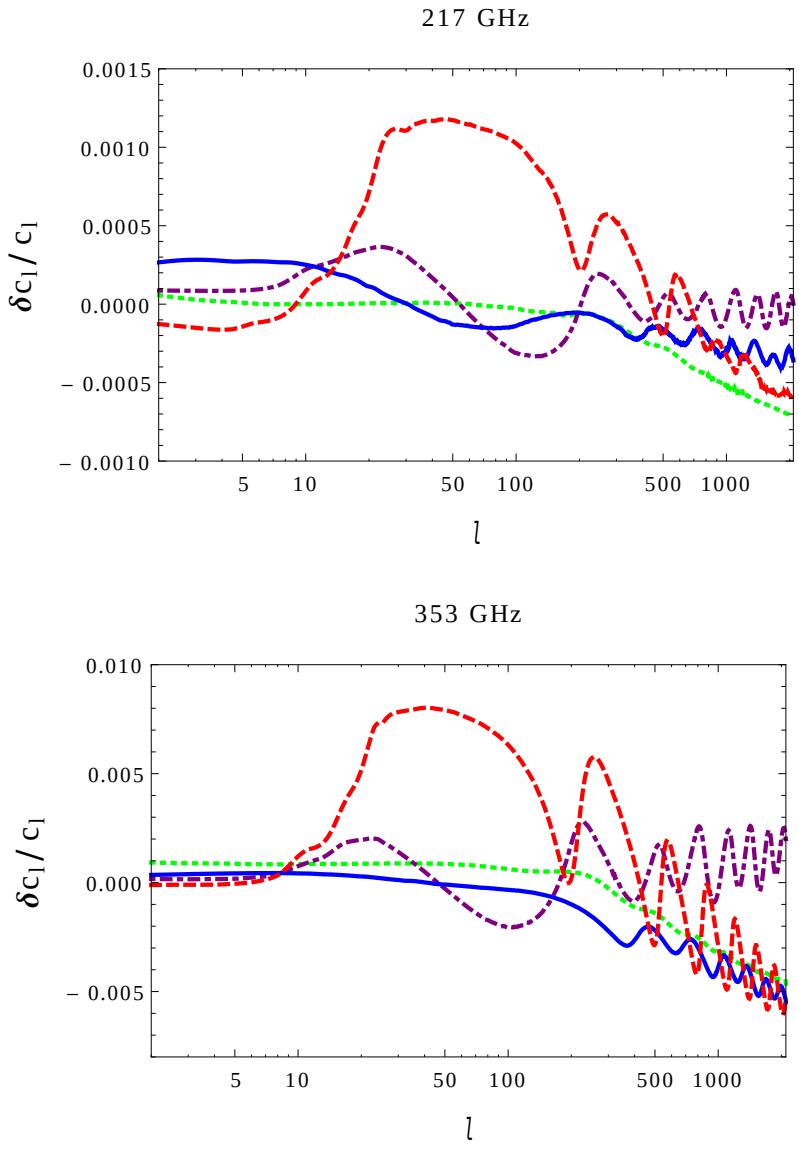


**Figure 4.10:** Shown are a fractional measure, $\delta C_l^{XY}/\sqrt{C_l^{XX}C_l^{YY}}$, of the change $\delta C_l^{XY}$ in (lensed) scalar CMB anisotropy spectra due to Rayleigh scattering. The blue (solid), red (dashed), green (dotted) and purple (dot dashed) are for the temperature, E-polarization, B-polarization from lensing and Temperature-E polarization cross-correlation spectra respectively. The upper and lower panels are for 217 and 353 GHz frequency channels respectively.

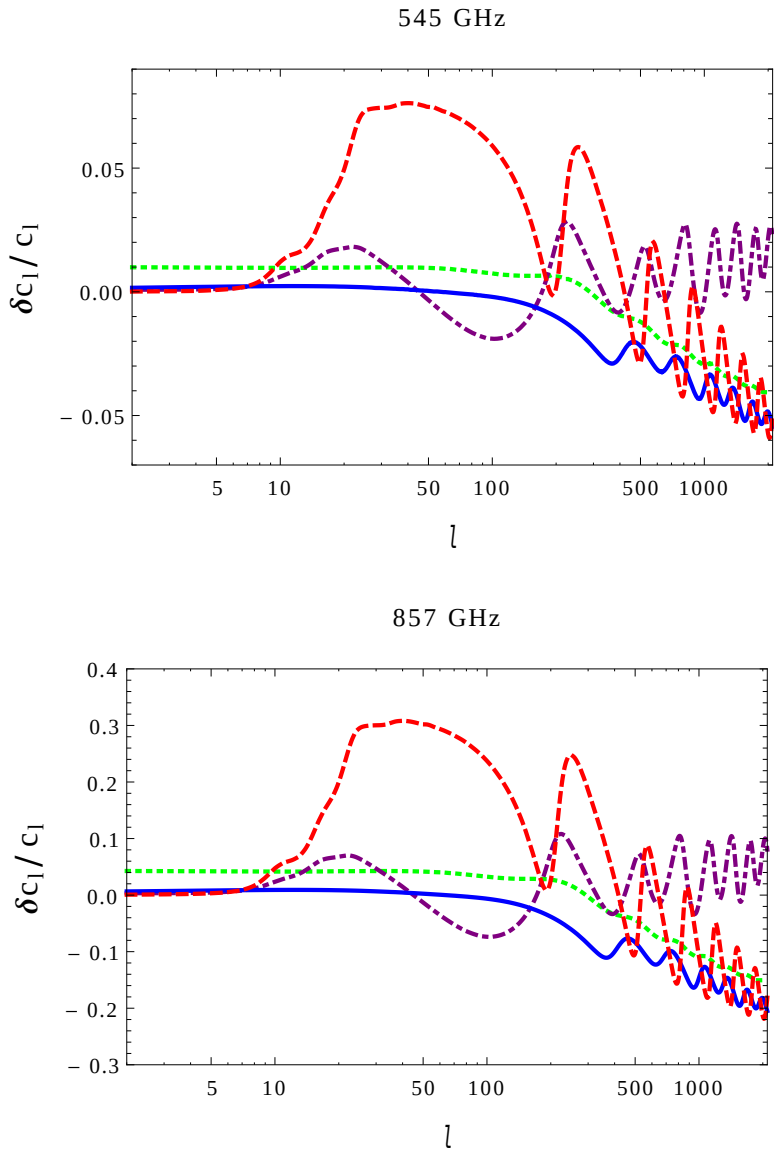


**Figure 4.11:** Same as 4.11 but for different frequency channels. The upper and lower panels are for 545 and 857 GHz frequency channels respectively.

Another effect worth noting is that, the oscillations of $\delta C_l/C_l$ show that the peaks in anisotropy spectra are shifted in the presence of Rayleigh scattering. Since the photon cross section is frequency dependent, the location of the surface of last scattering $\tau_*^{R+T}$ will depend on frequency too and the higher the frequency, the bigger $\tau_*^{R+T}(k,\nu)$. Therefore the sound horizon at the last scattering,

$$r_s^{R+T} = \int_0^{\tau_*^{R+T}} c_s d\tau, \tag{4.51}$$

will be larger than the sound horizon at last scattering when we only include the Thomson scattering $r_s^T$ and it will increase with increasing frequencies. The shift in the location of the peaks will be

$$\delta l/l = \delta k/k = 1 - r_s^{R+T}(\tau_*^{R+T})/r_s^T(\tau_*^T) \tag{4.52}$$

in the direction of decreasing $l$.

### 4.5.1 Convergence of the numerical code

We verify the convergence of the modified version of CAMB [24] by running several computations with increasing accuracy i.e. by increasing the accuracy-boost parameter in the code which decreases the time steps, affects the sampling, etc. In addition we justify the number of spectral distortion terms that we need to keep in Eqs. 4.22 and 4.23 by showing that keeping only the first five leading terms in these expansions results in an error smaller than 0.1%. To show this convergence, in 4.12 we plot the difference in the fractional change in the temperature power spectra when we include up to $\nu^n$ in Eqs. 4.22 and 4.23 compared to when we include up to $\nu^{n-2}$ terms and as shown, by increasing the terms kept in the expansion this difference becomes smaller and smaller.

## 4.6 Rayleigh Distorted Statistics

Since the terms in the expansion of temperature and E-polarization perturbations, Eqs. 4.22 and 4.23, fall off quickly like $(ah\nu/a_*\mathrm{Ry})^2$ only the two leading terms play an important role at frequencies smaller than 800 GHZ. We therefore

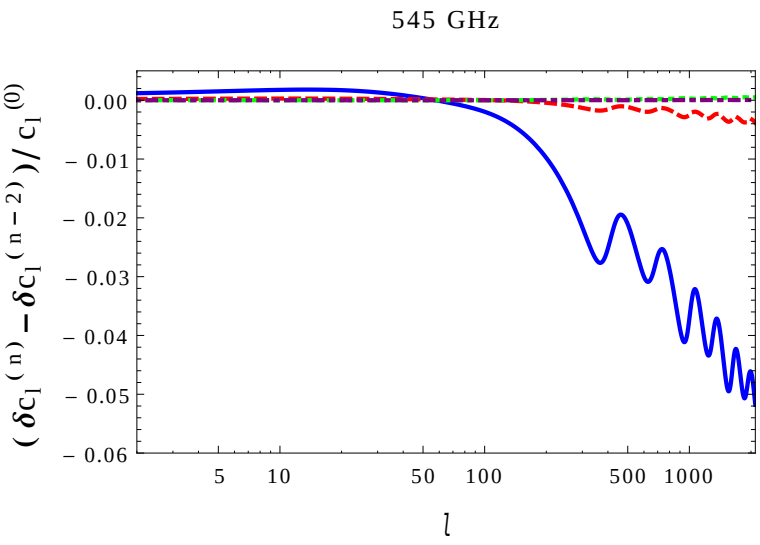


**Figure 4.12:** Shown are the difference in the fractional change, $\delta C_l^{TT}/C_l^{TT}$ in (lensed) scalar temperature CMB anisotropy spectra due to Rayleigh scattering for 545 GHZ frequency channel when we include up to $\nu^n$ in Eqs. 4.22 and 4.23 compared to when we include up to $\nu^{n-2}$ terms. The blue (solid), red (dashed), green (dotted) and purple (dot dashed) are for when $n = 4$, $n = 6$, $n = 8$ and $n = 10$ respectively and they justify the convergence of the expansions.

effectively need two sets of random variables to describe the statistics of temperature and E-polarization. In this section we find a compressed representation of the power spectra for independent random variables. First we introduce the antenna temperature which is defined as

$$T_{\rm ant}(\nu) = 2\pi\nu f(\nu), \tag{4.53}$$

where $f(\nu)$ is the photon phase space distribution function and $\nu$ is the frequency. For the CMB, the antenna temperature has the form

$$\frac{T_{\rm ant}(\nu)}{T} = \frac{h\nu/k_BT}{e^{h\nu/k_BT}-1} + \Theta\frac{(h\nu/k_BT)^2 e^{h\nu/k_BT}}{(e^{h\nu/k_BT}-1)^2}. \tag{4.54}$$

The first term is the monopole which does not interest us here and we ignore it. The second term gives the spectral shape of CMB anisotropies. Keeping only the first two non-zero terms in Eqs. 4.22 and 4.23, the antenna temperature for the CMB is

$$\frac{T^X_{\rm ant}(\nu)}{T} = \Theta^{(0)}_X F^{(0)}(\nu) + \Theta^{(4)}_X F^{(4)}(\nu), \tag{4.55}$$

where $F^{(0)}(\nu) = \frac{(h\nu/k_BT)^2 e^{h\nu/k_BT}}{(e^{h\nu/k_BT}-1)^2}$ is the black body shape function and $F^{(4)}(\nu) = (\frac{h\nu}{Ry})^4 F^{(0)}(\nu)$ is the shape function for the Rayleigh signal and X is either I for intensity perturbations or E for E-polarization perturbations. The angular power spectrum covariance matrix for the antenna temperature is

$$\begin{aligned} C_l^{XX}(\nu,\nu') &= C_l^{XX(00)} F^{(0)}(\nu) F^{(0)}(\nu') \\ &+ C_l^{XX(04)} (F^{(0)}(\nu) F^{(4)}(\nu') + F^{(4)}(\nu) F^{(0)}(\nu')) \\ &+ C_l^{XX(44)} F^{(4)}(\nu) F^{(4)}(\nu'). \end{aligned} \tag{4.56}$$

This structure indicates that $T_{\rm ant}(\nu)$ and $T_{\rm ant}(\nu')$ are correlated to each other but are not perfectly correlated like in the standard thermal case. We diagonalize the anisotropy spectrum in frequency space for a given $X \in \{I, E\}$ to obtain the two uncorrelated eigenvalues:

$$\begin{aligned} \lambda^{XX}_{1,2}(l) = \frac{1}{2}[&C_l^{XX(00)} G^{00} + 2C_l^{XX(04)} G^{04} + C_l^{XX(44)} G^{44} \\ &\pm \sqrt{(C_l^{XX(00)} G^{00} + 2C_l^{XX(04)} G^{04} + C_l^{XX(44)} G^{44})^2 - 4((C_l^{XX(04)})^2 - C_l^{XX(00)} C_l^{XX(44)})((G^{04})^2 - G^{00} G^{44})}], \end{aligned} \tag{4.57}$$

where $G^{ij} = \int F^{(i)}(\nu) F^{(j)}(\nu) d\nu$. The two orthogonal eigenvectors are

$$\begin{aligned} v^X_{1,2l}(\nu) &= N^X_{1,2}[(C_l^{XX(04)} \lambda^{XX}_{1,2} + C_l^{XX(00)} C_l^{XX(44)} G^{04} \\ &- (C_l^{XX(04)})^2 G^{04}) F^{(0)}(\nu) + (C_l^{XX(44)} \lambda^{XX}_{1,2} \\ &- C_l^{XX(00)} C_l^{XX(44)} G^{00} + (C_l^{XX(04)})^2 G^{00}) F^{(4)}(\nu)], \end{aligned} \tag{4.58}$$

where $N^X_{1,2}$ is the normalization factor. If we expand the antenna temperature in terms of spherical harmonics,

$$T^X_{\rm ant}(\nu)/T = \sum_{l=1}^{\infty} \sum_{m=-l}^{l} a^X_{lm} Y_{lm}, \tag{4.59}$$

then we can write the coefficients $a^X_{lm}$ in the new basis spanned by the eigenvectors $\{v^T_{1l}(\nu), v^T_{2l}(\nu), v^E_{1l}(\nu), v^E_{2l}(\nu)\}$,

$$a^X_{lm} = \alpha^X_{1lm} v^X_{1l}(\nu) + \alpha^X_{2lm} v^X_{2l}(\nu). \tag{4.60}$$

The covariance matrix in this new basis takes the compact form

$$\mathbf{C}_l \delta_{m,m'} = \begin{pmatrix} \mathbf{C}^I_l & \mathbf{C}^{IE}_l \\ \mathbf{C}^{IE}_l & \mathbf{C}^E_l \end{pmatrix} \delta_{m,m'} = \tag{4.61}$$

$$\begin{pmatrix} \langle \alpha^I_{1lm} \alpha^I_{1lm'} \rangle & 0 & \langle \alpha^I_{1lm} \alpha^E_{1lm'} \rangle & \langle \alpha^I_{1lm} \alpha^E_{2lm'} \rangle \\ 0 & \langle \alpha^I_{2lm} \alpha^I_{2lm'} \rangle & \langle \alpha^I_{2lm} \alpha^E_{1lm'} \rangle & \langle \alpha^I_{2lm} \alpha^E_{2lm'} \rangle \\ \langle \alpha^E_{1lm} \alpha^I_{1lm'} \rangle & \langle \alpha^E_{1lm} \alpha^I_{2lm'} \rangle & \langle \alpha^E_{1lm} \alpha^E_{1lm'} \rangle & 0 \\ \langle \alpha^E_{2lm} \alpha^I_{1lm'} \rangle & \langle \alpha^E_{2lm} \alpha^I_{2lm'} \rangle & 0 & \langle \alpha^E_{2lm} \alpha^E_{2lm'} \rangle \end{pmatrix}.$$

Using this diagonalization, we reduced the number of power spectra needed to describe the theoretical CMB covariance matrix from 10 to 8. These 8 non-zero elements in the covariance matrix are shown in Figures 4.13 to 4.16. $\langle \alpha^I_{1lm} \alpha^I_{1lm'} \rangle$ and $\langle \alpha^E_{1lm} \alpha^E_{1lm'} \rangle$ are almost proportional to the primary thermal signal (no Rayleigh scattering included) and we call them the primary temperature and polarization signal. The second eigenvalues of intensity and polarization spectra $\langle \alpha^I_{2lm} \alpha^I_{2lm'} \rangle$ and $\langle \alpha^E_{2lm} \alpha^E_{2lm'} \rangle$, which are due purely to Rayleigh scattering and uncorrelated to the first eigenvalues, we call the Rayleigh intensity and E-polarization signal. Note that since intensity and E-polarization perturbations must be separately diagonalized their eigenvectors are not orthogonal to each other. Thus all possible temperature-polarization cross-spectra are non-zero and present in Figures 4.15 and 4.16.

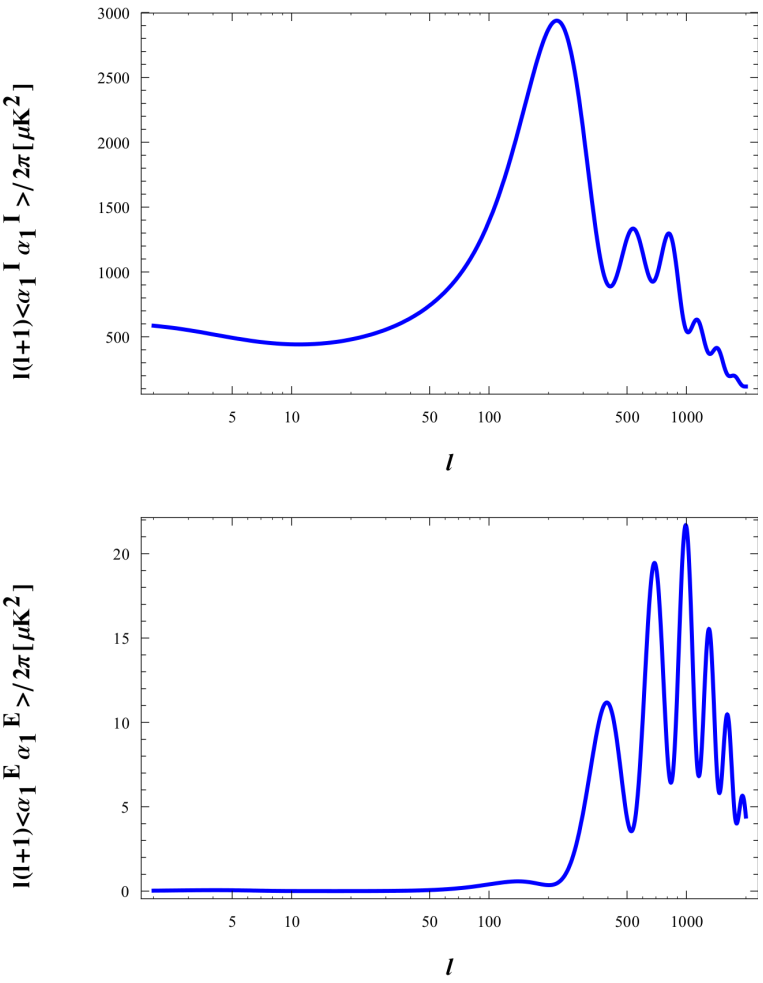


**Figure 4.13:** The non-zero power spectra in the Rayleigh distorted CMB covariance matrix as a function of l. The upper and lower panels show the first eigenvalues of intensity and polarization spectra respectively which are almost proportional to the primary thermal signal.

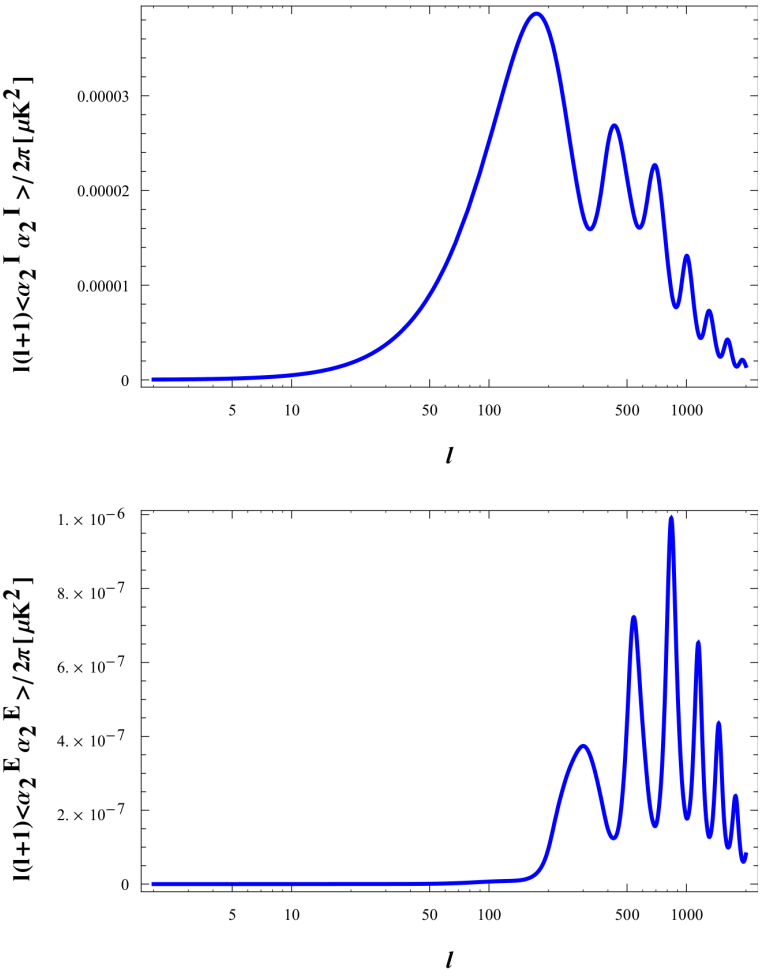


**Figure 4.14:** Same as 4.13 but for the second eigenvalues of intensity (upper panel) and polarization (lower panel). Note that the second eigenvalues are purely Rayleigh signals which are uncorrelated to the first eigenvalues.

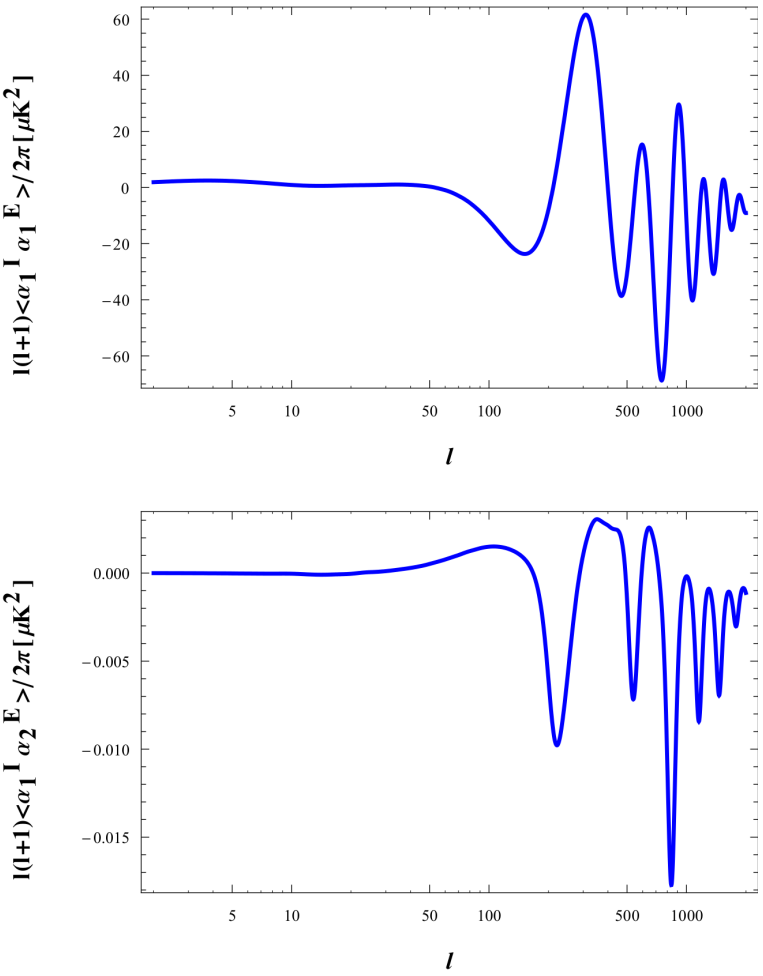


**Figure 4.15:** Same as 4.13 but for temperature-polarization cross-spectra. The upper and lower panels present $\langle \alpha^I_{1lm} \alpha^E_{1lm'} \rangle$ and $\langle \alpha^I_{1lm} \alpha^E_{2lm'} \rangle$ as a function of $l$ respectively.

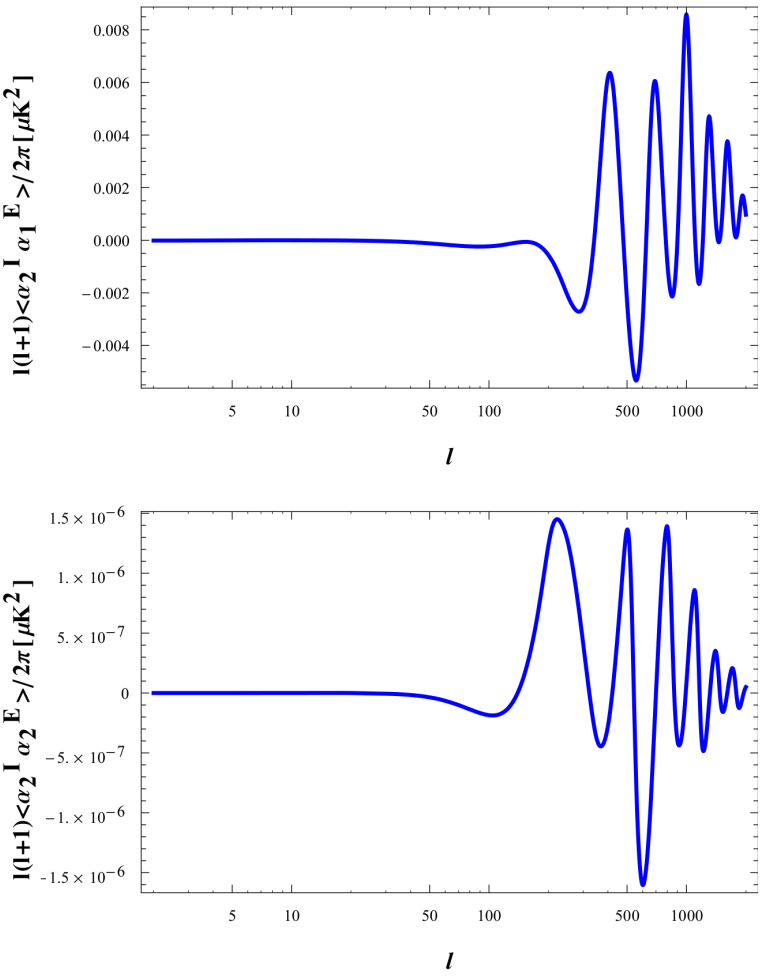


**Figure 4.16:** Same as 4.13 but for temperature-polarization cross-spectra. The upper and lower panels show $\langle \alpha^I_{2lm} \alpha^E_{1lm'} \rangle$ and $\langle \alpha^I_{2lm} \alpha^E_{2lm'} \rangle$ as a function of $l$ respectively.

## 4.7 Detectibility

Measurement of the Rayleigh signal is very challenging since at high frequencies that Rayleigh scattering becomes important, there are very few photons and very high levels of foreground contamination including Galactic dust, and the Cosmic Infrared Background (CIB). Yet if many high frequency channels are measured in future CMB missions, in principle, foregrounds can be removed. The reason for this is that the spectral shape of foregrounds are different from one another and from the spectral shape of the Rayleigh signal. In addition, the Rayleigh power spectrum looks very different from all the foregrounds since it's oscillatory and it spans the full range of scales whereas most of the foregrounds are important either at lower or higher l values. For example, the CIB and thermal Sunyaev-Zel'dovich have small amplitudes at large scales but larger amplitudes at smaller scales, while Galactic dust is important at lower $l$ and is less so at higher $l$. A future CMB mission that could be a candidate for detecting the Rayleigh signal is one similar to the proposed PRISM experiment [6], which has many high frequency bands with more than 7000 detectors. In this section we take a PRISM-like experiment as an example of what capabilities a next generation CMB satellite might have and explore the detectibility of the Rayleigh signal with this experiment.

### 4.7.1 Signal to noise ratio of Rayleigh signal

Our goal is to find the signal-to-noise ratio for the 8 non-zero elements of the CMB covariance matrix. As an example, we use the foreground removal method described in Ref. [25] and closely follow its notation. In this method, the foregrounds are treated as an additional source of noise which is correlated between frequency channels. If the frequency dependence, the scale dependence and also the variation in frequency dependence across sky are known for each physical component of foregrounds, this leads to a natural way of removing them.

Let's say that our experiment has F frequency channels. The F-dimensional vectors $\mathbf{a}^I_{lm}$ and $\mathbf{a}^E_{lm}$, which are the measured multipoles at F different frequencies, are assumed to be composed of signal plus noise:

$$\mathbf{y}_{lm} = \mathbf{A}_l \mathbf{x}_{lm} + \mathbf{n}_{lm}, \tag{4.62}$$

$$\mathbf{y}_{lm} = \begin{pmatrix} \mathbf{a}^I_{lm} \\ \mathbf{a}^E_{lm} \end{pmatrix}, \qquad \mathbf{x}_{lm} = \begin{pmatrix} \alpha^I_{1lm} \\ \alpha^I_{2lm} \\ \alpha^E_{1lm} \\ \alpha^E_{2lm} \end{pmatrix}, \tag{4.63}$$

$$\mathbf{A}_l = \begin{pmatrix} \mathbf{v}^I_{1l}(\nu) & \mathbf{v}^I_{2l}(\nu) & 0 & 0 \\ 0 & 0 & \mathbf{v}^E_{1l}(\nu) & \mathbf{v}^E_{2l}(\nu) \end{pmatrix}. \tag{4.64}$$

$\mathbf{A}_l$ is the $2F \times 4$ scan strategy matrix for a given (l,m). $\mathbf{n}_{lm}$ is the sum of detector noise and K different foreground components such as Galactic dust, synchroton emission or CIB. The covariance matrix for the noise is obtained by

$$\boldsymbol{N}_l = \begin{pmatrix} \mathbf{N}^I_l & \mathbf{N}^{IE}_l \\ \mathbf{N}^{IE}_l & \mathbf{N}^E_l \end{pmatrix}, \tag{4.65}$$

where $\mathbf{N}^X_l = \sum_{k=1}^{K+1} \mathbf{C}^X_l(k)$ is a $F \times F$ matrix. $\mathbf{C}^X_l(k=1)$ is the covariance matrix for detector noise, and $\mathbf{C}^X_l(k)$ is the angular power spectrum for different foreground components.

To see how accurately we can remove the foregrounds and measure the CMB power spectra $\mathbf{x}_{lm}$, we need to invert the noisy linear problem of Eq. 4.62. It's shown in Ref. [43] that the minimum-variance estimate of the $\mathbf{x}_{lm}$ is $\tilde{\mathbf{x}}_{lm} = \boldsymbol{W}^t_l \mathbf{y}_{lm}$ where

$$\begin{aligned} \boldsymbol{W}_l &= \boldsymbol{N}_l^{-1}\mathbf{A}_l[\mathbf{A}^t_l \boldsymbol{N}_l^{-1}\mathbf{A}_l]^{-1} \\ &= \begin{pmatrix} \mathbf{w}^I_{1l} & \mathbf{w}^I_{2l} & \mathbf{w}^E_{1l} & \mathbf{w}^E_{2l} \\ \mathbf{w}^{I'}_{1l} & \mathbf{w}^{I'}_{2l} & \mathbf{w}^{E'}_{1l} & \mathbf{w}^{E'}_{2l} \end{pmatrix}. \end{aligned} \tag{4.66}$$

$\mathbf{w}^X_{il}$ are the F-dimensional weight vectors where

$$\begin{aligned} \tilde{\alpha}^I_{ilm} &= \mathbf{w}^{It}_{il}\mathbf{a}^I_{lm} + \mathbf{w}^{I't}_{il}\mathbf{a}^E_{lm}, \\ \tilde{\alpha}^E_{ilm} &= \mathbf{w}^{Et}_{il}\mathbf{a}^E_{lm} + \mathbf{w}^{E't}_{il}\mathbf{a}^I_{lm}. \end{aligned} \tag{4.67}$$

The weight vectors are different for each l-value, so that at each angular scale, the frequency channels with smaller foregrounds contribution have more weight.

The estimated solution $\tilde{\mathbf{x}}_{lm}$ is unbiased such that $\langle\tilde{\mathbf{x}}_{lm}\rangle = \mathbf{x}_{lm}$ and the covariance matrix of the pixel noise $\varepsilon_{lm} = \tilde{\mathbf{x}}_{lm} - \mathbf{x}_{lm}$ is $\Sigma_l \delta_{m,m'} = \langle\varepsilon_{lm}\varepsilon^t_{lm'}\rangle$ where

$$\Sigma_l = [\mathbf{A}_l^t \boldsymbol{N}_l^{-1} \mathbf{A}_l]^{-1} = \begin{pmatrix} \tilde{\mathbf{N}}_l^I & \tilde{\mathbf{N}}_l^{IE} \\ \tilde{\mathbf{N}}_l^{IE} & \tilde{\mathbf{N}}_l^E \end{pmatrix}. \tag{4.68}$$

Here $\tilde{\mathbf{N}}_l^I$, $\tilde{\mathbf{N}}_l^E$ and $\tilde{\mathbf{N}}_l^{IE}$ are $2\times 2$ cleaned power spectrum matrices of the non-cosmic signals. The covariance matrix of our estimate $\tilde{\mathbf{x}}_{lm}$ is

$$\tilde{\mathbf{C}}_l \delta_{m,m'} = \langle\tilde{\mathbf{x}}^*_{lm}\tilde{\mathbf{x}}^t_{lm}\rangle = \begin{pmatrix} \tilde{\mathbf{C}}_l^I & \tilde{\mathbf{C}}_l^{IE} \\ \tilde{\mathbf{C}}_l^{IE} & \tilde{\mathbf{C}}_l^E \end{pmatrix} \delta_{m,m'}, \tag{4.69}$$

where $\tilde{\mathbf{C}}_l^X = \mathbf{C}_l^X + \tilde{\mathbf{N}}_l^X$ is the total power spectrum in the cleaned maps. To find how accurately we can measure any of the eight non-zero element of cosmic power spectrum, we must compute the $8\times 8$ Fisher matrix:

$$\mathbf{F}_{l\alpha\beta} = \frac{1}{2} Tr[\tilde{\mathbf{C}}_l^{-1} \frac{\partial\tilde{\mathbf{C}}_l}{\partial\alpha} \tilde{\mathbf{C}}_l^{-1} \frac{\partial\tilde{\mathbf{C}}_l}{\partial\beta}], \tag{4.70}$$

where $\alpha$ and $\beta$ could be any of the 8 non-zero elements. Up this point, we have used only one multipole $\mathbf{x}_{lm}$ to calculate the Fisher matrix, but for each l-value we have $(2l+1)f_{\rm sky}$ independent modes where $f_{\rm sky}$ is the fraction of sky covered. Therefore the full Fisher matrix is $(2l+1)f_{\rm sky}$ times what we calculated in Eq 4.70. Inverting this matrix gives the constraints on the 8 non-zero elements of the cosmic covariance matrix.

We compute this Fisher matrix for a PRISM-like experiment with the same frequency channels between 30GHz and 800GHz as PRISM. For the noise, we choose the resolution to be 1 arc min and the sensitivity to be 1nK for channels with frequencies less than 500GHz and 10nK for channels with frequencies higher than 500GHz. For the dominant foreground components, the temperature and E-polarization power spectra of Galactic dust and the temperature power spectra of CIB, we used the power spectra given in a series of Planck papers [44–47]. For other foreground components which are subdominant for detecting the Rayleigh signal, we used the power spectra given in Table 2 of Ref. [25]. The eight non-zero

elements and their signal-to-noise ratio for each l value as well as accumulative signal-to-noise ratio are plotted in Figures 4.17 to 4.20.

Since the power spectra $\langle \alpha^I_{1lm} \alpha^I_{1lm'} \rangle$, $\langle \alpha^E_{1lm} \alpha^E_{1lm'} \rangle$ and $\langle \alpha^I_{1lm} \alpha^E_{1lm'} \rangle$ are almost the same as the primary thermal signal, their signal-to-noise ratio is huge. For the auto correlation of the primary temperature and E-polarization, the signal-to-noise ratio is almost equal to the cosmic variance limit up to $l = 2000$. Among the remaining elements, $\langle \alpha^I_{1lm} \alpha^E_{2lm'} \rangle$ and $\langle \alpha^I_{2lm} \alpha^E_{1lm'} \rangle$ have larger accumulative signal-to-noise ratios and these two are detectable for this PRISM-like experiment. The accumulative signal-to-noise for $\langle \alpha^I_{1lm} \alpha^E_{2lm'} \rangle$ is almost 5.4 and for $\langle \alpha^I_{2lm} \alpha^E_{1lm'} \rangle$ is around 5.2. If we do not include the Rayleigh scattering, these two signals are zero. Detecting them to be non-zero would be an interesting and non-trivial cross check of the CMB physics and the assumed cosmological model.

### 4.7.2 Constraints on Cosmological Parameters

There is independent information contained in the Rayleigh signal which might help to better constrain the cosmological parameters. To show how much potential information we can get from the Rayleigh signal, we consider an ideal experiment with no foregrounds and negligible detector noise so that the signal-to-noise ratios for both the primary and Rayleigh signals are cosmic-variance limited. To find the constraints on seven cosmological parameters, $\Omega_b, \Omega_c, \tau, n_s, A_s, H, Y_p$, we calculate the Fisher matrix using the standard equation:

$$\mathbf{F}_{ij} = \sum_l^{l_{\max}} (2l+1) f_{\rm sky} \frac{1}{2} Tr[\tilde{\mathbf{C}}_l^{-1} \frac{\partial \tilde{\mathbf{C}}_l}{\partial p_i} \tilde{\mathbf{C}}_l^{-1} \frac{\partial \tilde{\mathbf{C}}_l}{\partial p_j}], \tag{4.71}$$

where $p_i$ and $p_j$ could be any of the seven cosmological parameters considered. The constraints on cosmological parameters for the cosmic-variance limited experiment are presented in Table 4.2. Note that in this calculation we only included moments up to $l_{\max} = 2000$. In principle the extra information contained in the Rayleigh sky is quite powerful. For instance, adding the Rayleigh signal potentially could help to improve the constraint on the helium fraction $Y_p$ by a factor of four. Furthermore, the fundamental limit on $n_s$ from the CMB only is less than $10^{-3}$ which could be of interest for inflation studies.

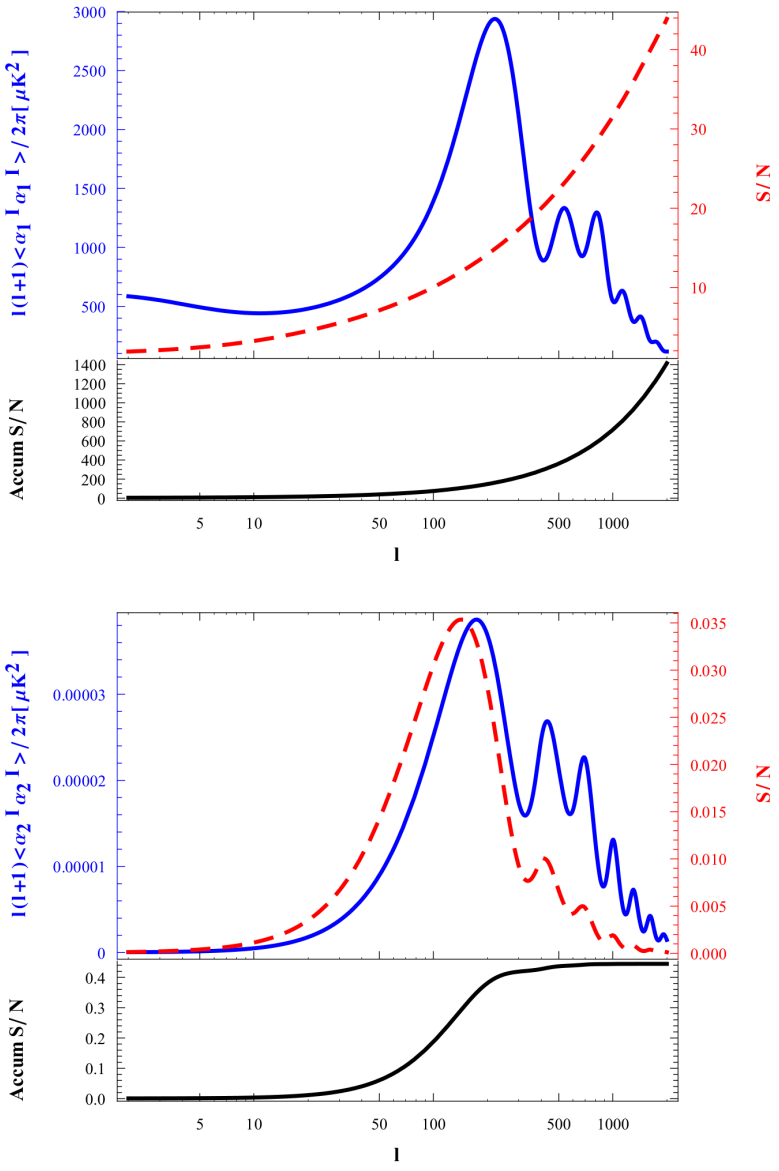


**Figure 4.17:** The first eigenvalues of intensity $\langle \alpha^I_{1lm} \alpha^I_{1lm'} \rangle$ and polarization $\langle \alpha^E_{1lm} \alpha^E_{1lm'} \rangle$ spectra (blue, solid) and their signal-to-noise ratio at each l (red, dashed) as well as the accumulative signal-to-noise ratio for the PRISM-like experiment. Note that the signal-to-noise ratio for the temperature-polarization cross power spectrum can be negative at some l values due to anti-correlation of the temperature and polarization. However the accumulative signal-to-noise, added in quadrature, is always positive.

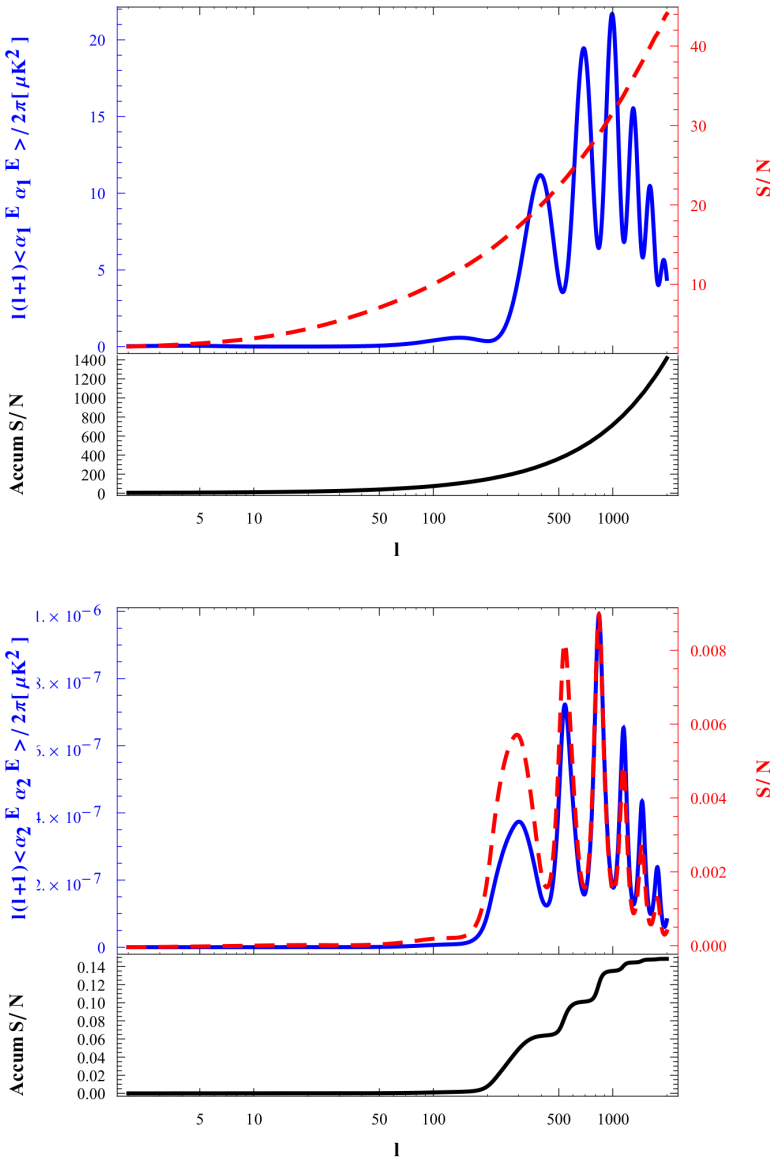


**Figure 4.18:** Same as 4.17 but for the second eigenvalues of intensity $\langle \alpha^I_{2lm} \alpha^I_{2lm'} \rangle$ and polarization $\langle \alpha^E_{2lm} \alpha^E_{2lm'} \rangle$ spectra.

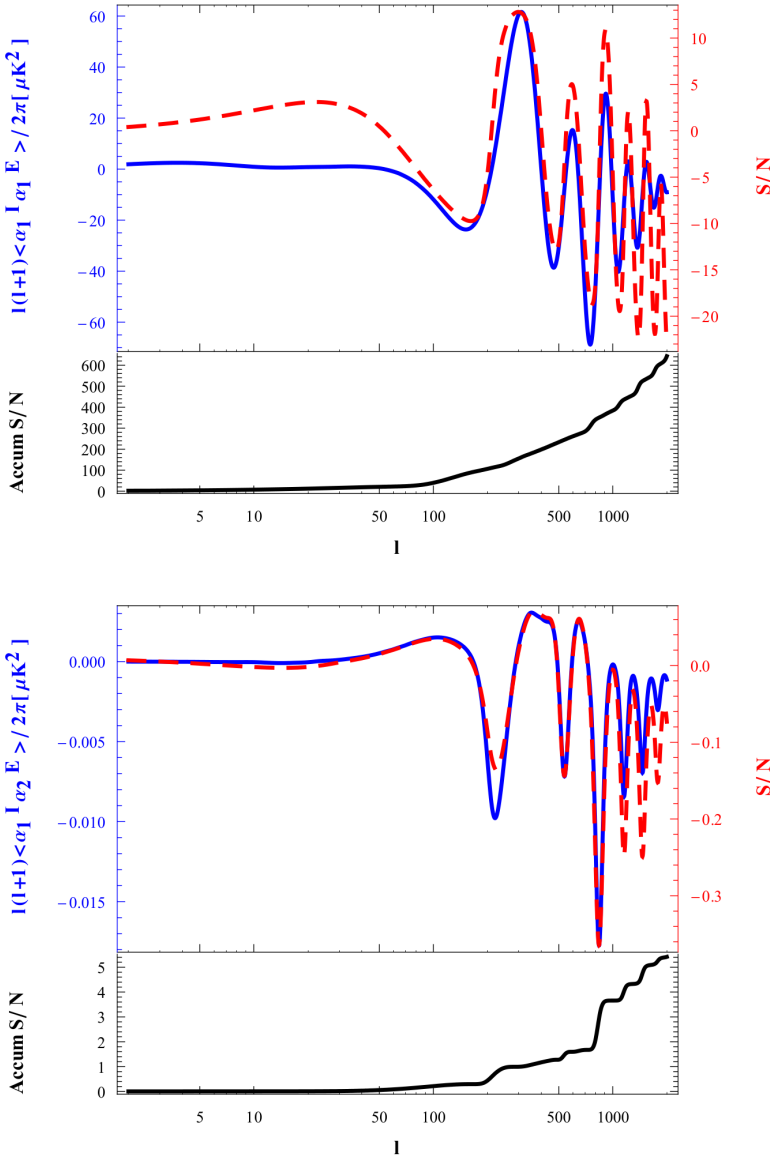


**Figure 4.19:** Same as 4.17 but for the temperature-polarization cross-spectra $\langle \alpha^I_{1lm} \alpha^E_{1lm'} \rangle$ and $\langle \alpha^I_{1lm} \alpha^E_{2lm'} \rangle$.

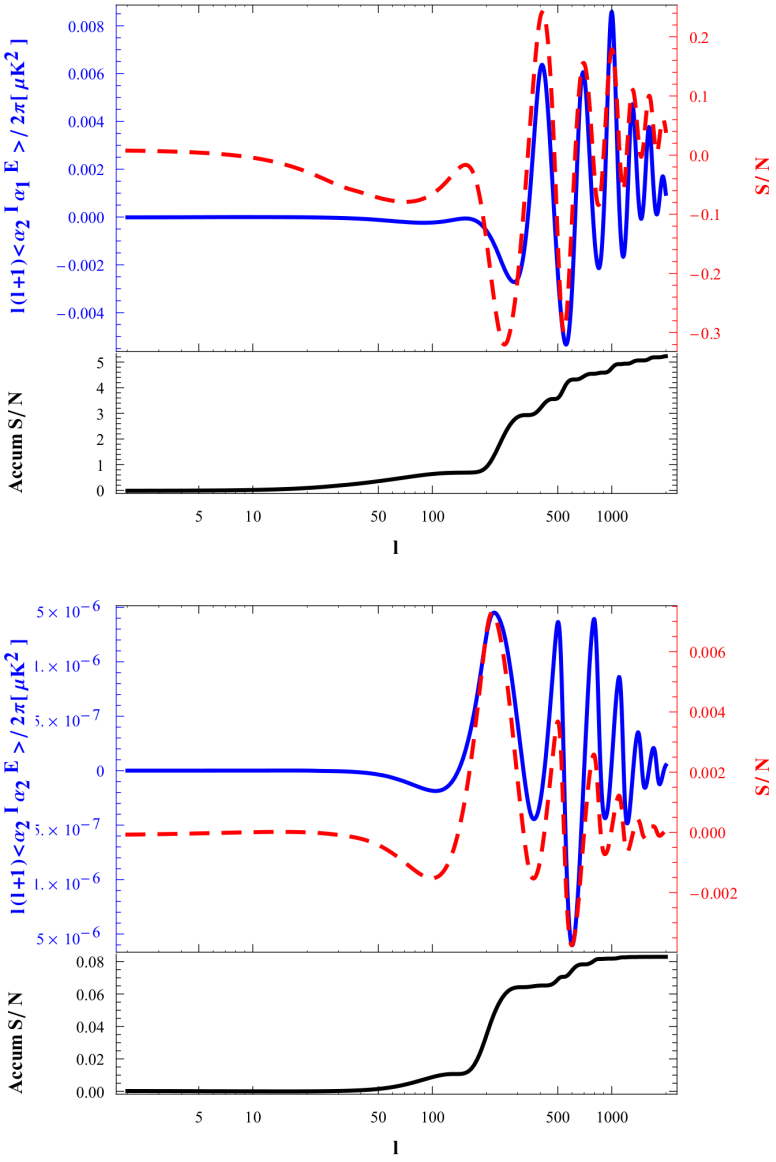


**Figure 4.20:** Same as 4.17 but for the temperature-polarization cross-spectra $\langle \alpha^I_{2lm} \alpha^E_{1lm'} \rangle$ and $\langle \alpha^I_{2lm} \alpha^E_{2lm'} \rangle$.

| | parameter values Planck+WP | Primary CV Limited | Primary+Rayleigh CV Limited |
|---|---|---|---|
| $\Omega_b h^2$ | 0.02205 | 0.25657 | 0.10136 |
| $\Omega_c h^2$ | 0.1199 | 0.3570 | 0.1149 |
| $\tau$ | 0.089 | 2.4033 | 1.0887 |
| $n_s$ | 0.9603 | 0.2623 | 0.0950 |
| $A_s$ | $2.1955 \times 10^{-9}$ | 0.4009 | 0.1829 |
| $H$ | 67.3 | 0.2667 | 0.0870 |
| $Y_p$ | 0.24770 | 1.4288 | 0.3375 |

**Table 4.2:** The percentage constraints on cosmological parameters ($100\sigma_{p_i}/p_i$) for a hypothetical cosmic-variance limited case with and without accounting for the Rayleigh signal. Note that although the Rayleigh signal is detectable with the PRISM-like experiment, this signal doesn't add much constraining power for cosmological parameters as its accumulative signal-to-noise ratio is modest. The constraints on parameters with the PRISM-like experiment are nearly identical to the third (Primary CV limited) column in this table.

We also calculate how much of a constraint one can except for the PRISM-like experiment. In this case, although the Rayleigh signal is detectable, the Rayleigh signal adds very little constraining power for cosmological parameters as its accumulative signal-to-noise ratio is small.

It's also reasonable to ask how biased each cosmological parameter will be by ignoring the Rayleigh scattering. These biases will move the central measured values of each parameter relative to their actual values. The observed power spectrum is a sum of the primary power spectrum, Rayleigh power spectrum and generalized noise (including foregrounds)

$$\tilde{\mathbf{C}}_l = \mathbf{C}_l^{\text{Primary}} + \mathbf{C}_l^{\text{Rayleigh}} + \tilde{\mathbf{N}}_l. \tag{4.72}$$

To calculate the bias, we need to find the difference between expectation value of the parameter estimator, $\langle \hat{p}_i \rangle$, and the true value $\overline{p}_i$, using

$$\mathbf{b}_i = \langle \hat{p}_i \rangle - \overline{p}_i = \mathbf{F}_{ij}^{(00)-1} \mathbf{B}_j, \tag{4.73}$$

where $\mathbf{F}_{ij}^{(00)-1}$ and $\mathbf{B}_j$ are Fisher matrix and bias vector respectively for the power spectrum $\mathbf{C}_l^P = \mathbf{C}_l^{\rm Primary} + \tilde{\mathbf{N}}_l$

$$\mathbf{F}_{ij}^{(00)-1} = \sum_l^{l_{\rm max}} (2l+1)\frac{1}{2} Tr[\mathbf{C}_l^{P-1}\frac{\partial \mathbf{C}_l^P}{\partial p_i}\mathbf{C}_l^{P-1}\frac{\partial \mathbf{C}_l^P}{\partial p_j}], \tag{4.74}$$

$$\mathbf{B}_j = \sum_l^{l_{\rm max}} (2l+1)\frac{1}{2} Tr[\mathbf{C}_l^{P-1}\frac{\partial \mathbf{C}_l^P}{\partial p_j}\mathbf{C}_l^{P-1}\mathbf{C}_l^{\rm Rayleigh}]. \tag{4.75}$$

The biases (relative to standard deviation) introduced by ignoring the Rayleigh scattering for the PRISM-like experiment are

$$b_i/\sigma_i = \{-0.13, 0.08, -0.06, -0.20, -0.02, -0.18, -0.28\} \tag{4.76}$$

for the set of parameters $\{\Omega_b, \Omega_c, \tau, n_s, A_s, H, Y_p\}$. While these potential biases are worrisome and Rayleigh scattering should be incorporated into future analysis, they are still smaller than the forecasted constraints on each parameter.

The potential constraints that could be achieved using a cosmic-variance limited experiment, motivate us to consider how larger signal-to-noise measurements might be made.

### 4.7.3 Improvements to signal to noise ratio

There are a few ways to improve the signal-to-noise ratio of the Rayleigh signal and bring it closer to the idealized cosmic-variance limit. One is to have a more effective foreground removal method. The scheme we discussed assumes an isotropic power spectrum for each foreground component and aims to detect the signal in the presence of foregrounds using only this knowledge. Since Rayleigh scattering is more important at frequencies higher than 300GHz and at high frequencies the dominant foregrounds are Galactic dust and CIB, one might do a better job at foreground removal by measuring Galactic dust and CIB maps at very high frequency, (for example higher than 600GHz), and then extrapolating their spectrum and removing them at the map level from lower frequencies such as 300GHz or 400 GHz. While we will still be left with some residual foreground power spectra they should have a smaller amplitude than the original foreground

power spectra. Furthermore, as long as the Rayleigh signal in not limited by cosmic variance, instead of probing the whole sky one could concentrate observing time on regions of the sky where foreground contamination is less.

Another way to enhance the signal-to-noise ratio is to improve the experiment. To do so, we can either reduce the detector noise by having more detectors (better sensitivity) or by including more frequency channels so that we can model foregrounds with higher fidelity and remove them more effectively.

To examine how sensitive the signal-to-noise ratio of the Rayleigh signal is to each of these improvements, we study three cases: **Case I**. In the first case, we keep the specification of the experiment the same as our PRISM-like experiment but imagine a more effective foreground removal method. More specifically, in this case, by measuring the foregrounds at very high frequencies or optimizing observation to low foreground region, we assume we can remove most of the foreground contamination from lower frequencies and are left with only 5% of the original foreground spectra as residuals. **Case II**. In the second case we use the same normal foreground levels but improve the specification of the experiment. For illustrating purposes we consider an extremely ambitious experiment with 50 frequency channels between 30 GHz and 800 GHz and a noise in each frequency channel of 0.01 nK. **Case III**. The third case is the combination of I and II.

In Figures 4.21 to 4.24, we show the accumulative signal-to-noise ratios for the all eight non-zero elements of CMB covariance matrix for these improved cases. The blue, red, green and black lines are the signal-to-noise ratios respectively for a PRISM-like experiment, Case I, Case II and Case III. For example, the accumulative signal-to-noise ratio for the cross spectra between the primary temperature signal and Rayleigh E-polarization signal which was around 5 for the PRISM-like experiment, is amplified to 26 by improving the foregrounds removal method (Case I), to 71 by decreasing the detector noise (Case II) and to 218 by combining Case I and II (Case III). As can be seen from this graph, in Case III the accumulative signal-to-noise ratio of all the power spectra are greater than 100 and could provide us with valuable information about cosmological parameters.

The effects of improving the signal-to-noise ratio on cosmological parameters are illustrated in Figures 4.25 and 4.26. In Figure 4.25 we plotted the $1\sigma$ and $2\sigma$ constraints on cosmological parameters using only the primary signal. Since

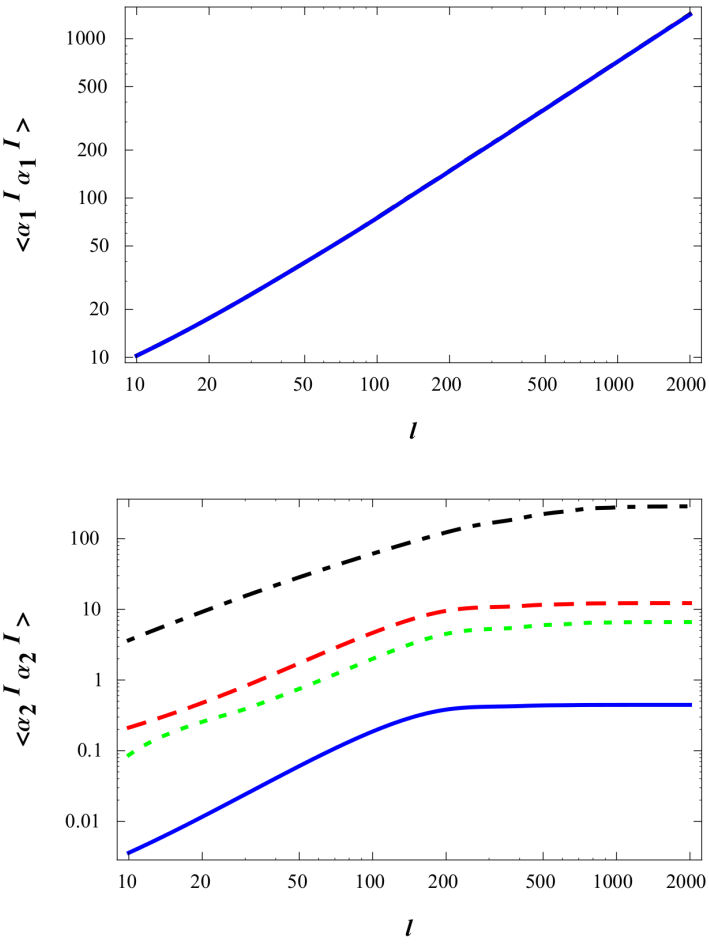


**Figure 4.21:** Accumulative signal-to-noise ratios for the first eigenvalues of intensity $\langle \alpha^I_{1lm} \alpha^I_{1lm'} \rangle$ and polarization $\langle \alpha^E_{1lm} \alpha^E_{1lm'} \rangle$ spectra. The blue (solid), red (dashed), green (dotted) and black (dot dashed) lines are the signal-to-noise ratios respectively for a PRISM-like experiment, for Case I: improved foregrounds removal method, for Case II : improved detector noise, and for Case III which combines Case I and II.

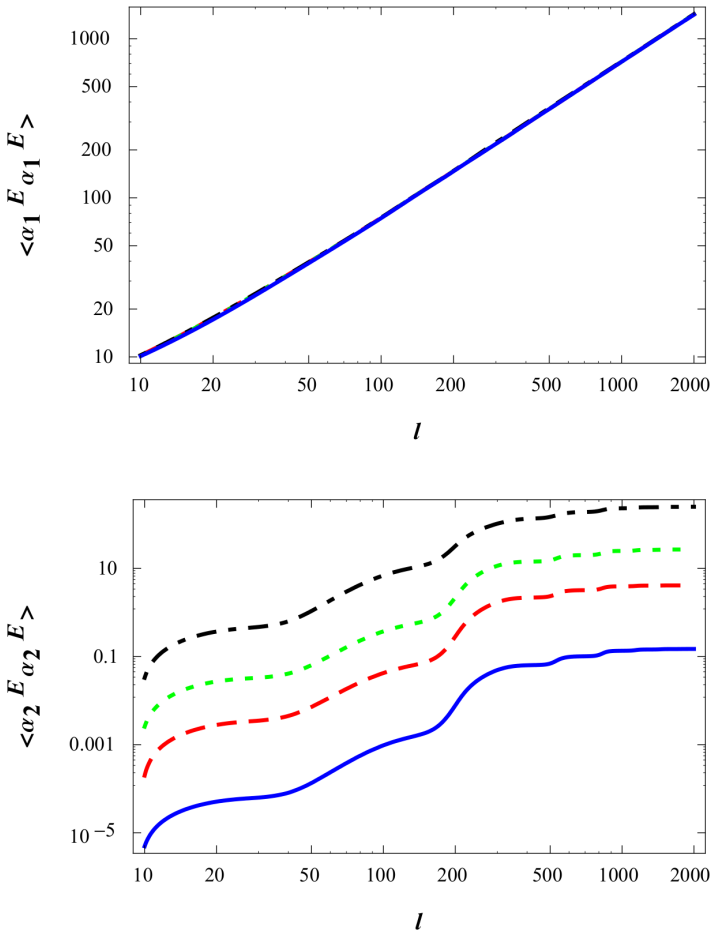


**Figure 4.22:** Same as 4.21 but for the second eigenvalues of intensity $\langle \alpha^I_{2lm} \alpha^I_{2lm'} \rangle$ and polarization $\langle \alpha^E_{2lm} \alpha^E_{2lm'} \rangle$ spectra.

the signal-to-noise ratio for the primary signal is cosmic-variance limited in all the cases considered here, the constraints on the parameters remain the same for all cases. We also show the bias introduced by ignoring the Rayleigh signal in this Figure. In almost all the cases (save for one) the bias for each parameter is less than one sigma and only when the foreground contamination is large and the detector noise is small, Case II, we are left with biases larger than two sigma for some parameters.

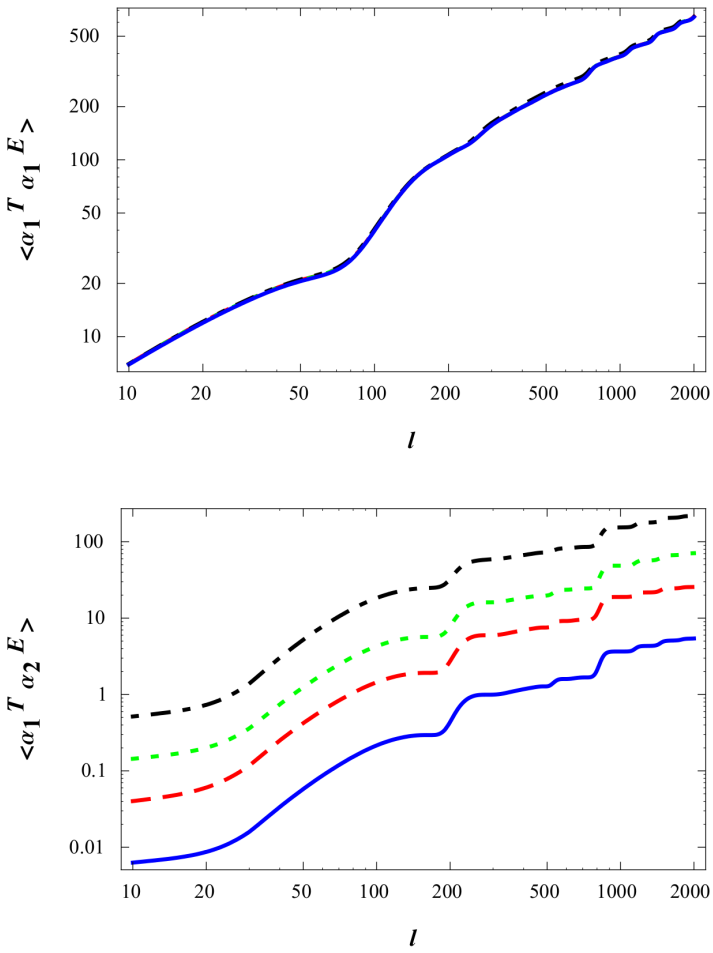


**Figure 4.23:** Same as 4.21 but for the temperature-polarization cross-spectra $\langle \alpha^I_{1lm} \alpha^E_{1lm'} \rangle$ and $\langle \alpha^I_{1lm} \alpha^E_{2lm'} \rangle$.

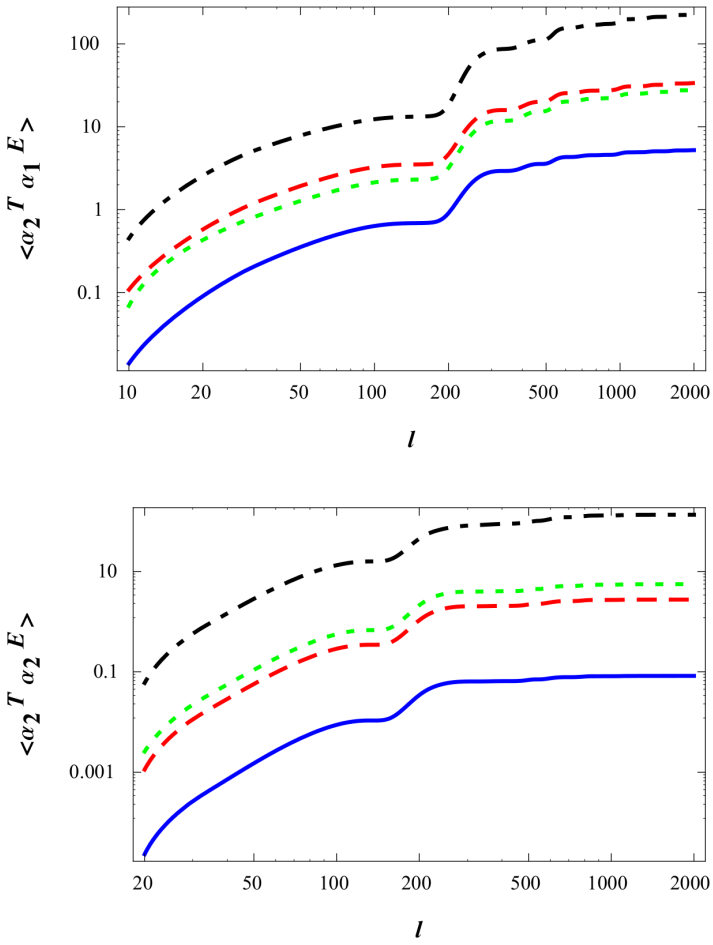


**Figure 4.24:** Same as 4.21 but for the temperature-polarization cross-spectra $\langle \alpha^I_{2lm} \alpha^E_{1lm'} \rangle$ and $\langle \alpha^I_{2lm} \alpha^E_{2lm'} \rangle$.

In Figure 4.26, we plotted the two-sigma constraints on cosmological parameters using both the primary and Rayleigh signal and show that by improving the PRISM-like experiment, as we go through Case I, II and III, the constraints on parameters become smaller since the signal-to-noise ratio of the Rayleigh signal becomes larger. For instance, the percentage error on $Y_p$ in case III is half the constraint of the PRISM-like experiment.

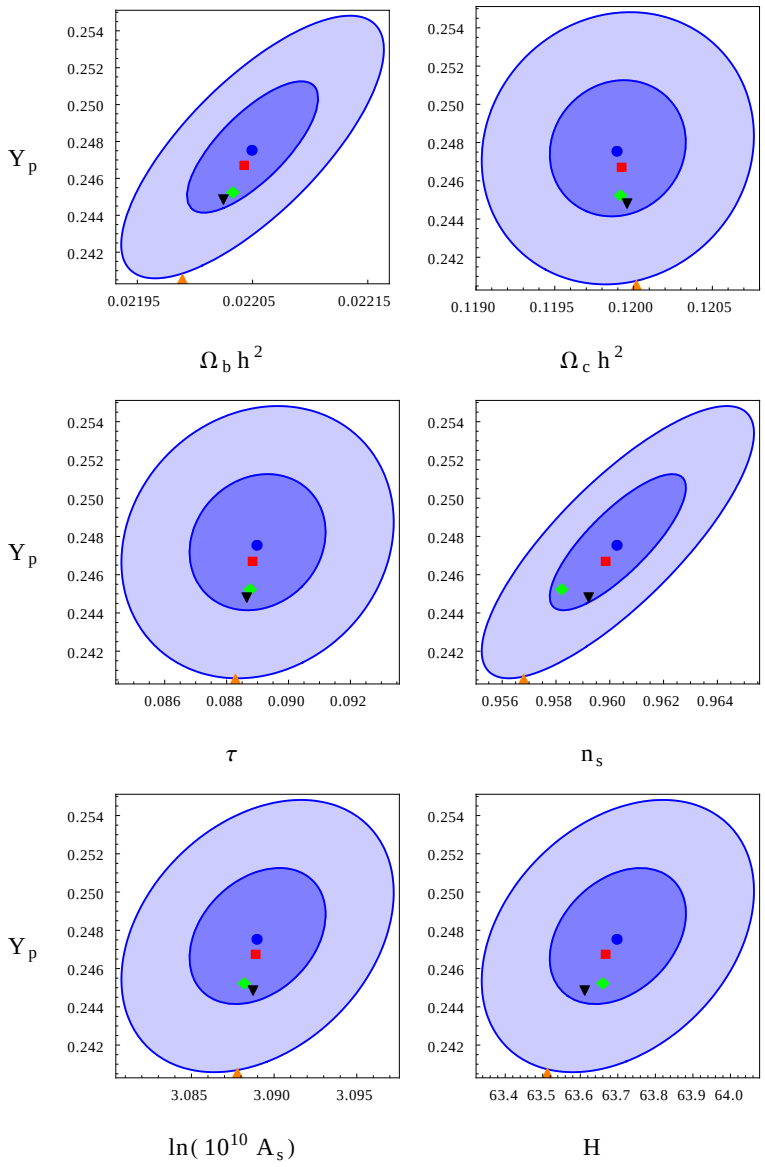


**Figure 4.25:** The biases and constraints on cosmological parameters that could potentially occur if one ignores the Rayleigh signal. The blue contours are the one-sigma and two-sigma constraints on parameters using only the primary signal centred at the fiducial value of the parameters. The red, green, orange and black dots represent the bias introduced by ignoring the Rayleigh signal respectively in PRISM-like experiment, Case I (improving foreground removal), Case II (reducing detector noise) and Case III (combination of both).

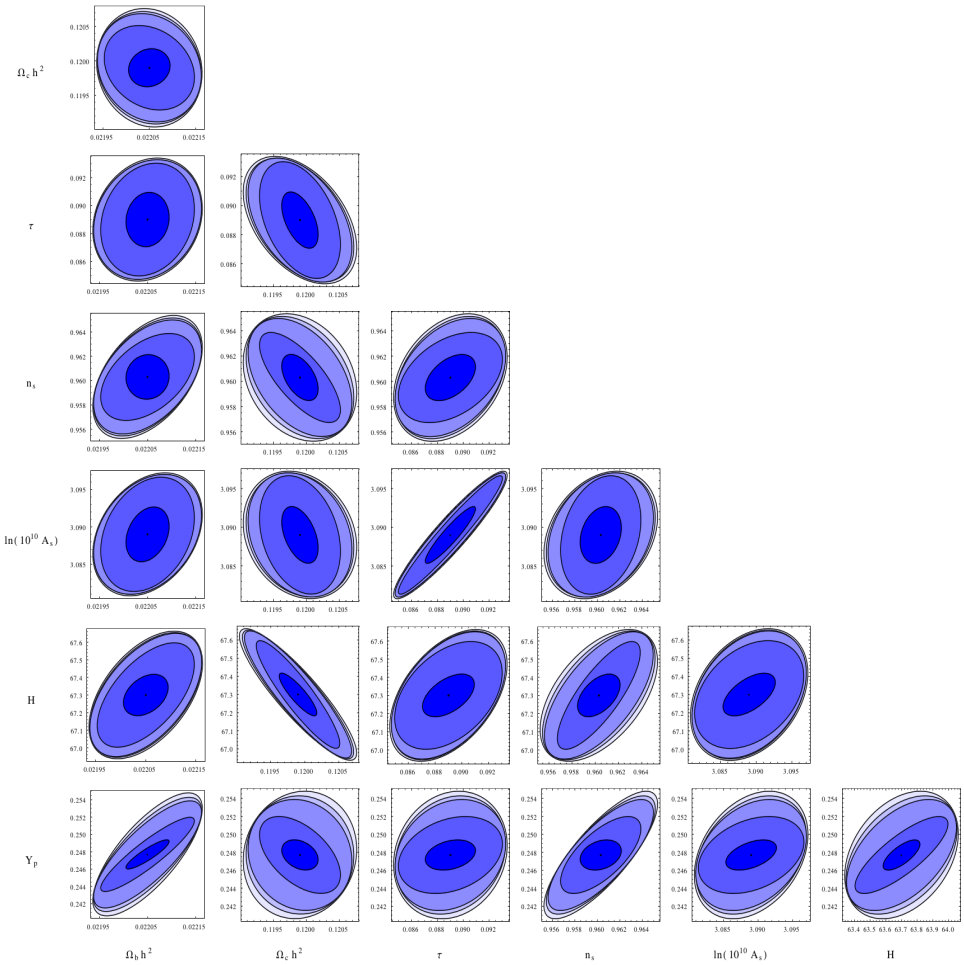


**Figure 4.26:** The two-sigma constraints on cosmological parameters by considering both the primary and Rayleigh signal. The smallest and darkest contour represents the cosmic-variance limited case. The lighter contours show the Case III, Case II, Case I and the PRISM-like experiment respectively as we go from smallest-darkest to largest-lightest contours. Note that the largest contours essentially delineate the conventional (primary only) cosmic variance limit, and smaller contours represent an improvement in parameter constraints beyond this limit.

## 4.8 Conclusions

In this chapter, we have calculated the effect of Rayleigh scattering on CMB temperature and polarization anisotropies as well as the impact on cosmic structure. We also have investigated the possibility of detecting the Rayleigh signal in the CMB. A new method was introduced to account for the frequency-dependence of the Rayleigh cross section by solving for a hierarchy of spectral distortion perturbations, which allows for an accurate treatment of Rayleigh scattering including its back-reaction on baryon perturbations with only a few spectral-distortion hierarchies. We have found that Rayleigh scattering modifies the distribution of matter in the Universe at the 0.3% level.

Since the Rayleigh cross section is frequency-dependent, the CMB temperature and polarization anisotropies depend on frequency too. For each frequency of interest, Rayleigh scattering reduces the $C_l$ power spectrum at high l multipoles because the visibility function shifts to lower redshifts when the Silk damping is more important. For reference, at 857 GHz, the highest frequency of the Planck experiment, both temperature and E-polarization anisotropies decrease as much as 20% near $l \sim 1000$ and at 353 GHz they decrease as much as 0.6%. Low-multipole E-polarization anisotropies increase because the visibility function shifts toward later time when the CMB quadrupole is larger. The increase in E-polarization signal at $l \sim 50$ is 35% at 857 GHz and 0.8% at 353 GHz.

We showed that due to these distortions, the primary intensity and E-polarization power spectra at different frequencies are not perfectly correlated with each other like in standard treatments of the CMB. Furthermore we have found, to a very good approximation, we need two sets of random variables to completely describe the statistics of primordial intensity and E-polarization patterns on the sky we observe. There is a second Rayleigh-distorted CMB sky beyond the primary CMB sky that contains additional information. We have determined a compressed representation of the joint power spectra of these two temperature/intensity and E-polarization skies.

Detecting the Rayleigh signal is very challenging because at high frequencies the number of CMB photons is low and the signal is contaminated by foregrounds. However since both the spectral shape and power spectra of the Rayleigh sky are

different from all the foregrounds, the Rayleigh signal might be detectable if many high frequency channels are included in future CMB missions. We have shown that with a PRISM-like experiment that has many frequency bands, and using a simple power spectrum based foregrounds removal method, the cross spectrum between the primary E-polarization and Rayleigh temperature signal and the cross spectrum between the primary temperature and Rayleigh E-polarization signal should be detectable with accumulative signal-to-noise ratio of 5.2 and 5.4 respectively.

Measuring the Rayleigh signal could provide powerful constraints on cosmological parameters including the helium fraction and scalar spectral index. A more ambitious experiment either observing in low foreground contaminated regions or using a more sophisticated foreground removal method might detect the Rayleigh CMB sky at high signal-to-noise. This would tighten CMB constraints on cosmological parameters beyond what was, even in principle, previously thought possible.

Furthermore, as the Rayleigh opacity is more prominent at high frequencies, one may be able to use this signal to constrain other new physics such as dark matter annihilation into Standard Model particles that inject energy into primordial gas and/or distort the high energy CMB spectrum (e.g., Ref [48]). If these effects alter the Rayleigh signal then detecting it may provide corroborating evidence for such new physics. The detail of such effects and how the Rayleigh signal might constrain them is an interesting topic for future studies.

# Chapter 5

# Cosmic Neutrino Background Anisotropy Spectrum

## 5.1 Introduction

Studying the Cosmic Microwave Background anisotropies provides us with detailed information about the physical content of the Universe [2, 3]. These relic photons have travelled to us from the last scattering surface at redshift $z \simeq 1090$ and thus they can inform us about the condition of the Universe when it was only $\sim 380,000$ years old.

The standard model also predicts a cosmic neutrino background (CNB); relic neutrinos which have free-streamed to us freely from when the Universe was only $\sim$ 1s old. Although the direct detection of the CNB is extraordinary challenging, serious possibilities have been discussed in Ref. [49–52]. One of the recently proposed methods is the process of neutrino capture on a tritium target [52]. In this process, a relic neutrino is captured by a tritium nucleus, and an electron and a $^3$He nucleus are emitted in the final state. This process can be distinguished from tritium $\beta$-decay background by observation of electron kinetic energies emitted from a tritium target that are above the $\beta$-decay endpoint by twice the mass of neutrinos and so is sensitive to the CNB provided the energy resolution is comparable to $m_\nu$. Moreover in Ref. [53] a new method is proposed to use the annual modulation of the CNB by the gravitational focusing of the sun to detect its dipole moment. If

techniques like this prove successful in the future it might be possible to detect CNB anisotropies. With this renewed interest in the detection of relic neutrinos, it is interesting to consider the theory of the CNB, both in the standard model and in theories with non-standard neutrino interactions.

The CNB started to form when neutrinos decoupled from the rest of the cosmic plasma. In the standard model, neutrino decoupling is assumed to happen almost instantaneously at the temperature 1-2 MeV. In this scenario, before decoupling the neutrinos were in contact with the rest of the plasma through weak interactions ($\Gamma \sim G_F^2 T^5$) and they had a Fermi-Dirac equilibrium distribution function. After decoupling, when the rate of the interactions became much smaller than the Hubble rate ($\Gamma \ll H$), the neutrino distribution function maintained its equilibrium shape with the temperature decreasing as the inverse of scale factor $T_\nu \sim \frac{1}{a(t)}$. The temperature of electromagnetic plasma scaled in the same way until it reached the electron mass, $T_\gamma = m_e \approx 0.5$ MeV. When pair annihilation occurred, the photons and baryons were heated up relative to the neutrinos as the latter didn't receive any significant energy from the electron-positron pairs since they were already decoupled and the ratio $\frac{T_\gamma}{T_\nu}$ increased to the well known asymptotic value $\frac{T_\gamma}{T_\nu} \simeq (\frac{11}{4})^{1/3} = 1.401$ [1, 54].

However to calculate the CNB anisotropies properly, a more detailed study of non-instantaneous neutrino decoupling is needed. It is well known that the neutrino plasma receives a small energy contribution from pair annihilation and its final energy density is a bit higher than the instantaneous case. Since neutrinos with higher momentum are heated more, then neutrino spectra have a momentum dependent distortion. There have been a number of papers considering the effect of non-instantaneous decoupling on the background energy density of neutrinos and photons [55–57]. For example, in the most recent paper [56], the final ratio of photon temperature to neutrino temperature is found to be $\frac{T_\gamma}{T_\nu} = 1.399$.

The goal of this chapter is to study the impact of the non-instantaneous decoupling on the evolution of cosmological perturbations and specifically to calculate the CNB anisotropy power spectrum. Some existing works have already derived the massless [58] and massive [59] CNB power spectrum at only large scales assuming neutrino decoupling takes place instantaneously. The main source of anisotropies for the large scale modes is the Integrated Sachs-Wolf (ISW) effect

which is caused by the gravitational redshift occurring between the last scattering surface and the Earth. For massive neutrinos, the ISW effect is momentum dependent and larger than for massless neutrinos as they don't move at the speed of light and are eventually nonrelativistic. Also the distance from the last scattering surface to us is smaller for massive neutrinos [60]. Using a modified version of CAMB [24], we rederive the low $l$ part of the spectrum and show that for massless neutrinos our result is similar to Ref. [58] but we find a different result than Ref. [59] for massive neutrinos. We believe there are two main reasons for this difference. First, for massive neutrinos the power spectrum is momentum dependent and the method used in this work to average over all momenta to present the total power spectrum, is different than the method used in Ref.[59]. Second, in this work we include the effect of the variation of the distance from the last scattering surface for massive neutrinos, which it appears was not included in Ref.[59]. We discuss this further in section 5.6.

In addition to the low $l$ part of the power spectrum, we write a numerical code to solve the Boltzmann equations and calculate the small scale part for both massless and massive neutrinos with allowing neutrinos to oscillate. At small scales, similar to the CMB power spectrum, acoustic oscillations and silk damping are visible in the CNB power spectrum. The smaller momentum-dependent distance from the last scattering surface for the massive neutrinos leads to a shift in the power spectrum toward lower l values and makes the spectrum depend on the momentum of neutrinos.

A recent study [61] showed that the CMB data is compatible with a neutrino self-interaction strength that is orders of magnitude larger than the standard Fermi constant which can delay the neutrino free-streaming to a much later time. We show how the presence of such strong self-interactions modifies the CNB power spectrum.

This chapter is organized as follows: In Section 5.2 the set of the equations evolving the neutrino anisotropies are presented. In Section 5.3, we derive the CNB anisotropy power spectrum for massless neutrinos. The CNB anisotropy power spectrum for massive neutrinos and a discussion on neutrino oscillation are given in Sections 5.4 and 5.5 respectively. Section 5.6 presents a method for averaging over momenta to get the total CNB power spectrum, Section 5.7 investigates the effect

of nonstandard strong self-interactions on the CNB power spectrum and Section 5.8 concludes.

## 5.2 Evolution equations for neutrino anisotropies

As discussed above, since neutrino decoupling is non-instantaneous, neutrinos with higher momentum will receive more energy during pair annihilation and therefore the neutrino distribution function has a non-thermal distortion. Tracking this non-thermal distribution function makes the calculation rather complicated.[1] Therefore in the first approximation, we assume that the distribution function of neutrinos are still the thermal Fermi-Dirac distribution function:

$$f(\vec{x},p,\hat{p},t)=[e^{\frac{p}{T(t)[1+\theta(\vec{x},\hat{p},t)]}}+1]^{-1}, \tag{5.1}$$

where $\vec{x}$ is the position, $\vec{p}$ is the momentum, T is the temperature and $\theta$ is the temperature perturbation. We assume a Universe filled with neutrinos, photons, electrons, positrons and dark matter. At the time of neutrino decoupling the photons, electrons and positrons were tightly coupled. Thus we can treat them as one single perfect fluid with the energy density of $\rho_{\gamma e}=\frac{\pi^2}{15}T_\gamma^4(1+\frac{7}{4}\chi_\rho)$ and pressure of $P_{\gamma e}=\frac{\pi^2}{45}T_\gamma^4(1+\frac{7}{4}\chi_p)$ [62]. $\chi_\rho$ and $\chi_p$ are functions of temperature and electron mass, they are equal to one when the temperature is much higher than the electron mass and electrons and positrons are relativistic and they vanish as the temperature drops down and pair annihilation happens. Using the Einstein and Boltzmann equations given in chapter 2, one can solve for the evolution of perturbations.

In this chapter the Newtonian Conformal gauge is used since variables in this gauge are directly related to the physical quantities. The line element in this particular gauge is:

$$ds^2=a^2(\tau)[-(1+2\psi)d\tau^2+(1-2\phi)dx^i dx_i], \tag{5.2}$$

where $\phi$ and $\psi$ are the gravitational potentials, $\tau$ is the conformal time and $a(\tau)$ is the scale factor. The phase-space neutrino distribution evolves according to

[1] For an example of how to proceed in such an energy dependent case see Chapter 4.

the Boltzmann equation.

$$\frac{df}{dt} = C[f(\vec{p})]. \tag{5.3}$$

The left-hand side of the Boltzmann equation is the full time derivative of the distribution function and the right-hand side contains all possible collision terms. The first order part of $df/dt$ in Newtonian Conformal gauge can be written as

$$\begin{aligned} \frac{df}{dt} &= -p\frac{\partial f^0}{\partial p}[\frac{\partial \theta}{\partial t} + \frac{ik\mu}{a}\theta - \frac{\partial \phi}{\partial t} + \frac{ik\mu}{a}\psi] \\ &\quad -p(\theta - \psi)\frac{\partial (C_0/p)}{\partial p}, \end{aligned} \tag{5.4}$$

where $k$ is the wavenumber of the perturbations, $\mu = \hat{p}\cdot\hat{k}$ and $C_0$ is the zero order collision term.

The right hand side or the collision term can be written as

$$\begin{aligned} C[f(\vec{p})] &= \frac{1}{2E(p)}\int d\Pi_q d\Pi_{q'} d\Pi_{p'} \sum_{\text{spin}} |M|^2 (2\pi)^4 \\ &\times \delta^4(p+q-p'-q')\{f(\vec{q'})f(\vec{p'})[1-f(\vec{q})][1-f(\vec{p})] \\ &- f(\vec{q})f(\vec{p})[1-f(\vec{q'})][1-f(\vec{p'})]\}. \end{aligned} \tag{5.5}$$

In this equation, $d\Pi_q = \frac{d^3q}{(2\pi)^3 2E(q)}$ is the Lorentz-invariant phase-space volume element, $\delta^4(p+q-p'-q')$ enforces the energy-momentum conservation and M is the process amplitude. Calculating these integrals is extremely complicated especially when we include the Pauli blocking terms. For simplicity, we assume that all the particles involved in these interactions are massless and use Maxwell-Boltzmann statistics for all particles during neutrino decoupling. With these assumptions we can ignore the Pauli blocking terms while maintaining detailed balance. Note that we only use Maxwell-Boltzmann statistics to obtain the collision terms which are functions of only temperature. For the rest of the calculations we use the Fermi-Dirac distribution function for the neutrino plasma.

Around the time of neutrino decoupling, the weak reactions that keep neutrinos in contact with the rest of plasma are scattering and annihilation processes with electrons and positrons which heat up neutrinos, and also scattering and annihilation processes involving only neutrinos which thermalize the neutrino distributions.

| processes | $\sum \lvert M \rvert^2$ |
|---|---|
| $\nu_e + \bar{\nu}_e \to e^- + e^+$ | $8G_F^2(b_w t^2 + a_w u^2)$ |
| $\nu_e + \bar{\nu}_e \to \nu_i + \bar{\nu}_i$ | $8G_F^2 u^2$ |
| $\nu_e + e^- \to \nu_e + e^-$ | $8G_F^2(a_w s^2 + b_w u^2)$ |
| $\nu_e + e^+ \to \nu_e + e^+$ | $8G_F^2(b_w s^2 + a_w u^2)$ |
| $\nu_e + \nu_e \to \nu_e + \nu_e$ | $8G_F^2 s^2$ |
| $\nu_e + \bar{\nu}_e \to \nu_e + \bar{\nu}_e$ | $8G_F^2(4u^2)$ |
| $\nu_e + \nu_i \to \nu_e + \nu_i$ | $8G_F^2 s^2$ |
| $\nu_e + \bar{\nu}_i \to \nu_e + \bar{\nu}_i$ | $8G_F^2 u^2$ |

**Table 5.1:** The weak interactions involving electron neutrinos and their corresponding squared amplitudes.

| processes | $\sum \lvert M \rvert^2$ |
|---|---|
| $\nu_i + \bar{\nu}_i \to e^- + e^+$ | $8G_F^2(b_w t^2 + c_w u^2)$ |
| $\nu_i + \bar{\nu}_i \to \nu_e + \bar{\nu}_e$ | $8G_F^2 u^2$ |
| $\nu_i + \bar{\nu}_i \to \nu_j + \bar{\nu}_j$ | $8G_F^2 u^2$ |
| $\nu_i + e^- \to \nu_i + e^-$ | $8G_F^2(c_w s^2 + b_w u^2)$ |
| $\nu_i + e^+ \to \nu_i + e^+$ | $8G_F^2(b_w s^2 + c_w u^2)$ |
| $\nu_i + \nu_e \to \nu_i + \nu_e$ | $8G_F^2 s^2$ |
| $\nu_i + \bar{\nu}_e \to \nu_i + \bar{\nu}_e$ | $8G_F^2 u^2$ |
| $\nu_i + \nu_i \to \nu_i + \nu_i$ | $8G_F^2 s^2$ |
| $\nu_i + \nu_j \to \nu_i + \nu_j$ | $8G_F^2 s^2$ |
| $\nu_i + \bar{\nu}_i \to \nu_i + \bar{\nu}_i$ | $8G_F^2(4u^2)$ |
| $\nu_i + \bar{\nu}_j \to \nu_i + \bar{\nu}_j$ | $8G_F^2 u^2$ |

**Table 5.2:** The weak interactions involving $\mu$ and $\tau$ neutrinos and their corresponding squared amplitudes.

All the relevant weak interactions and corresponding squared amplitudes involving electron neutrinos and muon or tau neutrinos are displayed in Table 5.1 and 5.2 respectively [55].

The interactions involving $\mu$ and $\tau$-neutrino are identical but different from interactions involving electron neutrinos since electron neutrinos have both charged and neutral current interactions. In our notation, $G_F$ is the Fermi constant, $p$ is the four-momentum of the incoming neutrino, $q$ the four-momentum of the other

incoming particle, $p'$ the four-momentum of the outgoing neutrino or lepton and $q'$ is the four-momentum of the other outgoing particle. $s = (p+q)^2$ is the square of the center of mass energy, $u = (p-q')^2$ and $t = (p-p')^2$ are the squares of the four-momentum transfer. Also $a_w = (2\sin^2\theta_w + 1)^2 \simeq 2.13$, $b_w = (2\sin^2\theta_w)^2 \simeq 0.212$ and $c_w = (2\sin^2\theta_w - 1)^2 \simeq 0.292$ where $\theta_w$ is the Weinberg angle.

We can rewrite the first order Boltzmann equation governing the neutrinos anisotropies as

$$\begin{aligned}&\frac{p}{T}[-p\frac{\partial f^0}{\partial p}(\frac{\partial \theta}{\partial \tau} + ik\mu\theta - \frac{\partial \phi}{\partial \tau} + ik\mu\psi) - p(\theta-\psi)\frac{\partial(C_0)}{p}] \\ &= 4G_F^2 T_\nu^5 a[p\frac{\partial f^0}{\partial p}\theta(\hat{p})A(p) + B(p) + C(p) + D(p)]. \end{aligned} \tag{5.6}$$

Similar to Ref. [55], we categorize the terms arising from the expansion of $[f(\vec{q'})f(\vec{p'}) - f(\vec{q})f(\vec{p})]$ into four different types of terms in equation 5.6. The "A terms" represent the disappearing of a neutrino of momentum p and arise from all the processes, e.g., $\nu(p) + e^- \to \nu + e^-$. "B terms" come from all the processes that just change the momentum of neutrinos from $p$ to $p'$, e.g., $\nu(p) + e^- \to \nu(p') + e^-$ and involve an integration over $\theta_\nu(p')$. "C terms" are similar to B terms except they arise from interactions of electron neutrinos with $\mu$ or $\tau$ neutrinos and vice versa, e.g., $\nu_e(p) + \bar{\nu}_e \to \nu_\mu(p') + \bar{\nu}_\mu$. And finally "D terms" arise from interactions of neutrinos with electrons or positrons which heat up the neutrinos and they involve an integration over $\theta_e$. These terms for electron neutrinos are:

$$A_e(p) = \frac{1}{T_\nu^6}\int d\Lambda[f_{e0}(q)(a_w+b_w)(u^2+s^2) \tag{5.7}$$
$$+f_{\nu 0}(q)(b_w t^2+(8+a_w)u^2+3s^2)],$$
$$B_e(p) = \frac{1}{T_\nu^6}\int d\Lambda[f_{\nu 0}(p)q\frac{\partial f_{\nu 0}}{\partial q}\theta_{\nu_e}(\hat{q})[s^2+b_w t^2+(a_w+6)u^2] \tag{5.8}$$
$$-p'\frac{\partial f_{\nu 0}}{\partial p'}\theta_{\nu_e}(\hat{p'})[(a_w+b_w)(s^2+u^2)f_{e0}(p')+(6u^2+3s^2)f_{\nu 0}(p')]$$
$$-f_{\nu 0}(p')q'\frac{\partial f_{\nu 0}}{\partial q'}\theta_{\nu_e}(\hat{q'})[s^2+4u^2]],$$
$$C_e(p) = \frac{1}{T_\nu^6}\int d\Lambda[f_{\nu 0}(p)q\frac{\partial f_{\nu 0}}{\partial q}\theta_{\nu_\mu}(\hat{q})[2s^2+2u^2] \tag{5.9}$$
$$-f_{\nu 0}(q')p'\frac{\partial f_{\nu 0}}{\partial p'}\theta_{\nu_\mu}(\hat{p'})[2u^2]-f_{\nu 0}(p')q'\frac{\partial f_{\nu 0}}{\partial q'}\theta_{\nu_\mu}(\hat{q'})[2s^2+4u^2]],$$
$$D_e(p) = \frac{1}{T_\nu^6}\int d\Lambda[f_{\nu 0}(p)q\frac{\partial f_{e0}}{\partial q}\theta_e(\hat{q})[(a_w+b_w)s^2+(a_w+b_w)u^2] \tag{5.10}$$
$$-f_{e0}(q')p'\frac{\partial f_{e0}}{\partial p'}\theta_e(\hat{p'})[b_w t^2+a_w u^2]$$
$$-q'\frac{\partial f_{e0}}{\partial q'}\theta_e(\hat{q'})[(a_w+b_w)(u^2+s^2)f_{\nu 0}(p')+(b_w t^2+a_w u^2)f_{e0}(p')]],$$

where $d\Lambda = d\Pi_q d\Pi_{q'} d\Pi_{p'}(2\pi)^4\delta^4(p+q-p'-q')$ is a nine-dimensional phase-space volume element.

The $\mu-$ and $\tau-$neutrino phase-space distribution functions are identical and for them these four terms are:

$$A_\mu(p) = \frac{1}{T_\nu^6}\int d\Lambda[f_{e0}(q)(c_w+b_w)(u^2+s^2) \tag{5.11}$$
$$+f_{\nu 0}(q)(b_w t^2+(8+c_w)u^2+3s^2)],$$
$$B_\mu(p) = \frac{1}{T_\nu^6}\int d\Lambda[f_{\nu 0}(p)q\frac{\partial f_{\nu 0}}{\partial q}\theta_{\nu_\mu}(\hat{q})[2s^2+b_w t^2+(c_w+7)u^2] \tag{5.12}$$
$$-p'\frac{\partial f_{\nu 0}}{\partial p'}\theta_{\nu_\mu}(\hat{p'})[(c_w+b_w)(s^2+u^2)f_{e0}(p')+(7u^2+3s^2)f_{\nu 0}(p')]$$
$$-f_{\nu 0}(p')q'\frac{\partial f_{\nu 0}}{\partial q'}\theta_{\nu_\mu}(\hat{q'})[2s^2+6u^2]],$$
$$C_\mu(p) = \frac{1}{T_\nu^6}\int d\Lambda[f_{\nu 0}(p)q\frac{\partial f_{\nu 0}}{\partial q}\theta_{\nu_e}(\hat{q})[s^2+u^2] \tag{5.13}$$
$$-f_{\nu 0}(q')p'\frac{\partial f_{\nu 0}}{\partial p'}\theta_{\nu_e}(\hat{p'})[u^2]-f_{\nu 0}(p')q'\frac{\partial f_{\nu 0}}{\partial q'}\theta_{\nu_e}(\hat{q'})[s^2+2u^2]],$$
$$D_\mu(p) = \frac{1}{T_\nu^6}\int d\Lambda[f_{\nu 0}(p)q\frac{\partial f_{e0}}{\partial q}\theta_e(\hat{q})[(c_w+b_w)s^2+(c_w+b_w)u^2] \tag{5.14}$$
$$-f_{e0}(q')p'\frac{\partial f_{e0}}{\partial p'}\theta_e(\hat{p'})[b_w t^2+c_w u^2]$$
$$-q'\frac{\partial f_{e0}}{\partial q'}\theta_e(\hat{q'})[(c_w+b_w)(u^2+s^2)f_{\nu 0}(p')+(b_w t^2+c_w u^2)f_{e0}(p')]].$$

Evaluation of these terms $A_i$, $B_i$, $C_i$ and $D_i$ are rather tedious and the details of how to calculate them are presented in the Appendix A.

By Integrating the Boltzmann equation over $p^2dp$ and dividing it by $\int p^3 dp f_0(p)$, we can write the evolution equation for temperature perturbations:

$$\frac{\partial\theta_\nu}{\partial\tau}+ik\mu\theta_\nu-\frac{\partial\phi}{\partial\tau}+ik\mu\psi+(\theta_\nu-\psi/4)\frac{Q_\nu}{\rho_\nu}=4G_F^2T_\nu^5 a$$
$$\times[-\hat{A}\theta_\nu+\frac{1}{24}\int_0^\infty(B(z,\mu)+C(z,\mu)+D(z,\mu))z^2dz] \tag{5.15}$$

where $\hat{A}=5\frac{A}{(p/T_\nu)^2}$ is just a number and $Q_\nu\equiv\int d^3pppC_0(p)$ is the zero order energy transfer. Expanding the angular dependence of perturbations in a series of Legendre polynomials $\theta_\nu=\sum(-i)^l(2l+1)\theta_{\nu l}P_l(\mu)$, one can find an evolution equation for each $\theta_{\nu l}$ by multiplying the Boltzmann equation by $\frac{1}{(-i)^l}\int_{-1}^{1}\frac{d\mu}{2}P_l(\mu)$ and inte-

grating:

$$\dot{\theta}_{\nu_e l} + k\frac{l+1}{2l+1}\theta_{\nu_e l+1} - \frac{kl}{2l+1}\theta_{\nu_e l-1} - \dot{\phi}\,\delta_{l,0} - \frac{k}{3}\psi\delta_{l,1} + \theta_{\nu_e l}\frac{Q_{\nu_e}}{\rho_{\nu_e}} - \delta_{l,0}\frac{\psi}{4}\frac{Q_{\nu_e}}{\rho_{\nu_e}}$$
$$= 4G_F^2 T_\nu^5 a[-\hat{A_e}\theta_{\nu_e l} - \frac{1}{\pi^3}[\delta_{l,0}\frac{4}{3}((a_w+b_w+9)\theta_{\nu_e 0} + 8\theta_{\nu_\mu 0} + 4(a_w+b_w)r^{-4}\theta_{e0})$$
$$-\delta_{l,1}\frac{2}{3}((a_w+b_w+9)\theta_{\nu_e 1} + 8\theta_{\nu_\mu 1} + 4(a_w+b_w)r^{-4}\theta_{e1})$$
$$+\delta_{l,2}\frac{2}{15}((a_w+b_w+9)\theta_{\nu_e 2} + 8\theta_{\nu_\mu 2} + 4(a_w+b_w)r^{-4}\theta_{e2})]$$
$$+\frac{1}{384\pi^3}[\theta_{\nu_e l}c_{\nu_e}(l,r) + \theta_{\nu_\mu l}c_{\nu_\mu}(l,r) + \theta_{el}c_e(l,r)]], \tag{5.16}$$

$$\dot{\theta}_{\nu_\mu l} + k\frac{l+1}{2l+1}\theta_{\nu_\mu l+1} - \frac{kl}{2l+1}\theta_{\nu_\mu l-1} - \dot{\phi}\,\delta_{l,0} - \frac{k}{3}\psi\delta_{l,1} + \theta_{\nu_\mu l}\frac{Q_{\nu_\mu}}{\rho_{\nu_\mu}} - \delta_{l,0}\frac{\psi}{4}\frac{Q_{\nu_\mu}}{\rho_{\nu_\mu}}$$
$$= 4G_F^2 T_\nu^5 a[-\hat{A_\mu}\theta_{\nu_\mu l} - \frac{1}{\pi^3}[\delta_{l,0}\frac{4}{3}((c_w+b_w+13)\theta_{\nu_\mu 0} + 4\theta_{\nu_e 0} + 4(c_w+b_w)r^{-4}\theta_{e0})$$
$$-\delta_{l,1}\frac{2}{3}((c_w+b_w+13)\theta_{\nu_\mu 1} + 4\theta_{\nu_e 1} + 4(c_w+b_w)r^{-4}\theta_{e1})$$
$$+\delta_{l,2}\frac{2}{15}((c_w+b_w+13)\theta_{\nu_\mu 2} + 4\theta_{\nu_e 2} + 4(c_w+b_w)r^{-4}\theta_{e2})]$$
$$+\frac{1}{384\pi^3}[\theta_{\nu_\mu l}d_{\nu_\mu}(l,r) + \theta_{\nu_e l}d_{\nu_e}(l,r) + \theta_{el}d_e(l,r)]], \tag{5.17}$$

where $r = \frac{T_\nu}{T_\gamma}$ is the ratio of neutrino temperature to photon temperature and $c_{\nu_e}$, $c_{\nu_\mu}$, $c_e$, $d_{\nu_e}$, $d_{\nu_\mu}$,$d_e$ are functions of both $l$ and $r$ and they are defined in the Appendix.

The neutrino energy over-density $\delta_\nu$, velocity $\theta_\nu$ and anisotropic stress $\sigma_\nu$ are related to the first three moments of temperature perturbation: $\theta_{\nu 0} = \frac{\delta_\nu}{4}$, $\theta_{\nu 1} = \frac{1}{3k}\theta_\nu$ and $\theta_{\nu 2} = \frac{\sigma_\nu}{2}$ [22]. Since the photon-electron-positron plasma is a perfect fluid, we only need two variables to describe it: $\theta_{e0} = \frac{\rho_{\gamma e}}{T_\gamma d\rho_{\gamma e}/dT_\gamma}\delta_{\gamma e}$ and $\theta_{e1} = \frac{1}{3k}\theta_{\gamma e}$. The evolution equations for $\delta_{\gamma e}$ and $\theta_{\gamma e}$ is found using energy conservation. These equations are similar to the ones for neutrinos except that the momentum-energy conservation implies that the collision term for the $l = 0$ moment must be multiplied by $\frac{\rho_\nu}{\rho_{\gamma e}}$ and for $l = 1$ must be multiplied by $\frac{\rho_\nu + P_\nu}{\rho_{\gamma e} + P_{\gamma e}}$ where $\rho_\alpha$ and $P_\alpha$ are the energy density and pressure density of $\alpha$-fluid respectively .

Also note that the background energy-momentum conservation implies that

$Q_\nu = Q_{\nu_e} + 2Q_{\nu_\mu} = -Q_{\gamma e}$ [63]. To close this set of equations and solve them, one need to include the zero order energy conservation equations for each fluid:

$$\dot{\rho}_\alpha = -3H(\rho_\alpha + P_\alpha) + Q_\alpha. \tag{5.18}$$

We solve this set of equations by writing a numerical code and utilizing the LSODA solver from ODEPACK [64] library which implements a variety of solvers for ordinary differential equations. The LSODA solver is based on the backward differentiation formula method and automatically switches between nonstiff and stiff solvers depending on the behaviour of the problem.

It's interesting to first calculate the final value of ratio of neutrino temperature to photon temperature $\frac{T_\nu}{T_\gamma}$ to see how much it differs from the well known value $(\frac{4}{11})^{1/3} = 0.7138$, i.e. how much neutrino energy density has increased due to heating caused by the pair annihilation. We plot the ratio of neutrino temperature to photon temperature as a function of conformal time in Figure 5.1. At early times the neutrino temperature and photon temperature are the same, and as electron-positron annihilation happens, the photons receive most of the energy and the ratio of neutrino temperature to photon temperature decreases to the final asymptotic value of $\frac{T_\nu}{T_\gamma} = 0.7161$ which is a bit higher than $(\frac{4}{11})^{1/3}$ since neutrinos share some of the heat as well.

One can also express this increase in terms of an excess in the effective numbers of neutrinos, $N_{\rm eff}$, which is defined as

$$\rho_\nu = \frac{7}{8}(\frac{4}{11})^{4/3} N_{\rm eff} \rho_\gamma. \tag{5.19}$$

Therefore the effective number of neutrinos when we include the increase in neutrino energy due to pair annihilation is $N_{\rm eff} = 3.0399$ which is consistent with the result of Ref. [56].

## 5.3 Neutrino power spectrum

To calculate the neutrino anisotropy power spectrum, we use the line of sight integration approach [42]. In this approach, the temperature anisotropy can be written as an integral over the product of a source term and a geometrical term.

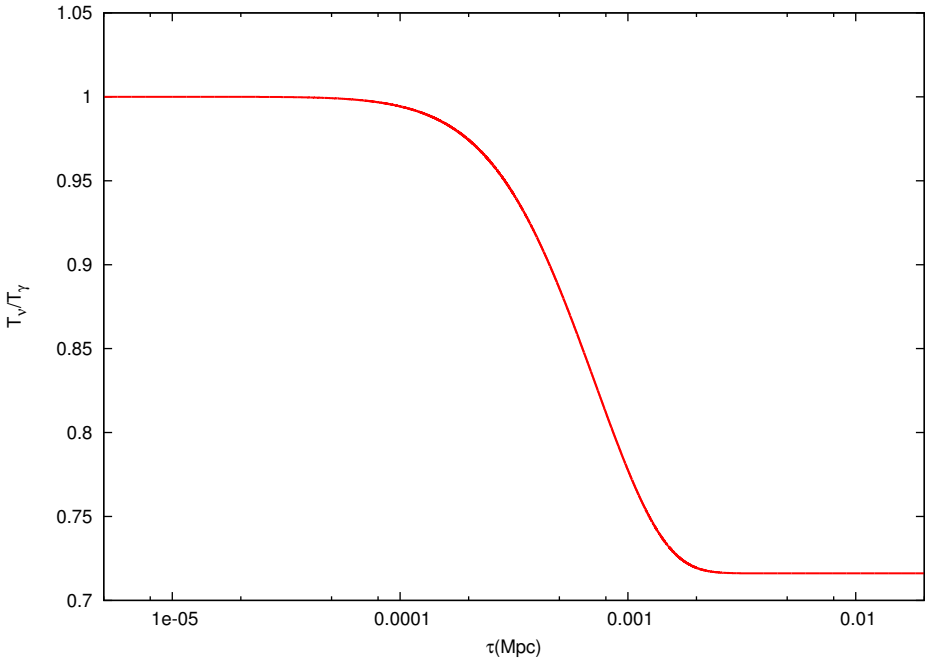


**Figure 5.1:** Ratio of neutrino temperature to photon temperature as a function of conformal time. The final asymptotic value of this ratio is 0.7161 which is a bit higher that the value in instantaneous neutrino decoupling scenario ($(\frac{4}{11})^{1/3}$) and shows that neutrinos receive some energy from the pair annihilation.

Defining the opacity as $\dot{\kappa} = -4G_F^2 T_\nu^5 a$, we write the solution of Equation 5.15 as

$$\theta_{\nu_e}(k,\mu,\tau_0) = \int_0^{\tau_0} d\tau \tilde{S}_e(k,\mu,\tau) e^{ik\mu(\tau-\tau_0)-\kappa}, \tag{5.20}$$

where the source term is

$$\begin{aligned} \tilde{S}_e &= \dot{\phi} - ik\mu\psi - (\frac{Q_{\nu_e}}{\rho_{\nu_e}} + \dot{\kappa}(1-\hat{A}_e)) \\ &\times \sum_{l=0}^{\infty}(-i)^l(2l+1)p_l(\mu)\theta_{\nu_e l} + \frac{\psi}{4}\frac{Q_{\nu_e}}{\rho_{\nu_e}} \\ &-\dot{\kappa}\frac{30}{7\pi^4}\int_0^{\infty}(B_e(z,\mu)+C_e(z,\mu)+D_e(z,\mu))z^2 dz]. \end{aligned} \tag{5.21}$$

We can eliminate the angle $\mu$ in the integrand by integrating by parts, and then drop the boundary terms since at $\tau \to 0$ it vanishes, and at $\tau = \tau_0$ it doesn't have any angular dependence. Therefore we can replace $\mu$ with $\frac{1}{ik}\frac{d}{d\tau}$ everywhere in the integrand. Then by multiplying the equation by $\frac{1}{(-i)^l}\int_{-1}^{1}\frac{d\mu}{2}P_l(\mu)$ and taking the integral, we get the following evolution equation for each moment of the neutrino temperature perturbation.

$$\theta_{\nu_e l}(k,\tau_0) = \int_0^{\tau_0} d\tau S_e(k,\tau) j_l[k(\tau_0-\tau)]. \tag{5.22}$$

The line of sight integration method helps us to have fewer coupled differential equations since the geometrical term is just the Bessel function and the source term, which depends on cosmological perturbations, can be calculated using a small number of differential equations.

We can even simplify the source term further and move the time derivatives to the Bessel functions by integrating by parts and then use the recurrence relations of the Bessel functions. After simplification, the source function for the electron

neutrino is

$$
\begin{aligned}
S_e(k,\tau,l) &= e^{-\kappa}(\dot{\phi}+\dot{\psi}) \qquad (5.23)\\
&+ g(\tau)[\psi-\frac{\psi}{4}\frac{Q_{\nu_e}}{\rho_{\nu_e}\dot{\kappa}}-\frac{1}{\pi^3}[(9+a_w+b_w)(\frac{4}{3}\theta_{\nu_e 0}+\frac{1}{2}\theta_{\nu_e 2})\\
&+ 8(\frac{4}{3}\theta_{\nu_\mu 0}+\frac{1}{2}\theta_{\nu_\mu 2})+4(a_w+b_w)r^{-4}(\frac{4}{3}\theta_{e0}+\frac{1}{2}\theta_{e2})]\\
&+ 2\frac{1}{\pi^3}[(9+a_w+b_w)\theta_{\nu_e 1}+8\theta_{\nu_\mu 1}+4(a_w+b_w)r^{-4}\theta_{e1}](-\frac{l+1}{x}+1)\\
&- \frac{3}{2}\frac{1}{\pi^3}[(9+a_w+b_w)\theta_{\nu_e 2}+8\theta_{\nu_\mu 2}](\frac{(l+1)(l+2)}{x^2}-\frac{2}{x}-1)\\
&+ (\frac{Q_{\nu_e}}{\rho_{\nu_e}\dot{\kappa}}+1-\hat{A}_e)[\theta_{\nu_e 0}+3\theta_{\nu_e 1}(-\frac{l+1}{x}+1)\\
&- 5\theta_{\nu_e 2}(-\frac{3}{2}\frac{(l+1)(l+2)}{x^2}+\frac{3}{x}+1)\\
&+ 7\theta_{\nu_e 3}(-\frac{5}{2}\frac{(l+1)(l+2)(l+3)}{x^3}+\frac{5}{2}\frac{l^2+l+6}{x^2}+\frac{l+6}{x}-1)+...]\\
&+ \frac{1}{384\pi^3}[f(0,r)+3f(1,r)(-\frac{l+1}{x}+1)\\
&- 5f(2,r)(-\frac{3}{2}\frac{(l+1)(l+2)}{x^2}+\frac{3}{x}+1)\\
&+ 7f(3,r)(-\frac{5}{2}\frac{(l+1)(l+2)(l+3)}{x^3}+\frac{5}{2}\frac{l^2+l+6}{x^2}+\frac{l+6}{x}-1)+...]].
\end{aligned}
$$

In this equation, $g(\tau)=-\dot{\kappa}e^{-\kappa}$ is the visibility function, the probability density function for the time at which neutrinos decoupled from the rest of the plasma and

$$f(l,r)=\theta_{\nu_e l}C_{\nu_e}(l)+\theta_{\nu_\mu l}C_{\nu_\mu}(l)+\theta_{el}C_e(l). \qquad (5.24)$$

There are two terms in the source function, one is proportional to the derivatives of gravitational potentials and the other is proportional to the visibility function. The visibility function is a very sharp function and it is only nonzero during a very brief period around decoupling ($\Delta\tau/\tau_0 \simeq 10^{-7}$). The behaviour of this visibility function is shown in Figure 5.2. After this short period, the only nonzero term in the source function is the term proportional to $\dot{\phi}$ and $\dot{\psi}$ which is called the Integrated Sachs-Wolfe term.

Note that since the Universe is radiation-dominated at the time of neutrino

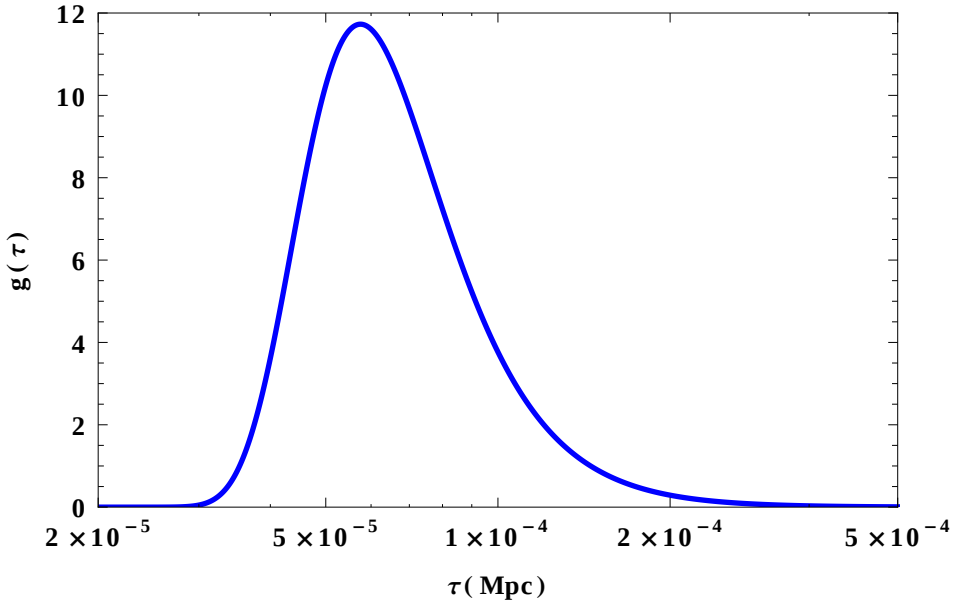


**Figure 5.2:** The visibility function as a function of conformal time. The peak of the visibility function occurs at $\tau = 5.75 \times 10^{-5}$Mpc or $T \simeq 1.48$ MeV

.

decoupling, the gravitational potentials for the modes that enter the horizon at this time evolve more dramatically compared to the modes that enter the horizon at the time of photon decoupling. Therefore we expect the ISW term to play a larger role for the neutrino power spectrum than for the CMB power spectrum.

As discussed earlier, the visibility function is sharply peaked during decoupling and since during this time $\tau/\tau_0$ is smaller than $10^{-7}$, the spherical Bessel function $j_l[k(\tau_0-\tau)]$ is a very smooth function compare to the visibility function. Therefore

$$\begin{aligned} \theta_{\nu_e l}(k,\tau_0) &= j_l[k(\tau_0)]\int_0^{\tau_0} d\tau S_e(k,\tau,l) \\ &= j_l[k(\tau_0)]\hat{S}_e(k,l), \end{aligned} \tag{5.25}$$

where the $\hat{S}_e(k,l)$ is just the time integral over the source function.

The anisotropy spectrum can be obtained by integrating over the initial power

spectrum of the metric perturbation:

$$C_l = 4\pi \int_0^\infty k^2 dk P_\psi(k) |\theta_l(k, \tau = \tau_0)|^2 \quad (5.26)$$

$$= 4\pi A \int_0^\infty \frac{dk}{k} \hat{S}_e^2(k,l) j_l^2[k\tau_0]. \quad (5.27)$$

In this equation $P_\psi(k) = Ak^{n_s-4}$ is the primordial potential fluctuation power spectrum. For the power law index, we assumed a flat Harrison-Zeldovich spectrum $n_s = 1$. We anticipate the peaks of the power spectrum to appear at very small scales ($l > 10^8$). In Ref. [65] it's shown that for high Bessel index l, the integral in Eq. 5.27 is equivalent to

$$C_l = \frac{\pi A}{(l+1/2)^2} \int_0^\infty \frac{\hat{S}_e^2[\frac{l+1/2}{\tau_0}\sqrt{1+y}, l]}{\sqrt{y(1+y)^3}} dy \quad (5.28)$$

Similarly the same calculation can be done for $\mu$ and $\tau$ neutrinos:

$$\theta_{\nu_\mu l}(k, \tau_0) = \int_0^{\tau_0} d\tau S_\mu(k, \tau, l) j_l[k(\tau_0 - \tau)], \quad (5.29)$$

where

$$
\begin{aligned}
S_\mu(k,\tau,l) &= e^{-\kappa}(\dot{\phi}+\dot{\psi}) \qquad (5.30)\\
&+ g(\tau)[\psi - \frac{\psi}{4}\frac{Q_{\nu_e}}{\rho_{\nu_e}\dot{\kappa}} - \frac{1}{\pi^3}[(13+c_w+b_w)(\frac{4}{3}\theta_{\nu_\mu 0}+\frac{1}{2}\theta_{\nu_\mu 2})\\
&+ 4(\frac{4}{3}\theta_{\nu_e 0}+\frac{1}{2}\theta_{\nu_e 2})+4(c_w+b_w)r^{-4}(\frac{4}{3}\theta_{e0}+\frac{1}{2}\theta_{e2})]\\
&+ 2\frac{1}{\pi^3}[(13+c_w+b_w)\theta_{\nu_\mu 1}+4\theta_{\nu_e 1}+4(c_w+b_w)r^{-4}\theta_{e1}](-\frac{l+1}{x}+1)\\
&- \frac{3}{2}\frac{1}{\pi^3}[(13+c_w+b_w)\theta_{\nu_\mu 2}+4\theta_{\nu_e 2}](\frac{(l+1)(l+2)}{x^2}-\frac{2}{x}-1)\\
&+ (\frac{Q_{\nu_\mu}}{\rho_{\nu_\mu}\dot{\kappa}}+1-\hat{A}_\mu)[\theta_{\nu_\mu 0}+3\theta_{\nu_\mu 1}(-\frac{l+1}{x}+1)\\
&- 5\theta_{\nu_\mu 2}(-\frac{3}{2}\frac{(l+1)(l+2)}{x^2}+\frac{3}{x}+1)\\
&+ 7\theta_{\nu_\mu 3}(-\frac{5}{2}\frac{(l+1)(l+2)(l+3)}{x^3}+\frac{5}{2}\frac{l^2+l+6}{x^2}+\frac{l+6}{x}-1)+...]\\
&+ \frac{1}{384\pi^3}[f_\mu(0,r)+3f_\mu(1,r)(-\frac{l+1}{x}+1)\\
&- 5f_\mu(2,r)(-\frac{3}{2}\frac{(l+1)(l+2)}{x^2}+\frac{3}{x}+1)\\
&+ 7f_\mu(3,r)(-\frac{5}{2}\frac{(l+1)(l+2)(l+3)}{x^3}+\frac{5}{2}\frac{l^2+l+6}{x^2}+\frac{l+6}{x}-1)+...]],
\end{aligned}
$$

We numerically calculate the anisotropy spectrum for electron and $\mu$ or $\tau$ neutrinos. The result is shown in Figure 5.3.

Similar to the CMB power spectrum, the acoustic oscillations and Silk damping are visible in neutrino anisotropy spectrum. The acoustic oscillations arise from the competition between gravitational collapse and neutrino pressure which tends to erase the anisotropies. This competition leads to this pattern of peaks and troughs in the power spectrum.

The Silk damping is caused by the finite thickness of the last scattering, since neutrinos move a mean distance during the decoupling, any perturbation on scales smaller than this distance will be washed out, which results in damping of higher k modes, ie higher l values.

In contrast to the CMB power spectrum, in the CNB spectrum the height of the

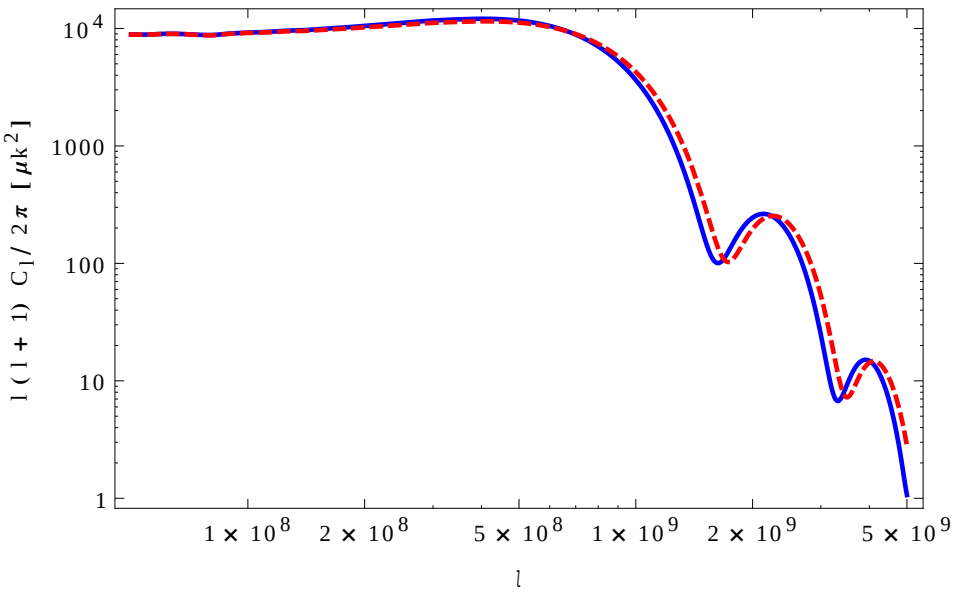


**Figure 5.3:** The anisotropy power spectrum for massless electron (blue) and $\mu$ or $\tau$ (red) neutrinos. Similar to the CMB power spectrum, the acoustic oscillations and Silk damping are visible in this plot.

peaks do not alternate because there is no non-relativistic particle during neutrino decoupling to resemble baryons during photon last scattering.

The peaks show the characteristic structure of coherent oscillations and appear at roughly $l_p = n\pi\frac{\tau_0}{r_s}$ where $r_s = \int_0^\tau d\tau c_s$ is the sound horizon at the time of decoupling.

Another feature worth noticing is that $3000 \lesssim l \lesssim 3 \times 10^8$ values correspond to the modes that were outside the horizon at the time of decoupling but entered the horizon in the radiation-dominated era. For these modes the ISW term is the dominant term which leads to an almost flat power spectrum.

## 5.4 Anisotropy spectrum for massive neutrinos

In the last section, we assumed that neutrinos were massless. Yet, based on cosmological constraints and measured neutrino mass differences from neutrino oscillation experiments, only one of the three species of neutrinos is potentially

relativistic and the other two must have masses greater than $10^{-2}$ eV [66]. Thus it's important to also find the anisotropy spectrum for massive neutrinos.

We start by writing the evolution equation for temperature perturbations for a massive neutrino:

$$\dot{\theta}_\nu + (ik\frac{q}{\varepsilon}\mu - \dot{\kappa})\theta_\nu = \tilde{S}(k,\tau) + \Delta\tilde{S}(k,\tau,m). \tag{5.31}$$

We follow the notation of Ref. [22] where $\varepsilon = \sqrt{q^2 + m^2a^2}$ and q is the comoving momentum. In the above equation $\tilde{S}$ is the source term for massless neutrinos and $\Delta\tilde{S}$ is the difference in source between massive and massless neutrinos. Since during the neutrino decoupling the temperature of the universe is much greater than any mass allowed for neutrinos, all the three species of CNB neutrinos are relativistic and the only difference between massive and massless neutrinos is in the ISW term:

$$\Delta\tilde{S} = (\dot{\phi} - ik\frac{\varepsilon}{q}\mu\psi) - (\dot{\phi} - ik\mu\psi), \tag{5.32}$$

which is only nonzero for large-scale modes that entered the horizon at the time when the neutrinos are un-relativistic.

Again we use the line of sight integration approach to find $\theta_\nu$:

$$\begin{aligned}\theta_\nu &= \int d\tau\tilde{S}(k,\tau)e^{ik\mu(\int_0^\tau \frac{q}{\varepsilon}d\tau' - \int_0^{\tau_0}\frac{q}{\varepsilon}d\tau')} \\ &\quad + \int d\tau[ik\mu\psi - ik\frac{\varepsilon}{q}\mu\psi]e^{ik\mu(\int_0^\tau \frac{q}{\varepsilon}d\tau' - \int_0^{\tau_0}\frac{q}{\varepsilon}d\tau')}.\end{aligned} \tag{5.33}$$

Note that $\int_0^\tau \frac{q}{\varepsilon}d\tau' = \chi(\tau)$ is the comoving distance travelled by a massive neutrino from big bang to $\tau$ and $\chi_0 = \chi(\tau_0)$. The distance from the last scattering surface to us $(\chi_0 - \chi(\tau_{\rm dec}))$ depends on both the mass of neutrinos and their momentum. In Figure 5.4. this distance is plotted as a function of $m_\nu$ for when the momentum of neutrinos at present is $3T_\nu$. Note that for masses above $10^{-4}$ eV, the last scattering surface is much closer to us.

Following the same steps that we did for the massless neutrinos in Eq. 5.20 to

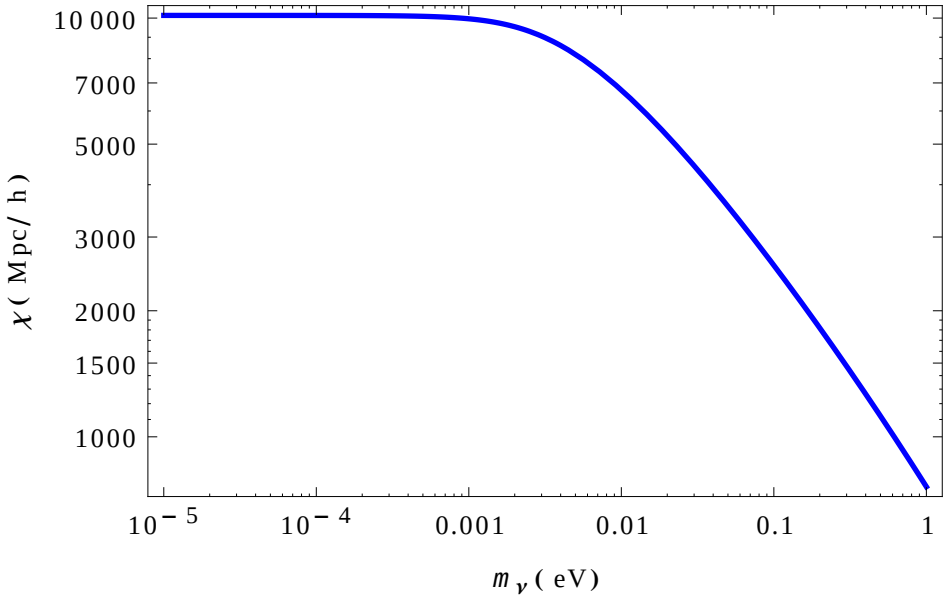


**Figure 5.4:** The comoving distance travelled by a massive neutrino from the last scattering surface to us as a function of $m_\nu$ for one value of the neutrino momentum ($3T_\nu$).

5.25 leads to

$$\begin{aligned}\theta_{\nu l}(k,\tau_0,q) &= \int d\tau (S+\Delta S) j_l[k(\chi_0-\chi(\tau))] \\ &= j_l[k(\chi_0]\int d\tau (S(k,\tau)+\Delta S(k,\tau)),\end{aligned} \tag{5.34}$$

where

$$\begin{aligned}\Delta S(k,\tau) &= \frac{d}{d\tau}(\psi\frac{\varepsilon^2}{q^2})-\dot{\psi} \\ &= \dot{\psi}(\frac{\varepsilon^2}{q^2}-1)+\psi\frac{2m^2a\dot{a}}{q^2}.\end{aligned} \tag{5.35}$$

First note that now $\theta_l$ is momentum-dependent, but we can still calculate the neutrino angular power spectrum as a function of momentum.

For large values of $l$ which correspond to the modes entering the horizon in the

radiation-dominated era, all the neutrinos can be treated as massless and therefore $\Delta S$ for these modes is negligible. Thus, apart from neutrino oscillation, the only difference for massive neutrinos would be that the distance from the last scattering surface for massive neutrinos are smaller than for massless neutrinos which leads to a shift in the angular power spectrum toward lower $l$ values for massive neutrinos.

For $l \lesssim 10^7$ which correspond to the modes that entered the horizon long after neutrino decoupling, the only relevant source is the ISW term. Using a modified version of CAMB [24], the angular power spectrum at low $l$ values is plotted for three different neutrino masses in Figure 5.5 . In this chapter we assume the normal hierarchy and the squared mass difference to be $\Delta m^2_{1,2} = 8 \times 10^{-5}$ eV$^2$ and $\Delta m^2_{2,3} = 2.5 \times 10^{-3}$ eV$^2$. Assuming that the lightest neutrino is massless then $m_1 = 0$ eV, $m_2 = 0.00894$ eV and $m_3 = 0.05894$ eV. For low $l$ values, in addition to a shift toward lower $l$ which is due to the fact that the distance from the last scattering for massive neutrinos is smaller, we observe a boost because of the larger ISW effect for massive neutrinos.

## 5.5 Neutrino oscillation

Neutrinos are produced and detected in flavor eigenstates but they propagate in mass eigenstates. Since the unitary matrix that transforms from the mass basis to the flavor basis is not orthogonal, in calculating the neutrinos anisotropy power spectrum, we must take into account that neutrinos can oscillate.

We are primarily interested in the anisotropy power spectrum for an electron neutrino at the detector. For a neutrino that is travelling in the $m_1$ mass eigenstate, we can define an effective visibility function or equivalently an effective source function:

$$S^{\rm eff}_{m_1}(k,\tau) = |Ue1|^2 S_e(k,\tau) + 2|U_{\mu 1}|^2 S_\mu(k,\tau) \tag{5.36}$$

where $|U_{e1}|^2 = |\langle \nu_e | \nu_1 \rangle|^2$ is the probability that the $m_1$ mass eigenstate has electron flavour and $|U_{\mu 1}|^2 = |\langle \nu_\mu | \nu_1 \rangle|^2$ is the probability that it has muon flavour. Then

$$\theta_l^{{\rm eff},m_1,p}(k,\tau_0) = \int d\tau S^{\rm eff}_{m_1}(k,\tau) j_l[k(\chi_0^{m_1,p} - \chi^{m_1,p}(\tau))] = \hat{S}^{\rm eff}_{m_1}(k) j_l[k\chi_0^{m_1,p}] \tag{5.37}$$

Note that $\chi^{m_1,p}(\tau)$ depends both on the mass of neutrino $m_1$ and momentum $p$

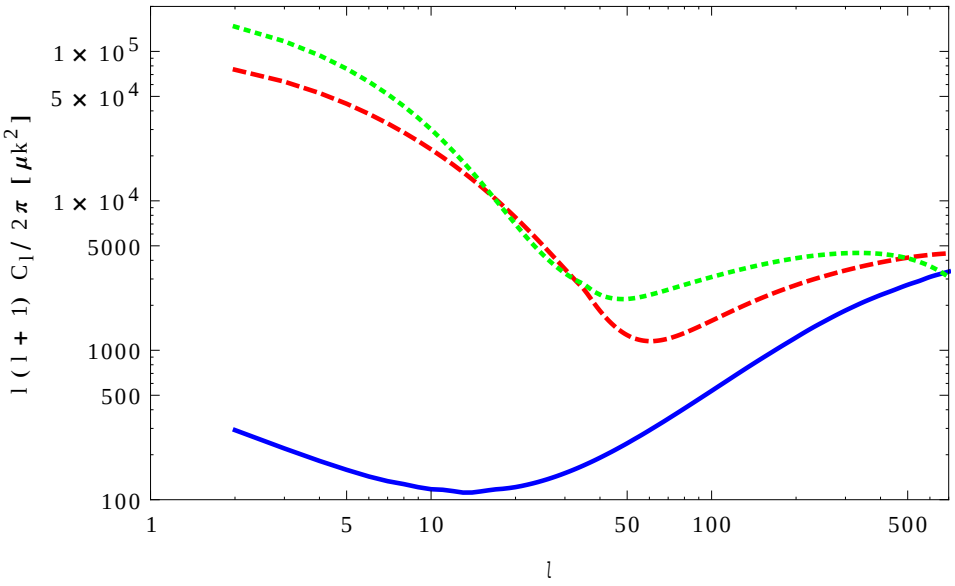


**Figure 5.5:** The anisotropy power spectrum at low $l$ values for three different neutrino masses with momentum $p = 0.0005$ eV: $m_1 = 0$ eV (blue, solid), $m_2 = 0.00894$ eV (red, dashed) and $m_3 = 0.05894$ eV (green, dotted). Since the ISW effect is larger for massive neutrinos, there is a boost at low $l$ angular power spectrum for these neutrinos.

of it at present. Using the a similar procedure as for the massless neutrinos we can derive the equation to calculate the anisotropy power spectrum for a neutrino travelling in one of the mass eigenstates.

$$C_l^{\text{eff},m_i,p} = \frac{\pi A}{(l+1/2)^2} \int_0^\infty \hat{S}_{m_i}^{\text{eff}}[\frac{l+1/2}{\chi_0^{m_i,p}}\sqrt{1+y}]\frac{dy}{\sqrt{y(1+y)^3}} \tag{5.38}$$

The anisotropy power spectrum for the three mass eigenstates are plotted in Figure 5.6. As discussed previously, the distance from the last scattering surface is smaller for massive neutrinos and the angular power spectrum for massive neutrinos are shifted toward lower l values.

Neutrinos propagate in these mass eigenstates until they reach a detector where they are detected in flavour eigenstates. The effective $\theta_l(k, \tau = \tau_0)$ for an electron

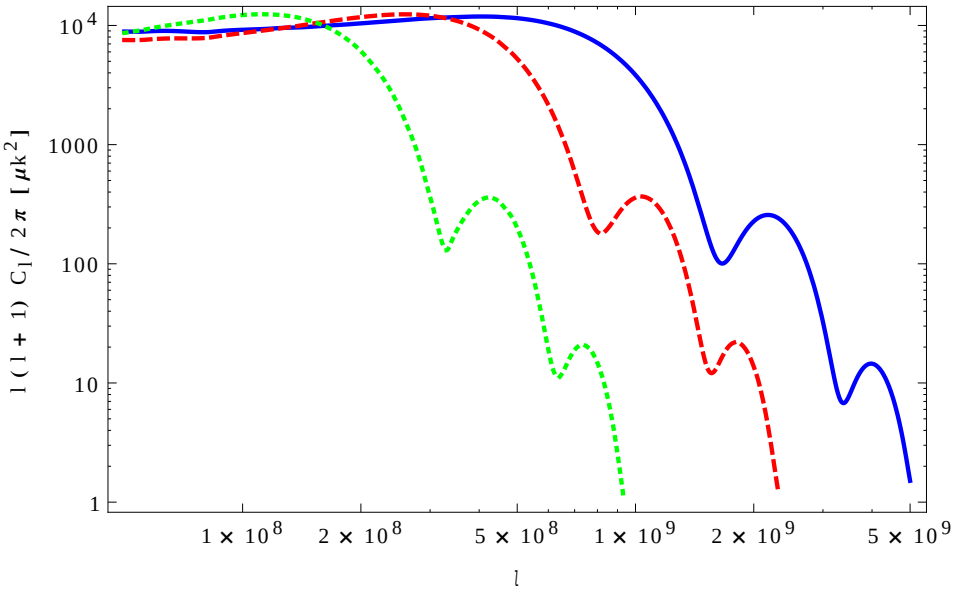


**Figure 5.6:** The anisotropy power spectrum for massive neutrinos with momentum $p = 0.0005$ eV before they are detected. The blue (solid), red (dashed) and green (dotted) curves are the power spectra for $m_1 = 0$ eV, $m_2 = 0.00894$ eV and $m_3 = 0.05894$ eV mass eigenstates respectively.

neutrino at the detector is

$$\theta_l^{\mathrm{eff},e,p}(k,\tau_0) = |U_{e1}|^2\theta_l^{\mathrm{eff},m_1,p_0} + |U_{e2}|^2\theta_l^{\mathrm{eff},m_2,p} + |U_{e2}|^2\theta_l^{\mathrm{eff},m_2,p_0}. \tag{5.39}$$

Then the effective anisotropy power spectrum for an electron neutrino at the detector is

$$\begin{aligned} C_l^{\mathrm{eff},e,pq} &= 4\pi\int dk k^2 P(k)(\theta_l^{\mathrm{eff},e,p}\theta_l^{\mathrm{eff},e,q}) \\ &= \begin{cases} 4\pi\sum_{i=1}^{3}|U_{ei}|^4\int dk k^2 P(k)|\theta_l^{\mathrm{eff},m_i,p}|^2, & \text{if } p=q, \\ 4\pi\sum_{i\neq j}|U_{ei}|^2|U_{ej}|^2\int dk k^2 P(k)(\theta_l^{\mathrm{eff},m_i,p}(k)\theta_l^{\mathrm{eff},m_j,q}(k)), & p\neq q. \end{cases} \end{aligned} \tag{5.40}$$

To get the last line in the above equation, we use the completeness relation of

the spherical Bessel functions [67]:

$$\int dk k^2 F(k) j_l[kr] j_l[kr'] \simeq \frac{\pi}{2r}\delta(r-r')F(\frac{l}{r}), \tag{5.41}$$

where the assumption is that $F(k)$ is a slowly varying function. Therefore :

$$\begin{aligned} &\int dk k^2 P(k)(\theta_l^{\mathrm{eff},m_i,p}(k)\theta_l^{\mathrm{eff},m_j,q}(k)) \\ &= A\int \frac{dk}{k}\hat{S}^{\mathrm{eff}}_{m_i}(k)\hat{S}^{\mathrm{eff}}_{m_j}(k) j_l[k\chi_0^{m_i,p}] j_l[k\chi_0^{m_j,q}] \\ &\propto \delta[\chi_0^{m_i,p} - \chi_0^{m_j,q}]. \end{aligned} \tag{5.42}$$

This condition tells us that the cross spectra between the mass eigenstates are only non-zero when $p$ and $q$ are such that $\chi_0^{m_i,p} = \chi_0^{m_j,q}$, in other words they are only non-zero when the neutrinos with momenta $p$ and $q$ are coming from the same distance.

In Figure 5.7 the anisotropy power spectra for an electron neutrino and a muon neutrino at the detector, $C_l^{\mathrm{eff},e,p}$ and $C_l^{\mathrm{eff},\tau,p}$ are plotted for $p = 0.0005$ eV. Since the most massive mass eigenstate only contributes to $\mu$ or $\tau$ neutrinos, the effective distance from the last scattering surface for these neutrinos is smaller than for electron neutrinos and thus the anisotropy power spectrum for these neutrinos is shifted toward lower l values.

## 5.6 Averaging over momenta

We should emphasize here that the neutrino temperature perturbation is momentum dependent since the the comoving distance travelled by massive neutrinos from decoupling surface to us and the late time ISW effect depend on momentum. The CNB anisotropy spectrum plotted in Fig. 5.6 and 5.5 are the small-scale and large-scale part of the mass eigenstates spectra for a neutrino with momentum $p = 0.0005$ eV. If the momentum of the neutrino is lower then since the distance to the last scattering surface becomes smaller for massive neutrinos, the spectra shift toward even lower $l$ values. Also lower momentum leads to larger late time ISW effect which means the large-scale parts of the spectra enhance even more.

The total temperature perturbation for a neutrino travelling in a mass eigenstate

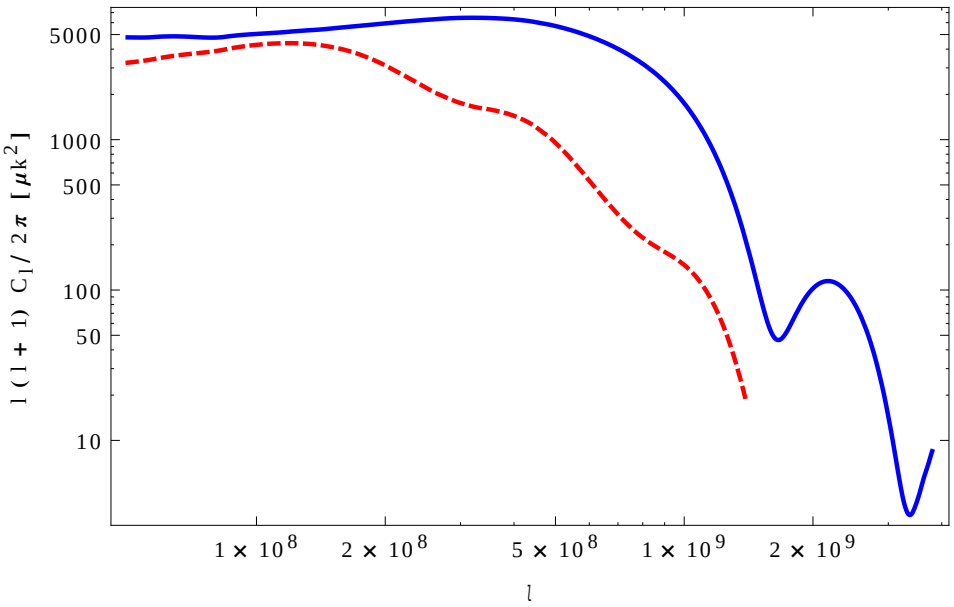


**Figure 5.7:** The anisotropy power spectrum for an electron neutrino (blue, solid) and a muon neutrino (red, dashed) at the detector. The neutrino momentum is $p = 0.0005$ eV

$\theta_l^{\text{eff},m_i}(k)$ then is found by averaging over momenta at the present time:

$$\theta_l^{\text{eff},m_i}(k) = \frac{\int dp p^2 f_0(p) \theta_l^{\text{eff},m_i,p}(k)}{\int dp p^2 f_0(p)}, \tag{5.43}$$

where $f_0(p)$ is the relativistic Fermi-Dirac distribution function. At the time of decoupling, the neutrinos follow the relativistic Fermi-Dirac distribution and since particle number is conserved after decoupling, this distribution hold even when neutrinos become non-relativistic. Then the total angular power spectrum for a neutrino travelling in a mass eigenstate is

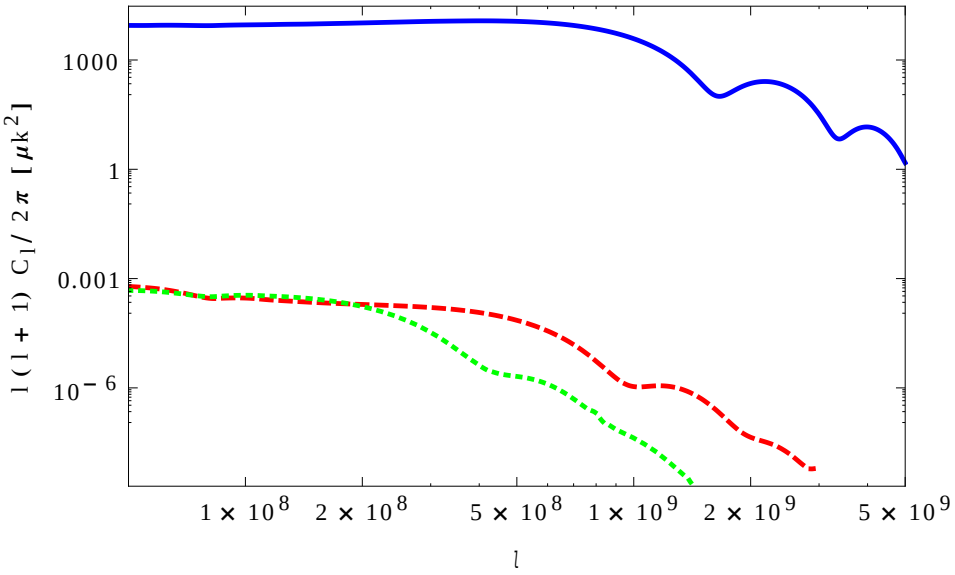


**Figure 5.8:** The total anisotropy power spectra for three mass eigenstates after averaging over all the momenta. The blue (solid), red (dashed) and green (dotted) curves are the power spectra for $m_1 = 0$ eV, $m_2 = 0.00894$ eV and $m_3 = 0.05894$ eV mass eigenstates respectively.

$$
\begin{aligned}
C_l^{\mathrm{eff},m_i} &= 4\pi A \int \frac{dk}{k} |\theta_l^{\mathrm{eff},m_i}(k)|^2 \qquad (5.44)\\
&= \frac{4\pi A}{(\int dp p^2 f_0(p))^2} \int dp p^2 f_0(p) \int dq q^2 f_0(q)\\
&\times \int \frac{dk}{k} [\hat{S}_{m_i}^{\mathrm{eff}}(k)]^2 j_l[k\chi_0^{m_i,p}] j_l[k\chi_0^{m_i,q}]\\
&= \frac{2\pi^2 A}{l^3 (\int dp p^2 f_0(p))^2} \int dp p^4 f_0^2(p) \frac{\chi_0^{m_i,p}}{\chi_0^{'m_i,p}} [\hat{S}_{m_i}^{\mathrm{eff}}(\frac{l}{\chi_0^{m_i,p}})]^2.
\end{aligned}
$$

To get the last line, we again used the completeness relation of the bessel functions to carry out the integral over wave number $k$. $\chi_0^{'m_i,p}$ in here is the derivative of the comoving distance with respect to the momentum.

The total effective anisotropy power spectra for the three mass eigenstates for

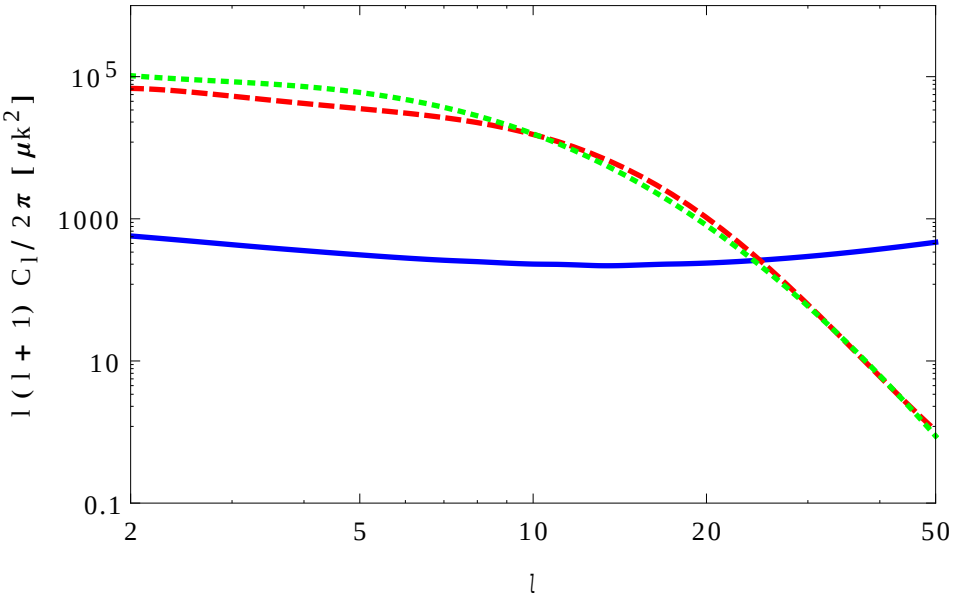


**Figure 5.9:** The averaged anisotropy power spectrum over all momenta at low $l$ values for three mass eigenstates: $m_1 = 0$ eV (blue, solid), $m_2 = 0.00894$ eV (red, dashed) and $m_3 = 0.05894$ eV (green, dotted). Averaging over all momenta leads to smaller amplitude for the power spectra at smaller scales.

the small scales are plotted in Figure 5.8. The amplitude of the power spectrum for the massive neutrinos are significantly smaller than for the massless one. The reason for this is that the massive neutrinos with different momenta come from different distances and if the range of the distances is much larger than the matter correlation length ($\simeq$ 7Mpc) then the perturbations for different momenta are uncorrelated and their contribution partly averages out giving a significantly smaller anisotropy power spectrum.

For the large-scale part of the power spectrum we used a modified version of CAMB [24] to calculate the temperature perturbations for different momenta and used Eq. 5.43 to average over all momenta to get the total power spectrum. The result is shown in Figure 5.9. Similar to the small-scale part, averaging over all momenta leads to a smaller amplitude for the power spectrum at smaller scales.

The large-scale part of the anisotropy power spectra for massive neutrinos has previously been calculated in Ref. [59] but our result is different than theirs. The first reason for this difference is that using Eq. 5.43 we averaged over momenta at the perturbation level, which we believe is the correct way to deal with this problem, but in Ref. [59], first the power spectra at different momenta are calculated and then they are averaged over momenta. The second reason is that we have included the effect of the variation of the distance from the last scattering surface for massive neutrinos, which apparently was not included in Ref. [59], and as we discussed above, neutrinos with different momenta coming from different distances is the main reason for having smaller power spectra at smaller scales.

We use Eq. 5.43 to evaluate the total power spectrum for an electron or tau neutrino at the detector. For the small-scale part of the power spectrum, since the amplitude anisotropy power spectrum for the massless neutrinos is much larger than the massive ones, they contribute the most to the power spectrum for flavour eigenstates. In contrast, for the large-scale part the amplitude of the massive neutrinos is significantly larger than the amplitude for the massless ones, therefore the massive neutrinos contribute the most for flavour eigenstates. The results are shown in Figures 5.10 and 5.11.

## 5.7 Extra neutrino interactions via an alternative Fermi constant

In previous sections we assumed the only relevant interactions for neutrinos are weak interactions in the standard model which results in neutrino free-streaming from the last scattering surface at the weak decoupling epoch. But a nonstandard neutrino self-interaction may delay the neutrino free-streaming until a much later time. A recent study [61] showed that the CMB data allows for a neutrino self-interaction strength $G_{\rm eff}$ that is orders of magnitude larger than the standard Fermi constant. In fact $G_{\rm eff} \lesssim 10^{-5}$ MeV$^{-2}$ has almost no impact on the CMB and can delay the neutrino free-streaming until their temperature is as low as $\sim 200$ eV. Even an alternative cosmology with strongly self-interacting neutrinos ($G_{\rm eff} \lesssim 10^{-2}$ MeV$^{-2}$) in which start free-streaming very close to the matter-radiation equality is compatible with CMB.

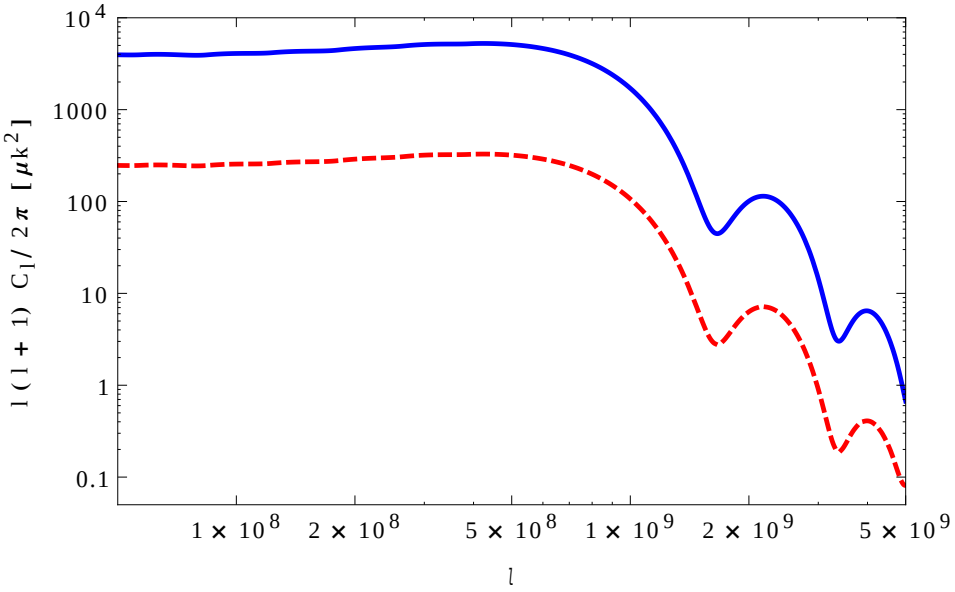


**Figure 5.10:** The small-scale part of the anisotropy power spectrum for an electron neutrino (blue, solid) and a muon neutrino (red, dashed) at the detector. Note that since the amplitude of the power spectrum for massless neutrinos is significantly larger than for the massive ones, they contribute the most.

To show how the neutrino anisotropy power spectrum can be affected by the neutrino self-interaction strength, we evaluated it for a larger value of $G_{\rm eff}$ which is still compatible with the CMB data. The anisotropy power spectra for mass eigenstates for when the self-interaction strength is $G_{\rm eff} \simeq 10^{-5}$ MeV$^{-2}$ are plotted in Figure 5.12.

The stronger self-interactions delay the neutrino decoupling until $T \simeq 240$ eV for $G_{\rm eff} \simeq 10^{-5}$ MeV$^{-2}$ which lead to a shift for the small-scale part of the power spectrum toward much lower $l$ values.

## 5.8 Conclusion

In this chapter, we have studied the anisotropies of the cosmic neutrino background for both massless and massive neutrinos. Assuming the normal hierarchy

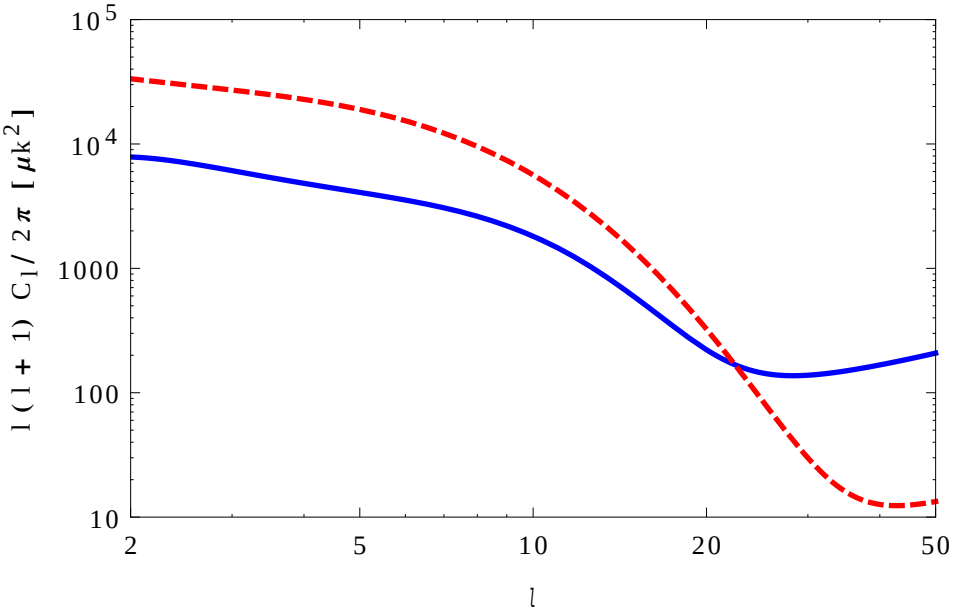


**Figure 5.11:** The large-scale part of the anisotropy power spectrum for an electron neutrino (blue, solid) and a muon neutrino (red, dashed) at the detector. Note that since the amplitude of the power spectrum for massive neutrinos is significantly larger than for the massless ones, they contribute the most.

for the neutrino masses, the CNB power spectrum is calculated with allowing neutrinos to oscillate and it's shown that there is some resemblance between neutrino power spectrum and the usual CMB spectrum as both have acoustic oscillations and silk damping. The acoustic oscillations are due to the competition between the gravitational collapse and pressure of relativistic neutrinos and the Silk damping is due to the finite thickness of the last scattering surface. In contrast to the CMB power spectrum, in the CNB spectrum the height of the peaks do not alternate because there is no non-relativistic particles during neutrino decoupling to resemble baryons during photons last scattering.

The anisotropy power spectra of massless and massive neutrinos differ from each other in a few ways: first the ISW effect for massive neutrinos is larger than for the massless ones which leads to a boost in the large scales for massive neu-

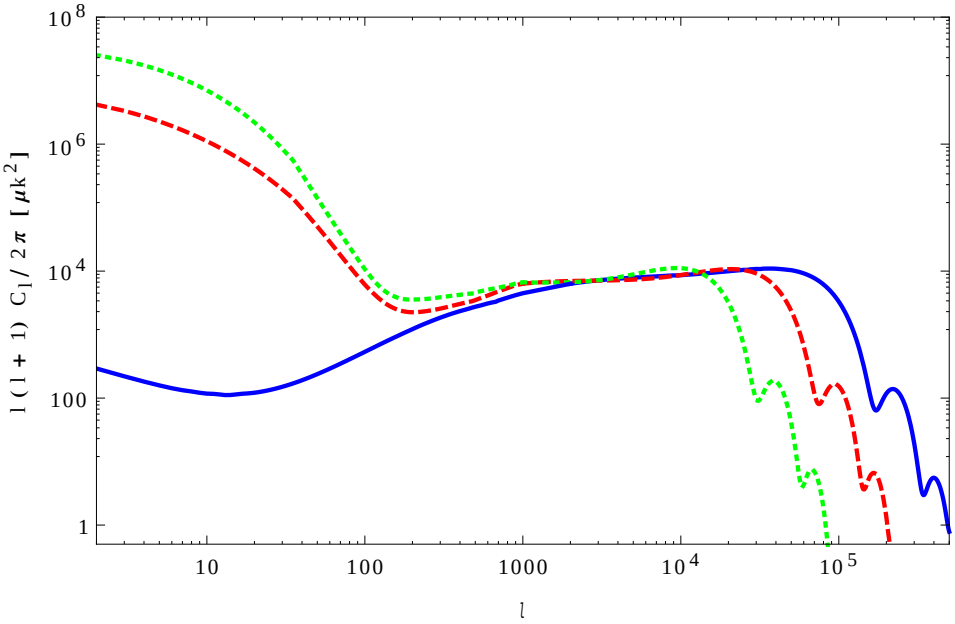


**Figure 5.12:** The anisotropy power spectrum for massive neutrinos with momentum $p = 0.0005$ eV with the self-interaction strength of $G_{\rm eff} \simeq 10^{-5}$ MeV$^{-2}$. The blue (solid), red (dashed) and green (dotted) curves are the power spectra for $m_1 = 0$ eV, $m_2 = 0.00894$ eV and $m_3 = 0.05894$ eV mass eigenstates respectively.

trinos. Also the distance from the last scattering surface for the massive neutrinos is smaller which means that the power spectrum shifts toward lower $l$ values for them. Moreover since this distance depends on the momentum, the anisotropy power spectrum for massive neutrinos are momentum-dependent. We also averaged over all the momenta to get the total anisotropy power spectra for mass eigenstates and showed that the amplitude of the power spectra for massive neutrinos are much smaller than massless ones since the massive neutrinos with different momenta come from different distances and because the range of the distances that they come from is larger than the matter correlation length, they are uncorrelated and their contribution partly averages out and gives a much smaller amplitude.

In addition we investigated the possibility of having strong nonstandard self-interactions in neutrino sector which is compatible with the current cosmological

data and showed how these strong self-interactions delay the time of neutrino decoupling and therefore shift the small-scale part of the spectrum toward lower $l$ values. While detecting these anisotropies is far beyond any technology we can imagine, in principle, detecting small-scale anisotropies in the CNB would put very tight limits on new physics in the neutrino sector.

# Chapter 6

# Conclusion

In this thesis we studied two projects in the pursuit of improving cosmological perturbation theory and therefore our knowledge about the Universe around us. We summarize the main results obtained in this two projects.

In chapter 4 we calculated the effect of Rayleigh scattering on CMB temperature and polarization anisotropies as well as the impact on cosmic structure. The frequency dependence of the Rayleigh cross section breaks the thermal nature of CMB temperature and polarization anisotropies and makes them frequency-dependent. We introduced a new method to capture the effect of the frequency-dependence of the Rayleigh cross section by tracking the spectral distortion perturbations rather than photon perturbations at a particular frequency, which allows for an accurate treatment of Rayleigh scattering including its back-reaction on baryon perturbations with only a few spectral-distortion hierarchies. We have found that Rayleigh scattering modifies the distribution of matter in the Universe at the 0.3% level.

We displayed the effect of Rayleigh scattering on the CMB power spectra for four different frequencies and showed that for each frequency of interest, Rayleigh scattering reduces the $C_l$ power spectrum at high l multipoles because the visibility function shifts to lower redshifts when the Silk damping is more important. In addition, the shift of the visibility function toward later times leads to a boost in Low-multipole E-polarization anisotropies because the CMB quadrupole is larger at later times. For reference, at 857 GHz, the highest frequency of the Planck

experiment, both temperature and E-polarization anisotropies decrease as much as 20% near $l \sim 1000$ and the increase in E-polarization signal at $l \sim 50$ is 35%.

We also investigated the possibility of detecting the Rayleigh signal in the CMB and showed that with a future CMB mission with many high frequency channels like a PRISM-like experiment the Rayleigh signal might be detectable. Measuring the Rayleigh signal could provide powerful constraints on cosmological parameters including the helium fraction and scalar spectral index. We also investigate how more ambitious experiments either observing in low foreground contaminated regions or using a more sophisticated foreground removal method might detect the Rayleigh CMB sky at high signal-to-noise which would tighten CMB constraints on cosmological parameters beyond what was, even in principle, previously thought possible.

In chapter 5, we studied the anisotropies of the Cosmic Neutrino Background radiation. We derived the angular power spectrum for both massless and massive neutrinos with allowing them to oscillate. Similar to the CMB power spectrum, the CNB spectrum has the same peak structure which is due to the fact that radiation pressure from the neutrinos resists the gravitational compression into potential wells and sets up acoustic oscillations. Also due to the finite thickness of the neutrino last scattering surface, small scales in the power spectrum are damped.

We also studied the difference between the anisotropy power spectra for massless and massive neutrinos and showed that since the last scattering surface for the massive neutrinos is closer to us, the locations of the peaks in the power spectrum shift to lower $l$ values. Also the larger ISW term for massive neutrinos enhances the large-scale part of the power spectrum. Moreover the anisotropy power spectrum for massive neutrinos is momentum-dependent and averaging over all momenta leads to a smaller amplitude for smaller scales since the range of distances that massive neutrinos are coming from is larger than the matter correlation length, and thus they are uncorrelated.

In addition, we discussed the effect of extra nonstandard neutrino self-interactions and showed that the delay in the time of neutrino decoupling caused by these extra self-interactions which are allowed by the current cosmological data makes the locations of the peaks in the power spectrum shift toward much lower $l$ values.

# Bibliography


[1] S. Dodelson. *Modern Cosmology*. Academic Press. Academic Press, 2003. ISBN: 9780122191411. → pages ix, 4, 5, 6, 12, 13, 20, 21, 22, 78

[2] Planck Collaboration, R. Adam, P. A. R. Ade, N. Aghanim, Y. Akrami, M. I. R. Alves, M. Arnaud, F. Arroja, J. Aumont, C. Baccigalupi, and et al. Planck 2015 results. I. Overview of products and scientific results. *ArXiv e-prints*, February 2015. → pages ix, 1, 5, 6, 7, 8, 77

[3] E. Komatsu and et al. [WMAP Collaboration]. *Astrophys. J. Suppl.*, 180:330–376, February 2009. → pages 1, 5, 26, 77

[4] Ruhl et al. The south pole telescope. *Proc. SPIE*, 5498:11–29, 2004. → pages 1, 26

[5] A. Kosowsky. The Atacama Cosmology Telescope. *nar*, 47:939–943, December 2003. → pages 1, 26

[6] PRISM Collaboration. PRISM (Polarized Radiation Imaging and Spectroscopy Mission): A White Paper on the Ultimate Polarimetric Spectro-Imaging of the Microwave and Far-Infrared Sky. *ArXiv e-prints*, June 2013. → pages 2, 26, 58

[7] A. Kogut, D.J. Fixsen, D.T. Chuss, J. Dotson, E. Dwek, M. Halpern, G.F. Hinshaw, S.M. Meyer, S.H. Moseley, M.D. Seiffert, D.N. Spergel, and E.J. Wollack. The primordial inflation explorer (pixie): a nulling polarimeter for cosmic microwave background observations. *Journal of Cosmology and Astroparticle Physics*, 2011(07):025, 2011. → pages 2, 26

[8] E. Komatsu and et al. [WMAP Collaboration]. Seven-year wilkinson microwave anisotropy probe (wmap) observations: Cosmological interpretation. *The Astrophysical Journal Supplement Series*, 192(2):18, 2011. → pages 2

[9] Planck Collaboration, P. A. R. Ade, N. Aghanim, M. Arnaud, M. Ashdown, J. Aumont, C. Baccigalupi, A. J. Banday, R. B. Barreiro, J. G. Bartlett, and et al. Planck 2015 results. XIII. Cosmological parameters. *ArXiv e-prints*, February 2015. → pages 2

[10] Michael Rauch, Jordi Miralda-Escud, Wallace L. W. Sargent, Tom A. Barlow, David H. Weinberg, Lars Hernquist, Neal Katz, Renyue Cen, and Jeremiah P. Ostriker. The opacity of the ly forest and implications for b and the ionizing background. *The Astrophysical Journal*, 489(1):7, 1997. → pages 2

[11] John M. OMeara, David Tytler, David Kirkman, Nao Suzuki, Jason X. Prochaska, Dan Lubin, and Arthur M. Wolfe. The deuterium to hydrogen abundance ratio toward a fourth qso: Hs 0105+1619. *The Astrophysical Journal*, 552(2):718, 2001. → pages 2

[12] W. Rindler. Visual horizons in world models. *mnras*, 116:662, 1956. → pages 3

[13] Robert Henry Dicke. *Gravitation and the universe*. American Philosophical Society, Philadelphia, PA, 1970. → pages 3

[14] D. Baumann. TASI Lectures on Inflation. *ArXiv e-prints*, July 2009. → pages 3, 23

[15] A. A. Penzias and R. W. Wilson. A Measurement of Excess Antenna Temperature at 4080 Mc/s. *apj*, 142:419–421, July 1965. → pages 5

[16] J. C. Mather, E. S. Cheng, R. E. Eplee, Jr., R. B. Isaacman, S. S. Meyer, R. A. Shafer, R. Weiss, E. L. Wright, C. L. Bennett, N. W. Boggess, E. Dwek, S. Gulkis, M. G. Hauser, M. Janssen, T. Kelsall, P. M. Lubin, S. H. Moseley, Jr., T. L. Murdock, R. F. Silverberg, G. F. Smoot, and D. T. Wilkinson. A preliminary measurement of the cosmic microwave background spectrum by the Cosmic Background Explorer (COBE) satellite. *apjl*, 354:L37–L40, May 1990. → pages 5

[17] W. Hu. Lecture Notes on CMB Theory: From Nucleosynthesis to Recombination. *ArXiv e-prints*, February 2008. → pages 7, 8

[18] A. Kosowsky. The cosmic microwave background. In S. Bonometto, V. Gorini, and U. Moschella, editors, *Modern Cosmology*, pages 219–263, 2002. → pages 7, 8

[19] E. M. Lifshitz. On the gravitational stability of the expanding universe. *Zhurnal Eksperimentalnoi i Teoreticheskoi Fiziki*, 16:587–602, 1946. → pages 11

[20] James M. Bardeen. Gauge-invariant cosmological perturbations. *Phys. Rev. D*, 22:1882–1905, Oct 1980. → pages 11, 15

[21] V.F. Mukhanov, H.A. Feldman, and R.H. Brandenberger. Theory of cosmological perturbations. *Physics Reports*, 215(56):203 – 333, 1992. → pages 11, 26

[22] C.-P. Ma and E. Bertschinger. *Astrophys. J.*, 455:7, December 1995. → pages 12, 15, 16, 18, 19, 26, 31, 86, 95

[23] Arthur Kosowsky. Introduction to microwave background polarization. *New Astronomy Reviews*, 43(24):157 – 168, 1999. → pages 22, 26

[24] Antony Lewis, Anthony Challinor, and Anthony Lasenby. *Astrophys. J.*, 538:473–476, 2000. → pages 24, 37, 45, 50, 79, 97, 103

[25] M. Tegmark, D. J. Eisenstein, W. Hu, and A. de Oliveira-Costa. Foregrounds and Forecasts for the Cosmic Microwave Background. *apj*, 530:133–165, February 2000. → pages 25, 58, 60

[26] Scott Dodelson. Determining cosmic microwave background anisotropies in the presence of foregrounds. *The Astrophysical Journal*, 482(2):577, 1997. → pages 25

[27] Franois R. Bouchet and Richard Gispert. Foregrounds and {CMB} experiments: I. semi-analytical estimates of contamination. *New Astronomy*, 4(6):443 – 479, 1999. → pages 25

[28] Lloyd Knox. Forecasting foreground impact on cosmic microwave background measurements. *Monthly Notices of the Royal Astronomical Society*, 307(4):977–983, 1999. → pages 25

[29] P. J. E. Peebles and J. T. Yu. Primeval Adiabatic Perturbation in an Expanding Universe. *apj*, 162:815, December 1970. → pages 26

[30] Planck Collaboration, P. A. R. Ade, N. Aghanim, C. Armitage-Caplan, M. Arnaud, M. Ashdown, F. Atrio-Barandela, J. Aumont, C. Baccigalupi, A. J. Banday, and et al. Planck 2013 results. I. Overview of products and scientific results. *ArXiv e-prints*, March 2013. → pages 26, 37

[31] Q. Yu, D. N. Spergel, and J. P. Ostriker. Rayleigh Scattering and Microwave Background Fluctuations. *apj*, 558:23–28, September 2001. → pages 27, 34

[32] A. Lewis. Rayleigh scattering: blue sky thinking for future CMB observations. *jcap*, 8:53, August 2013. → pages 27, 34

[33] Kenneth R. Lang. *Astrophysical formulae*. Springer, New York, 1999. → pages 28, 29

[34] H. C. Goldwire, Jr. Oscillator Strengths for Electric Dipole Transitions of Hydrogen. *apjs*, 17:445, December 1968. → pages 29

[35] Akihiro Kono and Shuzo Hattori. Accurate oscillator strengths for neutral helium. *Phys. Rev. A*, 29:2981–2988, Jun 1984. → pages 30

[36] W. C. Martin. Improved $^4$i *1snl* ionization energy, energy levels, and lamb shifts for *1sns* and *1snp* terms. *Phys. Rev. A*, 36:3575–3589, Oct 1987. → pages 30

[37] G. S. Khandelwal, F. Khan, and J. W. Wilson. An asymptotic expression for the dipole oscillator strength for transitions of the He sequence. → pages 30

[38] W. Cunto, C. Mendoza, F. Ochsenbein, and C. J. Zeippen. Topbase at the CDS. *aap*, 275:L5, August 1993. → pages 30

[39] V. B. Berestetskii, E. M. Lifshitz, and V. B. Pitaevskii. *Relativistic quantum theory. Pt.1*. 1971. → pages 30

[40] C. M. Hirata. Wouthuysen-Field coupling strength and application to high-redshift 21-cm radiation. *mnras*, 367:259–274, March 2006. → pages 31

[41] Anthony Challinor. Microwave background polarization in cosmological models. *Phys. Rev. D*, 62:043004, Jul 2000. → pages 31, 42

[42] U. Seljak and M. Zaldarriaga. *apj*, 469:437, October 1996. → pages 39, 42, 87

[43] Max Tegmark. How to make maps from cosmic microwave background data without losing information. *The Astrophysical Journal Letters*, 480(2):L87, 1997. → pages 59

[44] Planck collaboration, P. A. R. Ade, N. Aghanim, C. Armitage-Caplan, M. Arnaud, M. Ashdown, F. Atrio-Barandela, J. Aumont, C. Baccigalupi,

A. J. Banday, and et al. Planck 2013 results. XV. CMB power spectra and likelihood. *ArXiv e-prints*, March 2013. → pages 60

[45] Planck Collaboration, A. Abergel, P. A. R. Ade, N. Aghanim, D. Alina, M. I. R. Alves, G. Aniano, C. Armitage-Caplan, M. Arnaud, M. Ashdown, and et al. Planck 2013 results. XI. All-sky model of thermal dust emission. *ArXiv e-prints*, December 2013. → pages

[46] Planck Collaboration, R. Adam, P. A. R. Ade, N. Aghanim, M. Arnaud, J. Aumont, C. Baccigalupi, A. J. Banday, R. B. Barreiro, J. G. Bartlett, and et al. Planck intermediate results. XXX. The angular power spectrum of polarized dust emission at intermediate and high Galactic latitudes. *ArXiv e-prints*, September 2014. → pages

[47] Planck Collaboration, P. A. R. Ade, N. Aghanim, C. Armitage-Caplan, M. Arnaud, M. Ashdown, F. Atrio-Barandela, J. Aumont, C. Baccigalupi, A. J. Banday, and et al. Planck 2013 results. XXX. Cosmic infrared background measurements and implications for star formation. *ArXiv e-prints*, September 2013. → pages 60

[48] Mathew S. Madhavacheril, Neelima Sehgal, and Tracy R. Slatyer. Current dark matter annihilation constraints from cmb and low-redshift data. *Phys. Rev. D*, 89:103508, May 2014. → pages 76

[49] Steven Weinberg. *Phys. Rev.*, 128:1457–1473, Nov 1962. → pages 77

[50] A. G. Cocco, G. Mangano, and M. Messina. *Journal of Physics Conference Series*, 120(2):022005, July 2008. → pages

[51] M. Blennow. *prd*, 77(11):113014, June 2008. → pages

[52] S. Betts, W. R. Blanchard, R. H. Carnevale, C. Chang, C. Chen, S. Chidzik, L. Ciebiera, P. Cloessner, A. Cocco, A. Cohen, J. Dong, R. Klemmer, M. Komor, C. Gentile, B. Harrop, A. Hopkins, N. Jarosik, M. Messina, B. Osherson, Y. Raitses, W. Sands, M. Schaefer, J. Taylor, C. G. Tully, R. Woolley, and A. Zwicker. *ArXiv e-prints*, July 2013. → pages 77

[53] B. R. Safdi, M. Lisanti, J. Spitz, and J. A. Formaggio. Annual modulation of cosmic relic neutrinos. *prd*, 90(4):043001, August 2014. → pages 77

[54] S. Weinberg. *Cosmology*. Oxford University Press, 2008. ISBN: 978-0198526827. → pages 78

[55] Scott Dodelson and Michael S. Turner. *Phys. Rev. D*, 46:3372–3387, Oct 1992. → pages 78, 82, 83

[56] S. Esposito, G. Miele, and et al. *Nuclear Physics B*, 590:539–561, December 2000. → pages 78, 87

[57] A. D. Dolgov, S. H. Hansen, and D. V. Semikoz. *Nuclear Physics B*, 503:426–444, February 1997. → pages 78

[58] R. J. Michney and R. R. Caldwell. Anisotropy of the cosmic neutrino background. *jcap*, 1:14, January 2007. → pages 78, 79

[59] S. Hannestad and J. Brandbyge. *jcap*, 3:20, March 2010. → pages 78, 79, 104

[60] S. Dodelson and M. Vesterinen. Cosmic Neutrino Last Scattering Surface. *Physical Review Letters*, 103(17):171301, October 2009. → pages 79

[61] F.-Y. Cyr-Racine and K. Sigurdson. Limits on neutrino-neutrino scattering in the early Universe. *prd*, 90(12):123533, December 2014. → pages 79, 104

[62] Nicole F. Bell, Elena Pierpaoli, and Kris Sigurdson. *Phys. Rev. D*, 73:063523, Mar 2006. → pages 80

[63] K. A. Malik and D. Wands. *jcap*, 2:7, February 2005. → pages 87

[64] A. C. Hindmarsh. Odepack, a systematized collection of ode solvers. *Scientific Publishing, North Holland*, 1983. → pages 87

[65] Roman Tomaschitz. Weber and beltrami integrals of squared spherical bessel functions: finite series evaluation and high-index asymptotics. *Mathematical Methods in the Applied Sciences*, 37(9):1249–1272, 2014. → pages 92

[66] A. Strumia and F. Vissani. Neutrino masses and mixings and... *ArXiv High Energy Physics - Phenomenology e-prints*, June 2006. → pages 95

[67] A. Cooray and W. Hu. Imprint of Reionization on the Cosmic Microwave Background Bispectrum. *apj*, 534:533–550, May 2000. → pages 100

# Appendix A

# phase-space integration for driving neutrino evolution equations

In this Appendix, we calculate the terms $A_i$, $B_i$, $C_i$ and $D_i$ in the Boltzmann equations that govern the evolution of neutrino anisotropies, equation 5.6 in chapter 5.

One can evaluate some of the integrals in these terms very easily since portions of the integrand in them are Lorentz-invariant and thus some part of the integration can be carried out in the center of mass frame. These integrals are

$$\begin{aligned}
&\int d\Lambda s^2 f_0(q) = 3\int d\Lambda t^2 f_0(q) = 3\int d\Lambda u^2 f_0(q) = \frac{p^2T^4}{\pi^3},\\
&\int d\Lambda f_0(p) q\frac{\partial f_0}{\partial q}\theta_\nu(\hat{q})s^2 = 3\int d\Lambda f_0(p) q\frac{\partial f_0}{\partial q}\theta_\nu(\hat{q})t^2\\
&= 3\int d\Lambda f_0(p) q\frac{\partial f_0}{\partial q}\theta_\nu(\hat{q})u^2\\
&= -\frac{3p^2T^4}{\pi^3} f_0(p)(\frac{4}{3}\theta_{\nu 0} + 2i\mu\theta_{\nu 1} - \frac{3\mu^2-1}{3}\theta_{\nu 2}).
\end{aligned} \tag{A.1}$$

For the rest of the integrals, one must carry out all of the integrations in FRW frame. For these integrals, the following method can be used: First we use the

momentum part of the energy momentum delta function to carry out the $d\Pi_q$ integration. Then $d\Lambda$ can be expressed as:

$$d\Lambda = \frac{1}{256\pi^5}\frac{d^3q'}{q'}\frac{\delta(\mu'-\mu_0)dp'd\mu'd\phi'}{|\vec{p}-\vec{q'}|}, \tag{A.2}$$

where $\mu' = \cos\theta'$, $\theta'$ is the angle between $\vec{p'}$ and $(\vec{p}-\vec{q'})$, $\phi'$ is the angle between the plane defined by $p$ and $q'$ and that defined by $p'$ and $q$, and $\mu_0$ is given by

$$\mu_0 = \frac{-\vec{p}.\vec{q'}+p'(p-q')+pq'}{p'|\vec{p}-\vec{q'}|}. \tag{A.3}$$

The limits of $dp'$ integration are $p'_- < p' < \infty$ where

$$p'_- = \frac{|\vec{p}-\vec{q'}|+(p-q')}{2}. \tag{A.4}$$

Using this method, if we write $P_l(\eta) = \sum_{n=0}^{l} h_{n,l}\eta^n$, the following integrals can be evaluated:

$$\int d\Lambda f_{y0}(p')q'\frac{\partial f_{x0}}{\partial q'}\theta_x(\hat{q'})u^2 = \tag{A.5}$$
$$-\frac{p^2T_y^5/T_x}{16\pi^3}P_l(\mu)\sum_{l=0}^{\infty}(-i)^l(2l+1)\theta_{el}\sum_{n=0}^{l}h_{n,l}J_1(l,n,\frac{p}{T_y},r),$$
$$\int d\Lambda f_{y0}(p')q'\frac{\partial f_{x0}}{\partial q'}\theta_x(\hat{q'})t^2 = \tag{A.6}$$
$$-\frac{p^2T_y^5/T_x}{32\pi^3}P_l(\mu)\sum_{l=0}^{\infty}(-i)^l(2l+1)\theta_{el}\sum_{n=0}^{l}h_{n,l}J_2(l,n,\frac{p}{T_y},r),$$
$$\int d\Lambda f_{y0}(p')q'\frac{\partial f_{x0}}{\partial q'}\theta_x(\hat{q'})ut = \tag{A.7}$$
$$-\frac{p^2T_y^5/T_x}{16\pi^3}P_l(\mu)\sum_{l=0}^{\infty}(-i)^l(2l+1)\theta_{el}\sum_{n=0}^{l}h_{n,l}J_3(l,n,\frac{p}{T_y},r).$$

In here we define $\mu = \hat{p}.\hat{k}$, $z = \frac{p}{T_\nu}$, $r = \frac{T_\nu}{T_\gamma}$ and

$$J_1(l,n,z,r) = \int_{-1}^{1} d\eta (1-\eta)^2 \eta^n \int_0^\infty dx \frac{x^4 e^{-xr}}{\sqrt{z^2+x^2-2xz\eta}} \tag{A.8}$$
$$\times \mathrm{Exp}[-\frac{\sqrt{z^2+x^2-2xz\eta}+z-x}{2}],$$
$$J_2(l,n,z,r) = \int_{-1}^{1} d\eta \eta^n \int_0^\infty dx \frac{x^2 e^{-xr}}{\sqrt{z^2+x^2-2xz\eta}} \tag{A.9}$$
$$\times([3-v^2+\beta^2(3v^2-1)-4\beta v][y^2+2y+2]$$
$$+[2\alpha\beta(3v^2-1)-4\alpha v][1+y]+\alpha^2[3v^2-1])e^{-y},$$
$$J_3(l,n,z,r) = \int_{-1}^{1} (1-\eta) d\eta \eta^n \int_0^\infty dx \frac{x^3 e^{-xr}}{\sqrt{z^2+x^2-2xz\eta}} \tag{A.10}$$
$$\times[(1-\beta v)(1+y)-\alpha v]e^{-y},$$

where

$$\alpha = \frac{zx(1-\eta)}{\sqrt{z^2+x^2-2xz\eta}}, \tag{A.11}$$
$$\beta = \frac{z-x}{\sqrt{z^2+x^2-2xz\eta}}, \tag{A.12}$$
$$y = \frac{1}{2}(\sqrt{z^2+x^2-2xz\eta}+z-x), \tag{A.13}$$
$$v = \frac{z-x\eta}{\sqrt{z^2+x^2-2xz\eta}}. \tag{A.14}$$

Finally we are able to evaluate all the terms $A_i$, $B_i$, $C_i$ and $D_i$:

$$A_e(\frac{p}{T_\nu}) = \frac{1}{3\pi^3}(\frac{p}{T_\nu})^2[4(a_w+b_w)(\frac{T_\gamma}{T_\nu})^4+a_w+b_w+17], \tag{A.15}$$

$$\begin{aligned} B_e(\frac{p}{T_\nu},\mu) &= -\frac{(a_w+b_w+9)}{\pi^3}(\frac{p}{T_\nu})^2 f_{\nu 0}(p)[\frac{4}{3}\theta_{\nu_e 0}+2i\mu\theta_{\nu_e 1}-\frac{3\mu^2-1}{3}\theta_{\nu_e 2}] \\ &+\frac{(\frac{p}{T_\nu})^2}{16\pi^3}\sum_{l=0}^{\infty}(-i)^l(2l+1)\theta_{\nu_e l}P_l(\mu)\sum_{n=0}^{l}h_{n,l}[8J_1(l,n,z,1)+5J_2(l,n,z,1) \\ &+8J_3(l,n,z,1)+r^{-10}(a_w+b_w)(J_1(l,n,z,r^{-1})+J_2(l,n,z,r^{-1})+2J_3(l,n,z,r^{-1}))], \end{aligned} \tag{A.16}$$

$$\begin{aligned} C_e(\frac{p}{T_\nu},\mu) &= -\frac{8}{\pi^3}(\frac{p}{T_\nu})^2 f_{\nu 0}(p)[\frac{4}{3}\theta_{\nu_\mu 0}+2i\mu\theta_{\nu_\mu 1}-\frac{3\mu^2-1}{3}\theta_{\nu_\mu 2}] \\ &+\frac{(\frac{p}{T_\nu})^2}{16\pi^3}\sum_{l=0}^{\infty}(-i)^l(2l+1)\theta_{\nu_\mu l}P_l(\mu)\sum_{n=0}^{l}h_{n,l}[(6J_1(l,n,z,1)) \\ &+2J_2(l,n,z,1)+4J_3(l,n,z,1)], \end{aligned} \tag{A.17}$$

$$\begin{aligned} D_e(\frac{p}{T_\nu},\mu) &= -\frac{4(a_w+b_w)}{\pi^3}(\frac{p}{T_\nu})^2 f_{\nu 0}(p)[\frac{4}{3}\theta_{\nu_e 0}+2i\mu\theta_{\nu_e 1}-\frac{3\mu^2-1}{3}\theta_{\nu_e 2}] \\ &+\frac{(\frac{p}{T_\nu})^2}{16\pi^3}(a_w+b_w)r^{-4}\sum_{l=0}^{\infty}(-i)^l(2l+1)\theta_{el}P_l(\mu)\sum_{n=0}^{l}h_{n,l} \\ &[r^{-4}(J_1(l,n,\frac{p}{T_\gamma},1)+\frac{1}{2}J_2(l,n,\frac{p}{T_\gamma},1))+r(j_1(l,n,z,r)+\frac{1}{2}J_2(l,n,z,r) \\ &+2J_3(l,n,z,r))], \end{aligned} \tag{A.18}$$

$$A_\mu(\frac{p}{T_\nu}) = \frac{1}{3\pi^3}(\frac{p}{T_\nu})^2[4(c_w+b_w)(\frac{T_\gamma}{T_\nu})^4+c_w+b_w+17], \tag{A.19}$$

$$\begin{aligned} B_\mu(\frac{p}{T_\nu},\mu) &= -\frac{(c_w+b_w+13)}{\pi^3}(\frac{p}{T_\nu})^2 f_{\nu 0}(p)[\frac{4}{3}\theta_{\nu_\mu 0}+2i\mu\theta_{\nu_\mu 1}-\frac{3\mu^2-1}{3}\theta_{\nu_\mu 2}] \\ &+\frac{(\frac{p}{T_\nu})^2}{16\pi^3}\sum_{l=0}^{\infty}(-i)^l(2l+1)\theta_{\nu_\mu l}P_l(\mu)\sum_{n=0}^{l}h_{n,l}[11J_1(l,n,z,1)+6J_2(l,n,z,1) \\ &+10J_3(l,n,z,1)+r^{-10}(c_w+b_w)(J_1(l,n,z,r^{-1})+J_2(l,n,z,r^{-1})+2J_3(l,n,z,r^{-1}))], \end{aligned} \tag{A.20}$$

$$\begin{aligned} C_\mu(\frac{p}{T_\nu},\mu) &= -\frac{4}{\pi^3}(\frac{p}{T_\nu})^2 f_{\nu 0}(p)[\frac{4}{3}\theta_{\nu_e 0}+2i\mu\theta_{\nu_e 1}-\frac{3\mu^2-1}{3}\theta_{\nu_e 2}] \\ &+\frac{(\frac{p}{T_\nu})^2}{16\pi^3}\sum_{l=0}^{\infty}(-i)^l(2l+1)\theta_{\nu_e l}P_l(\mu)\sum_{n=0}^{l}h_{n,l}[(3J_1(l,n,z,1))+J_2(l,n,,z,1) \\ &+2J_3(l,n,z,1)], \end{aligned} \tag{A.21}$$

$$\begin{aligned} D_\mu(\frac{p}{T},\mu) &= -\frac{4(c_w+b_w)}{\pi^3}(\frac{p}{T_\nu})^2 f_{\nu 0}(p)[\frac{4}{3}\theta_{\nu_e 0}+2i\mu\theta_{\nu_e 1}-\frac{3\mu^2-1}{3}\theta_{\nu_e 2}] \\ &+\frac{(\frac{p}{T_\nu})^2}{16\pi^3}(c_w+b_w)r^{-4}\sum_{l=0}^{\infty}(-i)^l(2l+1)\theta_{el}P_l(\mu)\sum_{n=0}^{l}h_{n,l} \\ &[r^{-4}(J_1(l,n,\frac{p}{T_\gamma},1)+\frac{1}{2}J_2(l,n,\frac{p}{T_\gamma},1))+r(j_1(l,n,z,r)+\frac{1}{2}J_2(l,n,z,r) \\ &+2J_3(l,n,z,r))]. \end{aligned} \tag{A.22}$$

To get the Boltzmann equations governing the neutrinos anisotropies, we also

need to define the following functions:

$$
\begin{aligned}
c_{\nu_e}(l,r) &= \sum_{n=0}^{l} h_{n,l}[8I_1(l,n,1)+5I_2(l,n,1)+8I_3(l,n,1) \qquad \text{(A.23)}\\
&+r^{-10}(a_w+b_w)(I_1(l,n,r^{-1})+I_2(l,n,r^{-1})+2I_3(l,n,r^{-1}))],\\
c_{\nu_\mu}(l) &= \sum_{n=0}^{l} h_{n,l}[6I_1(l,n,1)+2I_2(l,n,1)+4I_3(l,n,1)],\\
c_e(l,r) &= \sum_{n=0}^{l} h_{n,l}(a_w+b_w)[r^{-9}(I_1(l,n,1)+\frac{1}{2}I_2(l,n,1))\\
&+r(I_1(l,n,r)+\frac{1}{2}I_2(l,n,r)+2I_3(l,n,r))],\\
d_{\nu_\mu}(l,r) &= \sum_{n=0}^{l} h_{n,l}[11I_1(l,n,1)+6I_2(l,n,1)+10I_3(l,n,1)\\
&+r^{-10}(c_w+b_w)(I_1(l,n,r^{-1})+I_2(l,n,r^{-1})+2I_3(l,n,r^{-1}))],\\
d_{\nu_e}(l) &= \sum_{n=0}^{l} h_{n,l}[3I_1(l,n,1)+I_2(l,n,1)+2I_3(l,n,1)],\\
d_e(l,r) &= \sum_{n=0}^{l} h_{n,l}(c_w+b_w)[r^{-9}(I_1(l,n,1)+\frac{1}{2}I_2(l,n,1))\\
&+r(I_1(l,n,r)+\frac{1}{2}I_2(l,n,r)+2I_3(l,n,r))],
\end{aligned}
$$

where

$$
\begin{aligned}
I_1(l,n,r) &= \int_0^\infty z^2 J_1(l,n,z,r)dz = \frac{g_{10}[l]+g_{11}[l]r+g_{12}[l]r^2}{r^6}, \qquad \text{(A.24)}\\
I_2(l,n,r) &= \int_0^\infty z^2 J_2(l,n,z,r)dz = \frac{g_{20}[l]+g_{21}[l]r+g_{22}[l]r^2}{r^6}, \qquad \text{(A.25)}\\
I_3(l,n,r) &= \int_0^\infty z^2 J_3(l,n,z,r)dz = \frac{g_{30}[l]+g_{31}[l]r+g_{32}[l]r^2}{r^6}. \qquad \text{(A.26)}
\end{aligned}
$$

Some of these coefficients,$g_{ij}$, can be calculated analytically and the rest numerically. The result is shown in Table A.1.

| l | l=0 | l=1 | l=2 | l=3 | l=4 | l=5 | l=6 | l=7 | l=8 | l=9 | l=10 |
|---|---|---|---|---|---|---|---|---|---|---|---|
| $g_{10}$ | 160 | 160 | 86.698 | 85.4802 | 55.1955 | 55.2245 | 38.4266 | 39.3688 | 28.3084 | 29.8438 | 21.6903 |
| $g_{11}$ | 384 | -192 | 24.8824 | -112.902 | -7.34499 | -78.3898 | -11.5957 | -59.2652 | -10.7893 | -47.2298 | -9.04102 |
| $g_{12}$ | 0 | 0 | 40.1714 | 0 | 33.8388 | 0 | 27.3112 | 0 | 22.3304 | 0 | 18.5982 |
| $g_{20}$ | 960 | 960 | 914.817 | 872.476 | 830.967 | 792.751 | 757.999 | 725.744 | 696.718 | 669.492 | 644.982 |
| $g_{21}$ | 256 | -128 | -277.308 | -359.741 | -412.057 | -438.336 | -458.874 | -465.633 | -472.85 | -471.336 | -472.246 |
| $g_{22}$ | 0 | 0 | 81.2602 | 86.6739 | 123.392 | 122.681 | 142.786 | 139.207 | 151.415 | 146.591 | 154.511 |
| $g_{30}$ | 160 | 160 | 130.391 | 118.536 | 101.624 | 93.03 | 81.9376 | 75.8088 | 67.9416 | 63.4381 | 57.5606 |
| $g_{31}$ | 128 | -64 | -60.4575 | -84.7234 | -75.4815 | -80.7843 | -72.2895 | -73.0258 | -65.9128 | -65.2953 | -59.4069 |
| $g_{32}$ | 0 | 0 | 81.2602 | 86.6739 | 123.392 | 122.681 | 142.786 | 139.207 | 151.415 | 146.591 | 154.511 |

**Table A.1:** Value of coefficients $g_{ij}$ for different values of $l$.